

MODELLING PHASE CHANGE MATERIAL THERMAL STORAGE SYSTEMS

MODELLING PHASE CHANGE MATERIAL THERMAL STORAGE SYSTEMS

By

JOANNE M. BAILEY, B.A.Sc., P.Eng.

A Thesis

Submitted to the School of Graduate Studies

in Partial Fulfillment of the Requirements

for the Degree

Master of Applied Science

McMaster University

Hamilton, Ontario, Canada

© Copyright by Joanne Bailey, January 2010

MASTER OF APPLIED SCIENCE (2010)
(Mechanical Engineering)

McMASTER UNIVERSITY
Hamilton, Ontario, Canada

TITLE: Modelling Phase Change Material Thermal Storage Systems

AUTHOR: Joanne M. Bailey, B.A.Sc., P. Eng.

SUPERVISOR: Dr. J. S. Cotton

NUMBER OF PAGES: xiv, 157

ABSTRACT

In order to increase the overall efficiency of energy use in a community, excess thermal energy from inefficient processes can be stored and used for heating applications. A one-dimensional analytical conduction model is therefore developed for sizing of phase change material thermal energy storage systems. The model addresses rectangular channels of phase change material separated by flow channels for the addition and removal of thermal energy. The analytical model assumes a planar melt front and linear temperature profiles throughout the thermal storage cell. Heat flux and interface temperatures are calculated at various melt fractions based on a quasi-steady electrical analogue analysis of the instant in question. Compensation is made for the sensible energy change between melt fractions by adding this energy at the calculated heat flux. A two dimensional, conduction only computational fluid dynamics model is used to compare the response of the analytical model to changes in the input parameters and shows good agreement. A test apparatus and a three dimensional computational fluid dynamics model are also created and melt-time results compared to analytical model predictions. These comparisons also show good agreement. Finally, a thermal storage system is sized for a specific application, H₂Green Energy Corporation's Distributed Storage System, with sizing based on the heat load requirements of McMaster Innovation Park during the winter months. Technical feasibility of this system is shown with analysis also included on economic feasibility. It is determined that the analytical model is sufficient for initial assessment of phase change material thermal energy storage

systems where detailed geometry is unavailable. Recommendations are made for further validation of the model and the development of a phase change material properties database. Suggestions are also presented on additional sources of revenue for the H₂Green Distributed Storage System that will increase its economic feasibility.

ACKNOWLEDGEMENTS

The author would like to acknowledge the financial contributions of the Ontario Centres of Excellence, H₂Green Energy Corporation, McMaster University Department of Mechanical Engineering, NSERC and the Canadian Engineering Memorial Foundation towards completion of this thesis.

The author would also like to thank Dan Wright for his assistance with data acquisition and programming, Ron Lodewyks, J.P. Talon, Mark MacKenzie, Jim McLaren and Joe Verhaeghe for their help with the fabrication of the experimental apparatus, Dr. J.S. Cotton for his guidance and supervision over the course of this project and Dr. H.S. Sadek for his continual support and advice.

Table of Contents

Abstract iii

Acknowledgements v

List of Tables ix

List of Figures x

Nomenclature xii

Glossary xiii

CHAPTER 1 – Introduction 1

 1.1 – Background 1

 1.2 – Current Applications of Thermal Storage 2

 1.3 – Potential Applications of Thermal Storage 5

 1.4 – Problem 7

 1.5 – Scope of Work 8

CHAPTER 2 – Thermal Storage Technologies 10

 2.1 – Thermal Storage Options 10

 2.2 – Phase Change Material Categories 12

 2.3 – Low Temperature Phase Change Materials 13

 2.4 – Recent Phase Change Material Thermal Storage Research 19

 2.5 – Capture Systems 24

 2.6 – Recovery Systems 26

 2.7 – Temperature Mediation Systems 27

 2.8 – Design Methodology 27

CHAPTER 3 – PCM Thermal Storage Models 32

 3.1 – PCM Mass 32

 3.2 – One-Dimensional Storage Cell Geometric Model 33

 3.3 – Analytical Model Single Storage Cell Time 34

 3.3.1 – Pseudo-Steady Heat Transfer Model 35

 3.3.2 – Changing Temperature Profile and Sensible Energy 36

 3.3.3 – Equations Used in the Analytical Model 37

 3.4 – Fluent Melting/Solidification Model 38

 3.5 – Two-Dimensional Numerical Storage Cell Model 39

3.5.1 – Effect of Thermal Conductivity	44
3.5.2 – Effect of Latent Heat of Fusion.....	49
3.5.3 – Effect of Sensible Energy Storage	50
3.5.4 – Effect of Capture/Recovery Temperature Difference	52
3.5.5 – Effect of Dimensional Changes	54
3.5.6 – Effect of Capture/Recovery Convective Heat Transfer Coefficient	55
3.6 – Three-Dimensional Sample Cell Model	56
3.6.1 – Lauric Acid Storage Cell.....	57
 CHAPTER 4 – Test Facility	 62
4.1 – Test Cell Design Criteria and Constraints.....	62
4.2 – Phase Change Material Chamber	65
4.3 – Capture/Recovery Fluid Channel.....	68
4.4 – Temperature Measurement	73
4.5 – Flow Measurement and Control.....	75
4.6 – Heat Flux Measurement.....	76
4.7 – Data Acquisition	77
4.8 – Experimental Uncertainty	79
 CHAPTER 5 – Experimental Results, Discussion and Comparison.....	 82
5.1 – Experimental Phase Change Results and Model Validation.....	82
5.2 – Lauric Acid Storage Cell Low Flow	83
5.3 – Effect of Flow Rate	89
5.4 – Effect of Flow Direction	91
5.5 – Discussion	93
 CHAPTER 6 – Sample System Sizing	 95
6.1 – H ₂ Green Distributed Storage System Thermal Storage Sizing.....	95
6.2 – H ₂ Green Distributed Storage System.....	95
6.3 – Capture and Recovery System Definition.....	98
6.4 – PCM Selection	101
6.5 – McMaster Innovation Park Heating Needs	104
6.6 – PCM Thermal Storage System Sizing Results.....	106
6.7 – DSS System Sizing Results	112
 CHAPTER 7 – Conclusions and Recommendations	 116
7.1 – Analytical Model	116
7.2 – Further Model Development and Validation	117
7.3 – PCM Effective Thermal Conductivity Enhancement	118
7.4 – Convective Heat Transfer in Liquid PCM	118

7.5 – PCM Properties Library	119
7.5.1 – Thermal Conductivity Testing	119
7.5.2 – Thermal Cycling Stability Testing.....	120
7.6 – H ₂ Green Distributed Storage System.....	120
REFERENCES	121
APPENDIX A – Experimental Apparatus Design Details	125
A.1 – PCM Chamber.....	125
A.2 – Capture/Recovery Flow Channel	126
A.3 – Refrigerated Bath	128
A.4 – Pump	130
A.5 – Flow Meter	131
A.6 – Thermocouples.....	133
A.7 – Heat Flux Sensors	133
A.8 – DAQ.....	135
APPENDIX B – Experimental Procedure	137
B.1 – Cell Assembly	137
B.2 – Plumbing and Sensor Connections.....	138
B.3 – Addition of PCM.....	139
B.4 – Cell Warm-Up	140
B.4 – Capture Test	141
B.5 – Stabilization.....	141
B.5 – Recovery Test.....	141
APPENDIX C – Calibration and Error Analysis.....	143
C.1 –Material Property Data	143
C.2 – Scale (PCM Mass Measurement).....	143
C.3 – PCM Thermocouples.....	144
C.4 – Flow Meter	145
C.5 – Heat Loss to Surroundings	146
C.6 – Heat Flux Sensors.....	147
C.7 – Flow Temperature	148
APPENDIX D – CFD Model Set-Ups.....	149
D.1 – Two Dimensional Base Case	149
D.2 – Two Dimensional Parametric Cases	153
D.3 – Three Dimensional Lauric Acid Cell	154

LIST OF TABLES

Table 2.1: Low temperature phase change material properties (Zalba et al., 2003).	17
Table 2.2: Phase change materials with melt temperatures between 50°C and 90°C (Ref. 1–Zalba et al., 2003, Ref. 2–Kenisarin & Mahkamov, 2007).	17
Table 2.3: Phase change mixtures with melt temperatures between 50°C and 90 °C (Zalba et al., 2003).	18
Table 2.4: Commercially available phase change materials (Kenisarin and Mahkamov, 2007).	19
Table 2.5: Symbol definitions for equations 3 through 6.	22
Table 2.6: Mathematical models for phase change energy storage (Verma et al., 2008).	23
Table 2.7: Capture system characterization matrix.	26
Table 3.1: Material properties for the two-dimensional CFD base case.	40
Table 3.2: Grid independence results for three-dimensional CFD PCM chamber.	59
Table 5.1 Comparison of half-melt time predictions for tests 1 and 2 with CFD, and analytical models.	84
Table 6.1: Time-of-day electricity pricing in Ontario, January 2009 (Ontario Energy Board, 2009).	97
Table 6.2: List of PCM candidates with melt temperatures between 60 and 70 °C.	102
Table 6.3: Estimated natural gas usage per month [therms] at McMaster Innovation Park (Sandwell Consulting, 2008).	104
Table 6.4: Required PCM mass and cost to store 91 GJ of latent thermal energy.	105
Table 6.5: Common inputs for the thermal energy storage system for McMaster Innovation Park.	107
Table 6.6: Phase change material inputs for the thermal energy storage system.	107
Table 6.7: Model outputs for the RT65 thermal energy storage system for several geometries.	108
Table 6.8: Model outputs for the stearic acid thermal energy storage system for several geometries.	108
Table 6.9: Summary of Distributed Storage Systems A and B, with and without storage compression.	114
Table 7.1: Summary of successfully tested ranges for model input parameters.	117
Table 7.2: Additional model limitations and recommendations for use.	117
Table A.1: General and thermal properties of Makrolon polycarbonate (Makrolon, 2009).	126
Table A.2: Temperature specifications for the Neslabs RTE 110 refrigerated bath (Neslabs, 1993).	128
Table A.3: Physical specifications for the Neslabs RTE 110 refrigerated bath (Neslabs, 1993).	129
Table A.4: Pump specifications for the RK-07012-20 miniature gear pump (Cole Parmer, 2009).	130
Table A.5: Flow meter calibration constants for the FP-5062 Micro-Flow Sensor (Omega, 2007).	131
Table A.6: Electrical properties and responses of the HFS-4 heat flux sensors (Omega, 2005).	135
Table C.1: Melt temperature variation for different grades of stearic acid.	143
Table C.2: Flow meter calibration data.	144
Table C.3: Flow meter calibration data.	145
Table D.1: Fluent input parameters for the CFD model base case.	149
Table D.1 continued: Fluent input parameters for the CFD model base case.	150
Table D.2: ANSYS-Fluent 6.3.26 set up parameters for 2D flow solution.	151
Table D.2 continued: ANSYS-Fluent 6.3.26 set up parameters for 2D flow solution.	152
Table D.3: ANSYS-Fluent 6.3.26 set up parameter changes for 2D energy solution.	152
Table D.4: ANSYS-Fluent 6.3.26 set up changes for the 2D parametric energy solutions.	153
Table D.5: Lauric Acid CFD model boundary conditions and material properties.	154
Table D.5 continued: Lauric Acid CFD model boundary conditions and material properties.	155
Table D.6: ANSYS-Fluent 6.3.26 set up parameters for 3D flow solution.	155
Table D.6 continued: ANSYS-Fluent 6.3.26 set up parameters for 3D flow solution.	156
Table D.7: ANSYS-Fluent 6.3.26 set up parameter changes for 3D energy solution.	157

LIST OF FIGURES

Figure 2.1: Comparison of sensible, latent and chemical energy stored in water.	11
Figure 2.2: Comparison of sensible, latent and chemical energy stored in ammonia.	11
Figure 2.3: Design methodology for solid to liquid PCM thermal storage systems.	29
Figure 3.1: Non-uniform melt distances for round tube banks (staggered and aligned, white for capture tubes, grey for recovery tubes) versus uniform melt distance for rectangular channels.	34
Figure 3.2: Two-dimensional CFD model geometry with temperature profiles for 50% liquid fraction during capture (a) and recovery (b).	40
Figure 3.3: Heat flux versus time curves 0-400 s for the rectangular and triangular meshes.	42
Figure 3.4: Change in heat flux and melt fraction vs. energy residual during a single time-step.	44
Figure 3.5: Effect of changing recovery channel thermal conductivity from 0.01 to 1000 W/mK during melt cycle.	45
Figure 3.6: Effect of changing capture channel thermal conductivity from 1 to 1000 W/mK during melt cycle.	47
Figure 3.7: Effect of changing effective PCM thermal conductivity from 0.1 to 100 W/mK.	48
Figure 3.8: Effect of changing PCM latent heat of fusion from 91,400 to 219,360 J/kg.	50
Figure 3.9: Effect of changing difference between initial and melt temperatures (1.05 to 20 °C).	51
Figure 3.10: Effect of changing the capture fluid temperature difference (2 to 50 °C).	53
Figure 3.11: CFD temperature profile at 50% melt for a ΔT Capture of 2K.	53
Figure 3.12: CFD base case temperature profile at 50% melt for a ΔT Capture of 21K.	54
Figure 3.13: Effect of changing the capture fluid convective heat transfer coefficient from 10 to 10,000 W/m ² K.	56
Figure 3.14: Sliver elements at junction of rounded and non-rounded parts.	58
Figure 3.15: Lauric Acid storage cell CFD model geometry.	58
Figure 3.16: Lauric Acid storage cell CFD mesh transverse cross-section.	59
Figure 3.17: Lauric Acid storage cell CFD mesh lateral cross-section, inlet end.	60
Figure 4.1: Schematic of the phase change material test cell.	64
Figure 4.2: Flanged modular PCM chamber design.	67
Figure 4.3: Flat backing plate with temperature measurement locator baffle.	68
Figure 4.4: Electrical resistance analogy diagram for calculating the heat transfer resistance of a phase change material cell.	69
Figure 4.5: CFD flow distribution 3mm from the channel bottom for 0.26 L/min flow.	72
Figure 4.6: CFD flow distribution 3mm from the channel bottom for 1.6 L/min flow.	73
Figure 4.7: Thermocouple positioning hole pattern in the central baffle (thermocouple spacing in melt front propagation distance is 1.8 mm).	74
Figure 4.8: Temperature profiles near the baffle in the three-dimensional CFD study.	75
Figure 4.9: Position of heat flux sensors in the experimental set-up.	77
Figure 5.1: Lauric acid test 1 melt time results compared to analytical and CFD models.	84
Figure 5.2: Lauric acid test 2 melt time results compared to analytical and CFD models.	85
Figure 5.3: Repeatability comparison of lauric acid tests 1 and 2 melt time results.	87
Figure 5.4: Lauric acid test 1 heat flux results compared to analytical and CFD models.	87
Figure 5.5: Lauric acid test 2 heat flux results compared to analytical and CFD models.	88
Figure 5.6: Lauric Acid test 3 melt time results compared to the analytical model.	90
Figure 5.7: Lauric Acid tests 3 and 4 comparing flow direction for 1.6 LPM capture flow.	92
Figure 6.1: Schematic representation of the H ₂ Green Distributed Storage System.	96
Figure 6.2: Design methodology for H ₂ Green Distributed Storage System thermal battery.	99
Figure 6.3: Cell material cost versus charge time for stearic acid and RT65 cells.	109
Figure 6.4: Capture cycle heat flux over time for 6-hour stearic acid capture cell.	110
Figure 6.5: Net capture cycle heat flux using 6-hour stearic acid capture cells staggered at 15 minute intervals.	111

Figure 6.6: Recovery cycle heat flux over time for 6 hour stearic acid capture cell (1 hour recovery time) with an average bulk recovery fluid temperature of 25 °C.	111
Figure A.1: PCM chamber dimensions.	125
Figure A.2: Capture/recovery flow channel external dimensions in millimetres.	127
Figure A.3: Capture/recovery flow channel internal dimensions in millimetres.	127
Figure A.4: Wiring diagram for the FP-5062 Micro-Flow Sensor (Omega, 2007a).	131
Figure A.5: Pressure drop across the FP-5062 Micro-Flow Sensor (Omega, 2007).	132
Figure A.6: Dimensions of the FP-5062 Micro-Flow Sensor (Omega, 2007).	132
Figure A.7: Specifications of the FP-5062 Micro-Flow Sensor (Omega, 2007).	132
Figure A.8: Layered construction of the HFS-4 heat flux sensors (Omega, 2005).	134
Figure A.9: Dimensions of the HFS-4 heat flux sensors (Omega, 2005).	134
Figure A.10: Position (mm) of the heat flux sensors on the capture/recovery channel surface.	135
Figure A.11: Type T thermocouple data acquisition error for the NI-9213 module.	136
Figure C.1: Heat loss to surroundings under natural convection.	147
Figure D.1: Model boundaries for the two-dimensional CFD cases.	150

NOMENCLATURE

Symbols

A	Area [m^2]
C _p	Heat Capacity [J/kgK]
d	Derivative (i.e. dx/dt)
D	Diameter [m]
e	Base of the Natural Logarithm
E	Energy [J]
erf	Error Function
erfc	Complimentary Error Function
f	Heat Flux Density [W/m^2]
h	Heat Transfer Coefficient [W/m^2K]
h _{sl}	Latent Heat of Fusion [J/kg]
[J]	Joules
k	Thermal Conductivity, [W/mK]
[K]	Kelvin
[kg]	Kilograms
L	Latent Heat of Fusion [J/kg]
ℓ	Length [m]
m	Mass [kg]
\dot{m}	Mass Flow Rate [kg/s]
[m]	Meters
Q	Heat Flux [W]
q''	Heat Flux Density [W/m^2]
s	Position of the Solid-Liquid Interface [m]
[s]	Seconds
t	Time [s]
T	Temperature [K]
U	Temperature Distribution [K]
V	Wall Temperature Difference [K]
[W]	Watts [J/s]
x	Position [m]
α	Thermal Diffusivity [m^2/sK]
δ	Partial Derivative (i.e. $\delta x / \delta t$)
γ	Melt Fraction []
κ	Thermal Diffusivity [m^2/sK]
λ	Eigen function
μ	Kinematic Viscosity [kg/ms]
Π	Pi (3.14159...)
ρ	Density [kg/m^3]
τ	Temperature Difference [K]
v	Dynamic Viscosity [m^2/s]
Φ	Temperature Distribution [K]

Subscripts

1	Liquid Phase
2	Solid Phase
al	Aluminum
C	Capture
cs	Cross Sectional
<i>eff</i>	Effective
H	Hydraulic
i	Initial
m	Melt
PCM	Phase Change Material
R	Recovery
SC	Subcooling
SH	Superheat
sl	Solid/Liquid
ss	Stainless Steel
store	Storage Value
tube1	Tube Inner Wall
tube2	Tube Outer Wall
w	Wall Value

GLOSSARY

Availability	The potential for a given quantity of thermal energy to be converted into work.
Capture System	The system from which thermal energy is collected for storage in a thermal battery.
Cell Charge Time	The amount of time required to fully melt the phase change material and impart any desired sensible heat into a single cell within a thermal battery.
Complementary Error Function	One minus the Error Function $erfc(x) = 1 - \frac{2}{\sqrt{\pi}} \int_0^x e^{-t^2} dt$
Cogeneration	Simultaneous production of both electricity and useful thermal energy.
Convective Heat Transfer Coefficient	A coefficient that relates the heat flux during convective heat transfer to the difference between the bulk fluid temperature and wall temperature.
Distributed Storage System	An energy storage system that is located at the end-user site.
Duty Cycle	The timing of thermal battery charge, storage and recovery based on the capture and recovery system on/off timing.
Effective Thermal Conductivity	The value (k_{eff}) calculated by dividing the heat transfer through the phase change material chamber wall by the average temperature slope in the phase change material $((T_m - T_w)/s)$.
Electrohydrodynamics	The study of the effect of electric fields on fluid flow
Error Function	Mathematical function defined as: $erf(x) = \frac{2}{\sqrt{\pi}} \int_0^x e^{-t^2} dt$
Expected Error	The expected error in a measurement calculated by adding the root squared of all possible error sources at their expected or experimentally determined values.
Form-Stable	Able to keep a constant shape without external encapsulation, even after melting of the integral phase change material has occurred
Freezing Temperature	The temperature at which a pure material changes from liquid to solid at atmospheric pressure.

Lauric Acid	A fatty acid with potential for use as a phase change material ($T_m \sim 317$ K).
Liquidus Temperature	ANSYS-Fluent term for melt temperature of any pure material or mixture
Maximum Error	The maximum possible error in a measurement calculated by adding the root squared of all possible error sources at their maximum values.
Melt/Melting Temperature	The temperature at which a pure material changes from solid to liquid at atmospheric pressure.
Mushy Zone	A region of partially solid and partially liquid material during a melting or solidification process.
Normalized_m³	Normalized cubic meters (as if the temperature and pressure were atmospheric).
Phase Change Material (PCM)	A substance that is used to store energy as latent heat via a change of phase.
Rankine Cycle	A cyclical process of changing the pressure, temperature and phase of a fluid (usually water) to extract mechanical energy (usually through a steam turbine) from thermal energy.
Recovery System	The system to which thermal energy is imparted from storage in a thermal battery.
Seebeck Effect	The thermoelectric phenomenon that causes electrons to flow through a circuit connecting two materials at different temperatures.
Solidus Temperature	ANSYS-Fluent term for freezing temperature of any pure material or mixture.
Standard Deviation	A statistical value for a normally distributed data set defined as the square root of the variance.
Stearic Acid	A fatty acid with potential for use as a phase change material ($T_m \sim 341$ K).
Super-Cooling	The degree of cooling below the melt temperature that a material or mixture can undergo before solidification occurs.
Thermal Battery	A thermal energy storage system that decouples the production of thermal energy from its usage in both space and time.
Thermal Cycling	Raising and lowering the temperature of a material several times (usually transitioning from solid to liquid and back each time for a phase change material).
Thermo-Electric Generator	Devices that use the Seebeck effect to generate electricity from thermal energy.
Variance	The amount that a data point deviates from the mean value of the entire data set.

CHAPTER 1 – Introduction

1.1 – Background

With the shift of focus in the energy industry towards more efficient and sustainable generation, transmission and usage of power, reducing waste has become an important area of research and development (MacCracken, 2009). Thermodynamics teaches us that all process inefficiency eventually manifests itself as thermal energy. In most processes, excess thermal energy is released to the atmosphere or a large body of water to complete a cyclic process or prevent overheating of components or facilities. Although excess thermal energy is impossible to completely eliminate, it has the potential to be harvested and used for applications that would otherwise require additional energy input from other sources. This method of energy transfer is not presently widely employed for several reasons. The two most significant of these are that the industry or utility that is producing the excess thermal energy is often not able to use it all at the time it is available, and that creating thermal energy from combustion of fossil fuels has historically been inexpensive. This means that recovering unused thermal energy does not decrease the energy usage of the system the designer is concerned with, their own facility, and low fossil fuel prices do not motivate others to seek alternate sources of thermal energy. An increase in overall system efficiency from excess thermal energy recovery would only be seen on a much larger scale in most instances, when the system analyzed is a community or region and the energy inputs from all sources are considered.

Due to the low fossil fuel prices, there is presently no thermal energy market to encourage the harvest and trade of excess thermal energy. The transfer of thermal energy as a commodity would minimize the traditional thermal energy generation requirements, including the use of electricity and the chemical energy in fossil fuels to supply the heating requirements of residential and industrial customers. Locating and quantifying the production and utilization of thermal energy on a regional scale would allow a more comprehensive energy system model to be developed in order to identify potential efficiency improvements in various communities. It would also allow for small and large thermal energy recovery systems to be used such that thermal storage and transport can be accomplished on all scales. Some of the technologies required to make this possible include thermal storage batteries and transport systems for thermal energy.

1.2 – Current Applications of Thermal Storage

Thermal storage is becoming more popular as energy efficiency gains importance on the global stage. From before the invention of refrigeration systems, the thermal storage capacity and insulative properties of the earth have been used to keep food and ice cool during the summer in root cellars and ice houses. More recent applications of thermal energy storage include phase change material impregnated wallboard or concrete, seasonal thermal storage and regulation of facility temperatures. Phase change material impregnated wallboard and concrete are used in construction of buildings to store thermal energy during the day as the phase change material melts and keep buildings warm at night through the solidification of the phase change material. They are created by filling

hollow spaces inside the wallboard or concrete with pockets of phase change material. Seasonal thermal energy storage using soil around boreholes or water tanks to store the summer thermal energy for winter use is less common due to the large volumes required to store seasonal energy. It is also becoming more common to see the use of bricks to store electrically generated thermal energy when the cost is lower and the use of large-scale chilled water or ice systems to shift cooling energy use to off-peak hours. Several large-scale cooling systems are already in use and can be found around the world. The 5 million square foot (1.5 million m²) McCormick Place in Chicago, Illinois, along with several neighbouring buildings, have an 8.5 million gallon (32 million litre) chilled water system (Bush and Wolf, 2009) with a storage capacity of 123,000 ton-hours, equivalent to 430 MW-hours or 156×10^{12} J of thermal storage (Engineered Systems, 2000). Again in Chicago, three ice storage facilities, which freeze water at night and have a total capacity of 259,000 ton-hours (910 MW-hours or 3.28×10^{12} J), cool many of the downtown buildings during the summer through a secondary chilled water distribution system (Williams, 1998). Each of these facilities is the size and shape of a small office building and constructed to blend in with the local architecture. The Andasol 3 parabolic solar facility in Spain uses a 28,500 kg eutectic salt phase change material thermal storage system to store enough energy to run the turbines at full load for up to 7.5 hours when the sun is not shining (Solar Millennium, 2008). Each of these facilities uses thermal energy storage to enable the energy to be used whenever it is available or when it is economically optimal.

Energy efficiency is not, however, the only motivator for the use of thermal storage. Comfort and convenience have also spawned some interesting uses of thermal energy storage. In order to keep soldiers and other labourers (including animals) who must work in hot climates more comfortable and effective, several companies offer vests and other articles of clothing filled with phase change materials to keep the worker at a constant temperature. One such vest maintains a temperature of 59 °F (15 °C) for up to 2.5 hours, at which time a freshly charged set of cooling packs can be inserted (Glacier Tek, 2009). This vest weighs less than 5 lbs (2.3 kg) and the cooling packs require 20 minutes to recharge at 32 °F (0 °C (Glacier Tek, 2009). A similar application of phase change material thermal storage is a coffee cup that keeps hot beverages at a constant, desirable temperature for a long period of time (Salton, 2009).

The food, medical and electronics industries also use the thermal storage in phase change materials for temporary protection of goods. Rather than using expensive back-up generators to ensure that sensitive electronics installations stay cool during a primary power outage, phase change materials can be included in the enclosure to ensure thermal protection for a given period of time. A phase change material thermal storage system can also be used to dissipate thermal energy from the enclosure at night to reduce or eliminate the cost of cooling during the day (Intertec, 2009). This same principle is used to ensure food and medical products are kept at their optimum temperature during transport to avoid spoilage. Containers with integral phase change materials that melt/solidify at the optimum temperature of the goods can be used as an alternative to

expensive environmental control systems for transportation during a given period of time (Drage, 2009).

1.3 – Potential Applications of Thermal Storage

With the proliferation of time-of-day electricity pricing in much of the world to account for peak system requirements, the number of potential sites for thermal energy storage is growing. While large-scale thermal energy storage sites currently exist, the greatest potential for development in this area is in transportable systems. An example of this would be a truck, train car or ship that captures thermal energy from a power plant or large industrial installation and then moves to a city centre to recover the thermal energy to a communal distributed heating system or absorption system for cooling. Using this technique, several thermal energy sources can be transferred to a central facility and used to feed a single or group of recovery systems in order to mitigate the risk if one of the sources stops producing thermal energy. If there is excess thermal energy from such a system during certain times of the year, it can be used to reduce energy input to other systems. This could include preheating water for hot water systems or snow and ice melt systems during winter months in parking lots or on airport runways.

Another group of potential applications for thermal storage is increasing the overall efficiency of distributed storage systems for storage of off-peak electrical energy for recovery during peak times. These systems would allow on-site conversion of electrical energy into an appropriate storage medium (pumped hydro, hydrogen, compressed gas, etc.) and then regeneration of electricity. This can not only reduce the

cost of electricity based on time-of-day pricing, but also reduces the peak generating requirements of the electrical grid. Due to the round-trip storage efficiency of such systems causing energy losses, as well as transmission losses, additional sources of revenue are often necessary to justify the system cost. One of the simplest sources of revenue to consider is the displacement of space heating costs. This transforms the inefficiencies in the storage and recovery process into useful thermal energy for heating and absorption cooling applications and reduces the electricity or fossil fuels required to keep a facility at a comfortable temperature.

Combined heat and power applications could also benefit greatly from thermal storage systems. This would allow the generation of heat to be decoupled both spatially and temporally from its use. Facilities that have large electricity demands could store and transport excess thermal energy to off-site locations for recovery. Conversely, smaller systems could be sized based on the thermal energy requirements of a building with electricity used during peak times and any excess sold back to the grid. This would allow the high availability chemical energy in fossil fuels to be used to generate high availability electricity with only the resulting inefficiencies put towards low availability space heating.

Thermal energy from some processes could also be used to generate electricity. This can be done using conventional steam generators if the temperature is high enough. An organic Rankine cycle, which operates the same way as the Rankine cycle used in steam generation but uses a fluid with a lower evaporation temperature, can be used to generate electricity from sources at lower than steam generation temperatures. Another

option for electricity generation directly from thermal energy is using Thermo-Electric Generators (TEGs). These devices operate on the Seebeck effect, promoting electron flow through two materials connected by an electric circuit and subjected to a temperature differential (Seebeck, 1895). Even when thermal energy is used to directly generate electricity it is still beneficial to be able to store the thermal energy until such a time when grid electricity is at its most expensive.

1.4 – Problem

With the development of thermal storage and transport technologies, the utilization of by-product thermal energy can be decoupled from the primary process that created it, both temporally and spatially, allowing it to be utilized when and where it is needed. This removes one of the major hurdles currently preventing the widespread use of cogeneration. The creation of a Thermal Energy Market would also lead to more widespread use of thermal energy storage and transport, as revenue can be generated from excess thermal energy that is currently released into the atmosphere. This not only creates an additional source of income for some companies and reduces heating costs and emissions from fossil fuel combustion for others, but also increases the overall efficiency of a community, city or region. These technologies also have the advantage of helping mediate intermittent sources of energy, such as wind and solar, in order to meaningfully integrate them into the current generation capacity.

This study focuses on the storage of low temperature thermal energy that cannot be used to produce electricity via steam generators. Materials and methods for thermal

storage are discussed, a mathematical model developed and a feasibility study performed on a distributed storage system (DSS), which will be described in Chapter 6. The system model is also used to analyze the parametric behaviour of thermal storage systems to determine which improvements would produce the most benefit to the system and which research areas are the most beneficial. The creation of such a model aids designers in evaluating thermal energy storage systems for a wide variety of potential applications. While many mathematical models currently exist for predicting melt and solidification times in phase change material cavities (Verma et al., 2008), they are not widely used in industry for preliminary assessments and sizing due to their dependence on specific geometry information. The models summarized by Verma et al. (2008) based on the first law of thermodynamics use an energy balance to determine temperature and heat flux profiles throughout the phase change thermal storage system. As the models based on the second law of thermodynamics, which use the principle entropy generation, have not been experimentally validated and are not particularly useful for sizing operations, they were not considered here. The creation of a simple and easy to communicate model that can be used for initial sizing of a phase change material battery will help promote widespread consideration of thermal energy storage systems to help uncover additional applications for this technology.

1.5 – Scope of Work

The scope of this study was the development of an analytical model to facilitate prediction of the size of a phase change material thermal storage system. The only inputs

to the model are specifications of the capture and recovery systems, including timing for the capture and recovery needs, and properties of the phase change material selected.

This allows preliminary sizing without detailed geometric design. The focus was on solid to liquid phase changes at temperatures between 50°C and 90 °C. This is a particularly interesting and challenging range for thermal energy use because it is too low to generate steam to run through a turbine. It is, however, attractive for space heating as the range is well above the air temperature required for indoor air. Storage of thermal energy at these temperatures would allow it to be used at a different time than it is produced. It also opens up the possibility of transporting it to another location with minimal losses for use elsewhere.

The figure of merit used to determine the usefulness of the model was the melt time calculation for a given configuration. The analytical model melt time sensitivity was compared to computational fluid dynamics results using the same assumptions to ensure that the model has the correct responses to changes in the input parameters. The base case was then validated experimentally to ensure reasonable agreement of the analytical model and computational fluid dynamics simulations.

CHAPTER 2 – Thermal Storage Technologies

2.1 – Thermal Storage Options

There are three main methods of storing thermal energy in any material: reversible chemical energy, sensible thermal energy and latent thermal energy. Chemical energy is absorbed or released when a chemical reaction occurs in a material, thus changing the organization of the molecules. If this process is reversible, it can be used to capture and recover energy. An example of this is splitting water into its component gases, diatomic oxygen and diatomic hydrogen and then recombining them into water. This can also be done to ammonia through the reversible Haber process (Soda-Fabrik, 1910) by combining and separating the nitrogen and hydrogen atoms.

Sensible thermal energy is stored through increasing the vibrational energy of the molecules in a substance, which manifests itself as an increase in temperature. The ability of a material to store sensible energy is represented by the heat capacity (the amount of energy required to raise the temperature of one kilogram of the material by one Kelvin).

Latent thermal energy is the energy required to bring about the reorganization of molecular structure that accompanies a change of phase. The phase change can be solid-solid, solid-liquid, solid-gas or liquid-gas. A comparison of the energy that can be stored in chemical, sensible and latent forms for water is shown in figure 2.1 and for ammonia in figure 2.2.

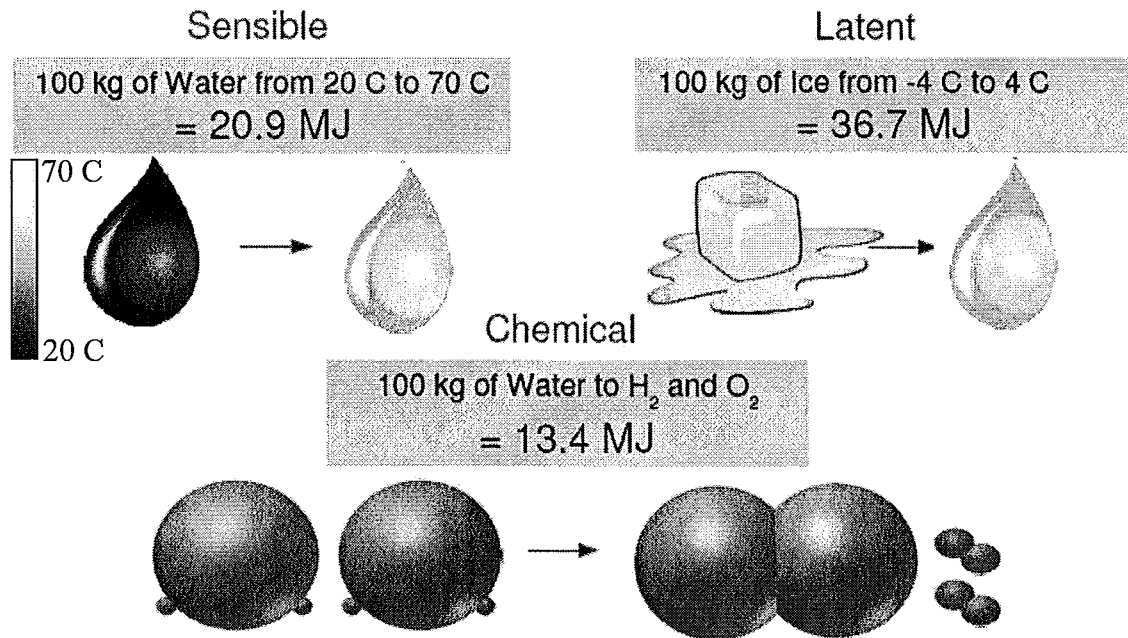


Figure 2.1: Comparison of sensible, latent and chemical energy stored in water.

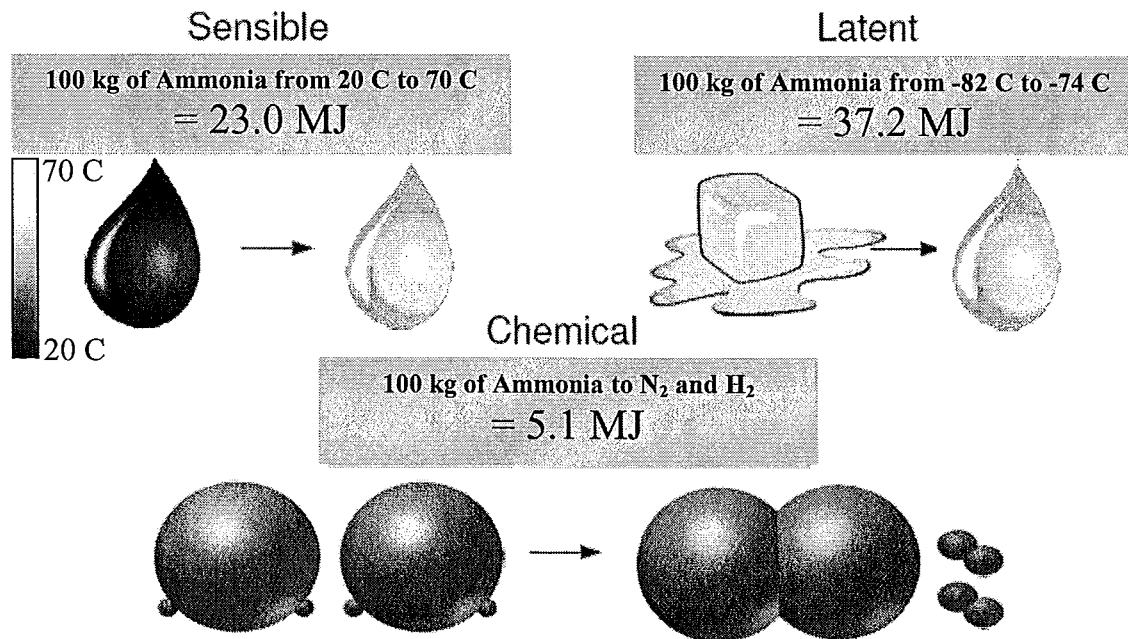


Figure 2.2: Comparison of sensible, latent and chemical energy stored in ammonia.

Because of the relatively large amount of energy that can be stored as latent heat in a material this was used as the primary storage mode in the design of the thermal batteries. The complexities associated with chemical reactions, such as by-products, catalysts and secondary reactions, can also be avoided by utilizing latent thermal energy storage. Sensible thermal energy storage was not used as the main method, but may still be used in certain systems to store some additional energy at peak generation periods without increasing the size of the system. This is dependent on the temperatures of the capture and recovery systems as it requires a large enough temperature gradient to drive the thermal energy into the phase change material after it has surpassed its melt temperature.

2.2 – Phase Change Material Categories

The use of latent heat as the primary thermal energy storage medium requires a survey of available materials and their relevant properties. Since all materials undergo phase changes, criteria and constraints have been clearly defined based on the system requirements to narrow the number of candidate materials. The first decision is the type of phase change to be employed.

Solid-liquid, solid-gas, solid-solid (this only occurs in a few materials that change molecular structure under specific conditions) or liquid-gas are available as phase transformations. In order for the system to be as simple and compact as possible, the volume difference between the two phases should be minimized. This means that using a gas phase would require compression, thus requiring additional energy and reducing the

storage efficiency. For this reason, solid-gas and liquid-gas phase changes were not considered in this study. This leaves solid-liquid and solid-solid phase change as the two candidates. Solid-solid phase changes only occur in a few materials, such as the n-alkanes, while solid-liquid phase changes can occur in any material. In general, a solid-liquid phase change has a higher latent heat than a solid-solid phase change due to the larger difference in molecular organization and was therefore chosen as the focus of this research. There is potential, however, to utilize a solid-solid phase change as a secondary storage mechanism in a material with favourable solid-liquid transition properties, but this opportunity is not usually available.

2.3 – Low Temperature Phase Change Materials

Given that solid-liquid phase change was chosen, the first constraint on material selection was the melt temperature. The range of acceptable melt temperatures was determined through a preliminary system analysis of the proposed capture and recovery systems. Since this study focused on the applications that lie below steam generation temperatures but above ambient air temperatures, the melt range specified was 50 °C to 90 °C. Since the second law of thermodynamics dictates that temperature difference is the driver for heat transfer, the melt temperature of the phase change material was set sufficiently below the input temperature of the capture fluid to remove as much thermal energy as possible, but also sufficiently above the desired final temperature of the recovery fluid to ensure a reasonable residence time in the thermal battery. The longer the residence time of the capture or recovery fluid in the thermal battery, the closer the

fluid exit temperature will be to the melt temperature of the phase change material but the longer the fluid channel must be for a given flow rate and cross-sectional channel geometry. Longer fluid channels cause higher pressure drop and therefore add parasitic losses to a system. The next criterion met by the phase change material was chemical stability for the required number of thermal cycles. Assuming that heat is stored from the capture process overnight and used each day in the recovery process and that the product should have a lifetime of at least 30 years without replacement, the required number of thermal cycles is 10950. This is over ten times the 1000 test cycles recommended by Kenisarin & Mahkamov (2007). It was therefore difficult to determine if a material could withstand this many cycles from currently available data. When candidate phase change materials and corresponding construction materials were chosen, further investigation to determine the thermal cycle and corrosion lifetime of the system in order to assess potential refurbishment costs was recommended since limited information was available.

The remaining parameters considered in the choice of a phase change material, as outlined below (Kenisarin & Mahkamov, 2007), were criteria rather than constraints and a balance between them to achieve an optimized system was found.

- High heat of fusion and specific heat per unit volume and mass
- Low vapour pressure at operating temperature to prevent evaporation
- Compatible with common containment materials
- Non-hazardous, non-flammable and non-toxic
- Small degree of super-cooling and high rate of crystal growth
- Small volume variation on solidification

- High thermal conductivity
- Abundant supply at low cost

Many of the desired properties on this list can be achieved through innovative system and component design, but others are integral to the operation of the thermal storage system and are not functions of design. The two most important properties on this list that can be used to rate candidate phase change materials are latent heat of fusion and cost. These cannot, however, be simply compared per unit mass or volume, but the size and cost of the optimized system that results from their selection must be analyzed. The cost of the phase change material itself is difficult to evaluate, as the very large size of these systems may warrant the creation of a dedicated production facility. This would significantly change the cost of the phase change material.

The size of the system is largely based on a combination of heat transfer surface design and the effective thermal conductivity of the phase change material. Effective thermal conductivity is defined as a representative value of the coefficient k_{eff} in equation 1 that includes the effects of all heat transfer enhancements, such as additives, natural convection cells or mechanical or electrohydrodynamic mixing.

$$Q = k_{eff} \frac{dT}{dx} \quad (1)$$

Effective thermal conductivity is a way to approximate a heat transfer region as if it were conduction in a pure material. This is most applicable to heat transfer enhancements such as homogeneous mixtures of different materials (i.e. nanoparticles suspended in the phase change material), but can also be applied to enhancements such as fins, nanotubes and impregnated foams as long as these enhancements produce effects

that are similar to a change in thermal conductivity. It is possible that for natural convection currents or other heat transfer enhancements that k_{eff} would be a function of time for a given storage cell configuration. Effective thermal conductivity, along with design options to improve effective properties, is further discussed in the proceeding section. Preliminary engineering calculations can be made, however, to eliminate some of the candidate materials. The advantages and disadvantages of organic and inorganic phase change materials are presented in Table 2.1, and show that both have drawbacks. Since the heat of fusion (called phase change enthalpy in the table) and cost are the two most important factors, it is difficult to eliminate either of these categories as both contain high heat of fusion and low cost options. The selection process therefore continued with options in both of these categories. Further subdivisions of the materials were made into eutectics, non-eutectics and fatty acids. Tables 2.2 and 2.3 show examples of low temperature phase change material candidates in these sub-categories found in literature summaries (Zalba et al., 2003 and Kenisarin & Mahkamov, 2007). Available properties have been listed, although much of the information required to properly evaluate each phase change material is not currently available in the literature. The most important property, melt temperature, is available for all materials and accounts for the bulk of the elimination process, although allowances were made for slight variations due to differences in material grade and purity.

Table 2.1: Low temperature phase change material properties (Zalba et al., 2003).

	Organic Materials	Inorganic Materials
Advantages	Non-Corrosive	Higher Latent Heat of Fusion
	Lower or No Super-cooling	
	Chemically Stable	
	Thermally Stable	
Disadvantages	Lower Latent Heat of Fusion	Higher Super-cooling
	Lower Thermal Conductivity	Corrosive
	Flammable	Prone to Phase Segregation
		Lack of Thermal Stability

Table 2.2: Phase change materials with melt temperatures between 50°C and 90°C (Ref. 1–Zalba et al., 2003, Ref. 2–Kenisarin & Mahkamov, 2007).

Compound	Category	Melt Temp [C]	Heat of Fusion [kJ/kg]	Thermal Conductivity [W/mK]	Density (Solid) [kg/m ³]	Density (Liquid) [kg/m ³]	Ref.
Zn(NO ₃) ₂ 2(H ₂ O)	Inorganic	54					1
NaOH H ₂ O	Inorganic	58					1
Na(CH ₃ COO) 3(H ₂ O)	Inorganic	58	226		1450		1
		58	247	0.66	1450	1280	2
Cd(NO ₃) ₂ 4(H ₂ O)	Inorganic	59.5					1
Fe(NO ₃) ₂ 6(H ₂ O)	Inorganic	60					1
NaOH	Inorganic	64.3	227.6		1690		1
Na ₂ B ₄ O ₇ 10(H ₂ O)	Inorganic	68.1					1
Na ₃ PO ₄ 12(H ₂ O)	Inorganic	69					1
Na ₂ P ₂ O ₇ 10(H ₂ O)	Inorganic	70	184				1
Ba(OH) ₂ 8(H ₂ O)	Inorganic	78	268	0.66	2070	1937	1
AlK(SO ₄) ₂ 12(H ₂ O)	Inorganic	80					1
KAl(SO ₄) ₂ 12(H ₂ O)	Inorganic	85.8					1
Al ₂ (SO ₄) ₃ 18(H ₂ O)	Inorganic	88					1
Al(NO ₃) ₃ 8(H ₂ O)	Inorganic	89					1
Mg(NO ₃) ₂ 6(H ₂ O)	Inorganic	89	156	0.5	1636	1550	1
		90	171	0.57			2
Paraffin C22-45	Organic	59	189	0.21	920	795	1
		56	128	0.73	1060		2
Paraffin Wax	Organic	64	173.6	0.167	916	790	1
		82	83	0.68	1200		2
Polyglycol E6000	Organic	66	190		1212	1085	1
Paraffin C21-50	Organic	67	189	0.21	930	830	1
Biphenyl	Organic	71	119.2		1166	991	1
Propionamide	Organic	79	168.2				1
Naphthalene	Organic	80	147.7	0.132	1145	976	1
Pentadecane Acid	Fatty Acid	52.5	158.6				1
Myristic Acid	Fatty Acid	57	187		990	861	1
		52	190				2
Palmitic Acid	Fatty Acid	64	186	0.16	989	850	1
		61	198				2
Stearic Acid	Fatty Acid	69	203	0.172	965	848	1
		65	185				2
Acetamide	Chemical Compound	82	263		1159	998	2

Table 2.3: Phase change mixtures with melt temperatures between 50°C and 90 °C (Zalba et al., 2003).

%	Compound 1	%	Compound 2	Category	Melt Temp [C]	Heat of Fusion [kJ/kg]	Thermal Conductivity [W/mK]	Density (Solid) [kg/m ³]	Density (Liquid) [kg/m ³]
61.5	Mg(NO ₃) ₂ 6(H ₂ O)	38.5	NH ₄ NO ₃	Inorganic Eutectic	52	125.5	0.5	1596	1515
58.7	Mg(NO ₃) ₂ 6(H ₂ O)	41.3	MgCl ₂ 6(H ₂ O)	Inorganic Eutectic	59	132	0.6	1630	1550
53	Mg(NO ₃) ₂ 6(H ₂ O)	47	Al(NO ₃) ₂ 9(H ₂ O)	Inorganic Eutectic	61	148			
14	LiNO ₃	86	Mg(NO ₃) ₂ 6(H ₂ O)	Inorganic Eutectic	72	180		1610	1590
66.6	Urea	33.4	NH ₄ Br	Inorganic Eutectic	76	161	0.33	1548	1440
	Mg(NO ₃) ₂ 6(H ₂ O)		Mg(NO ₃) ₂ 2(H ₂ O)	Inorganic Non-Eutectic	55.5				
	KOH		H ₂ O/KOH	Inorganic Non-Eutectic	99				
37.5	Urea	63.5	Acetamide	Organic Eutectic	53				
67.1	Naphthalene	32.9	Benzoic Acid	Organic Eutectic	67	123.4	0.136		

Kenisarin and Mahkamov (2007) also provided a list of the commercially available phase change materials, seen in table 2.4, however some data in this table were found to be inaccurate or out-of-date (Rubitherm, 2009). As the commercially available phase change materials are mainly for solar applications, the melt temperatures are relatively low. Since these are considered specialty chemicals and are not widely used, their cost in comparison to other chemicals can be comparatively high. The lowest cost chemicals are usually those that are commonly used in current industrial processes, such as sodium hydroxide, as large production facilities already exist.

Table 2.4: Commercially available phase change materials (Kenisarin and Mahkamov, 2007).

Trade Name	Type	Manufacturer	Melt Temp [C]	Heat of Fusion [kJ/kg]	Density [kg/m]
STL-52	Salt Solution	Mitsubishi Chemical	52	201	1.3
RT50	Paraffin	Rubitherm GmbH	54	195	
STL-55	Salt Solution	Mitsubishi Chemical	55	242	1.29
TH-58		TEAP	58	226	
ClimSel C 58		Climator	58	259	1.46
RT65	Paraffin	Rubitherm GmbH	64	207	
ClimSel C 70		Climator	70	194	1.7
PCM72	Salt Solution	Merk KgaA	72		
RT80	Paraffin	Rubitherm GmbH	79	209	
TH-89		TEAP	89	149	
RT90	Paraffin	Rubitherm GmbH	90	197	

2.4 – Recent Phase Change Material Thermal Storage Research

A literature review on the current state of the art in phase change material thermal storage showed that the bulk of the recent research focused on solar energy conversion and building materials (Khudhair and Farid, 2004). Much emphasis has been put on the preparation of form-stable solid to liquid phase change materials (Sari, 2004 and Xiao et al., 2002) that do not require additional encapsulation, but rather have a structural matrix surrounding the phase change material so that it will not change shape as it melts. This is particularly valuable for construction materials as phase change material impregnated wallboard can be produced in commonly sized sheets and then cut to size without additional encapsulation of the cut edge. An interesting subset of this research was focused on using expanded graphite foams as a form-stable matrix for paraffin based phase change materials (Sari and Karaipekli, 2007). This has the advantage of using a material with relatively high thermal conductivity to lend structure to the phase change material. Sari and Karaipekli (2007) found that the effective thermal conductivity of 10%

expanded graphite by mass in paraffin (n-docosane) was 0.82 W/mK, compared to 0.22 W/mK of the pure paraffin. This created a form-stable composite balancing the capillary forces retaining the paraffin in the open-celled graphite matrix with gravity. Mills et al. (2006) have investigated using pieces of metal tubing, aligned and randomly oriented graphite fibres and graphite foams and have achieved increases in effective thermal conductivity of up to two orders of magnitude over pure paraffin by using a graphite foam matrix.

Research into thermally stable phase change materials has produced many novel materials and mixtures that can withstand a large number of phase change cycles. One category of materials that was particularly relevant to this study was fatty acids. These chemicals occur in plants and animals and have favourable chemical and thermal properties including good stability under phase change cycling (Sari, 2006). Again, this research is mainly focused on building materials and solar energy storage due to the current demand in these areas, but is relevant to a much wider range of applications.

Early phase change material model research resulted in the one-dimensional model known as the Stefan-Neumann solution outlined in Carslaw and Jaeger (1959). This model assumes conduction only in the liquid phase and solves equation 2 subject to the preceding initial and boundary conditions:

$$\frac{\partial u(x,t)}{\partial t} = \frac{\partial^2 u(x,t)}{\partial x^2} \quad (2)$$

$u(x,t)$ = temperature of phase change material at location x and time t

Initial Condition $u(x,0) = \varphi(x)$

$\varphi(x)$ = known initial temperature profile at each location x

Stefan Boundary Condition $\frac{ds(t)}{dt} = -\frac{\partial u(s(t),t)}{\partial x}$

$s(t)$ = position of the solid-liquid interface as a function of time

Neumann Boundary Condition $\frac{\partial u(0,t)}{\partial x} = f(t)$

$f(t)$ = known heat flux at $x = 0$ as a function of time

This model results in equations 3 and 4 for the position of the solid-liquid interface and equations 5 and 6 for the temperature distributions in the liquid and solid phases, respectively. Parameter definitions for these equations can be found in table 2.5.

$$0 = \frac{e^{-\lambda^2}}{\text{erf}(\lambda)} - \frac{k_1 \kappa_2^{0.5} T_1 e^{-\lambda^2 \kappa_2 / \kappa_1}}{k_2 \kappa_1^{0.5} (V - T_1) \text{erfc}\left(\lambda \sqrt{\kappa_2 / \kappa_1}\right)} - \frac{\lambda L \pi^{0.5}}{Cp_2 (V - T_1)} \quad (3)$$

$$s(t) = 2\lambda \sqrt{\kappa_2 t} \quad (4)$$

$$V_1 = \frac{T_1}{\text{erfc}\left(\lambda \sqrt{\kappa_1 / \kappa_2}\right)} \text{erfc}\left(\frac{x}{2\sqrt{\kappa_2 t}}\right) \quad (5)$$

$$V_2 = V - \frac{V - T_1}{\text{erf}(\lambda)} \text{erf}\left(\frac{x}{\sqrt{2[\kappa_2 t]^{0.5}}}\right) \quad (6)$$

Table 2.5: Symbol definitions for equations 3 through 6.

Symbol	Definition	Dependencies
λ	Root (eigenvalue) of equation 3	$k_1, k_2, \kappa_1, \kappa_2, T_1, V, L, Cp_2$
k_1	Thermal Conductivity of the Liquid Phase	Material Property
k_2	Thermal Conductivity of the Solid Phase	Material Property
κ_1	Thermal Diffusivity of the Liquid Phase - $k_1/(\rho_1 Cp_1)$	k_1, ρ_1, Cp_1
κ_2	Thermal Diffusivity of the Solid Phase - $k_2/(\rho_2 Cp_2)$	k_2, ρ_2, Cp_2
ρ_1	Density of the Liquid Phase	Material Property
ρ_2	Density of the Solid Phase	Material Property
Cp_1	Heat Capacity of the Liquid Phase	Material Property
Cp_2	Heat Capacity of the Solid Phase	Material Property
V	Wall Temperature minus Initial Temperature	Initial Temperature
T_1	Melt Temperature minus Initial Temperature	Initial Temperature
L	Latent Heat of Fusion	Material Property

This solution is dependent on finding the root of equation 3 in order to be able to solve the position of the interface at time t . This can be done either using eigenvalue methods or iterative solvers. Unfortunately, this solution requires a constant wall temperature to solve the melt front, which may not be the case for many real capture and recovery systems. If it is used to try to predict such cases using the bulk fluid temperature as the constant wall temperature, it will under-predict the time to full melt as the heat flux during the initial phase of the heat transfer will be much higher than with natural convection. The Stephan-Neumann constant temperature model, along with computational fluid dynamics, is used to compare analytical and numerical model results and determine if there is a significant difference in calculation methods and if the trends are reasonable.

More recently, focus of model development has shifted to improving the prediction of convective heat transfer effects for given geometries. A detailed description of the currently available models is available from Verma et al. (2008) for the models listed in table 2.6 and is therefore not provided here. These models provide detailed calculations for specific system geometries. The difficulty with using most of these models lies in the available material property data. Many phase change material specifications include only properties at a single temperature and therefore do not provide

Table 2.6: Mathematical models for phase change energy storage (Verma et al., 2008).

Model Name	Dimensionality	Geometry	Steady/Transient
Shamsunder et al.	Three	Square	Transient
Hamden	Two	Rectangular	N/A
Kurkulu et al.	Two	Square	N/A
Esen et al.	Two	Cylindrical	Transient
Gong et al.	Two	Cylindrical	Transient
Costa et al.	One (with fins), Two (without fins)	Rectangular	Transient
Vakialtojjar	Two	Rectangular	Transient
Zhang et al.	One	Spherical Capsule	Transient
Benmansour et al.	Two	Spherical Capsule	Transient
Xu et al.	One	Shape-Stabilized Slab	Transient
Halawa et al.	Two	Rectangular	Transient
Sharma et al.	Two	Heat Exchanger	Transient
Trp	Two	Shell and Tube	Transient
Hed and Bellander	One	Rectangular	N/A
Dwarka and Kim	Three	Wallboard	N/A

sufficient information for these models, such as liquid density and viscosity as a function of temperature near the melting point. Another difficulty lies in using these models for initial assessment of phase change material thermal storage systems since this type of assessment occurs before detailed geometry information is available. Cell geometry

required by the two and three dimensional models is therefore not available and iterative design over a wide range of dimensions would be required. This is cumbersome for an initial assessment. One-dimensional models are therefore more appropriate for sizing and budgeting calculations.

2.5 – Capture Systems

The most commonly available systems from which low temperature thermal energy can be captured include furnaces, internal combustion engines, chemical processes, refrigeration systems, exhaust air (ventilation, micro-turbines, drying booths), and heat sinks for thermodynamic cycles, as in combined heat and power applications. The simplest ways to characterize such systems are by the heat transfer medium and whether it is an open or closed system. Open systems involve heat transfer media that are not recirculated, while closed systems involve recirculation of all of the heat transfer medium. The major difference between these two types of system is that closed systems provide an opportunity for higher efficiency as the only losses are those due to imperfect insulation, while open systems have lower efficiency due to the temperature difference required between the medium at the outlet and storage cell temperature to ensure heat transfer. The heat transfer medium can either be a solid (conduction), fluid (convection). Since this study focused on low temperature thermal energy, radiation was not considered. While using conduction to transfer the thermal energy from the capture system to the thermal battery is possible, using a fluid to transfer the thermal energy via forced convection is more common and simpler for a modular, transportable system.

This study therefore focused on two types of fluid systems, either utilizing the primary fluid that is used in the thermal energy producing process, or using a secondary heat transfer fluid with an intermediate heat exchanger. The addition of an intermediate heat exchanger reduces the temperature of the thermal energy that is delivered to the thermal battery, but this is acceptable in many cases to mitigate the effects of fouling, acid formation and corrosion that may occur in exhaust gases and corrosive liquids. The addition of a heat exchanger may, however, have negative effects on the capture system due to increased back pressure and this decision must therefore be made based on the specific system in question. When the primary heat transfer fluid is used, it may be either a liquid or a gas, but if a secondary fluid is used, it would most likely be a liquid due to improved heat transfer characteristics.

Another distinction made when characterizing the capture system is whether it is constant or variable temperature and constant or variable heat flux. Many systems will have a set operating temperature but may have variable heat flux depending on the system load. Conversely, some systems may have a set heat flux with a variable temperature to ensure all the heat is dissipated under different conditions. These considerations resulted in the matrix shown in table 2.7 for characterizing the capture system.

It is important that the thermal storage system not detract from the operation of the capture system. To ensure that the backpressure on the capture fluid is minimal, either additional pumping power can be added, which would result in increased parasitic

losses, or the pressure drop in the thermal battery can be kept as low as possible. This can be accomplished by designing the system for low Reynolds numbers.

Table 2.7: Capture system characterization matrix.

Parameter	Option 1	Option 2
System Configuration	Open	Closed
Heat Transfer Type	Convection	Conduction (not considered)
Heat Transfer Fluid Loop	Primary Fluid	Secondary Fluid
Heat Transfer Fluid Type	Liquid	Gas
Input Temperature	Constant	Variable
Input Heat Flux	Constant	Variable

2.6 – Recovery Systems

As with capture systems, recovery systems can be characterized using the matrix in table 2.7. While closed systems are reasonable for many capture systems, open recovery systems using the primary fluid are common since the thermal energy is to be used elsewhere. Some potential applications, both open and closed, include: water heating (pre-heat or full heat), building air (pre-heat, full heat or over-heat and subsequent mixing with fresh air), building radiators and absorption cooling systems.

The one additional parameter considered for the recovery system is whether or not it can use the same heat transfer medium as the capture system. If this is the case, cost and volume savings can be realized by having only one set of capture and recovery channels within the thermal battery. Separation between the two systems can be done using intelligent valve and plumbing design. The only drawback to using one set of

capture and recovery channels is that the capture and recovery cycles cannot be run through the thermal battery at the same time. This is not an issue for most thermal energy storage systems as the thermal energy can be used directly in this case and does not need to be routed through the thermal battery.

2.7 – Temperature Mediation Systems

One type of system that requires both capture and recovery to occur simultaneously is a temperature mediation system. Many thermodynamic processes require specific temperatures to operate at optimum efficiency. One example of this is an organic Rankine cycle, which has an optimum operating temperature due to the constant evaporation temperature of the fluid. Phase change material thermal storage systems can be used to mediate temperature fluctuations in the thermal energy source to ensure that the optimum operating conditions are met as often as possible. In this case, separate capture and recovery channels would be required and careful control of the charging and discharging of thermal energy for a single cell would be needed to ensure that full melt or full solidification does not occur, allowing sensible heating or cooling of the cell and drift from the optimum temperature.

2.8 – Design Methodology

The method used in this study to design solid-liquid phase change material (PCM) thermal energy storage systems is shown in figure 2.3. The analytical model outlined in Chapter 3 deals with the storage cell time and storage cell geometry portions of this

method. Grey boxes in this figure indicate the system inputs for the design that must be specified.

An example of the use of this design methodology is presented in Chapter 6, wherein it was used to design a thermal storage system for a specific application. Each step in the process was considered and the model developed in Chapter 3 is used to determine cell charge time and geometry.

During the preliminary stages of the thermal battery design, the capture and recovery systems are clearly defined. This includes defining duty cycles for each. In many instances this will be complex as conditions will change based on time of day, day of the week, outdoor conditions, electricity demand and other factors. While designing for the worst case scenario may be appropriate in some cases, it is far more efficient to target typical seasonal conditions for a thermal storage system since excess capacity is costly and does not provide a significant benefit. It should also be determined if any sensible thermal energy storage is desired. This would be an option for large temperature differences between the capture and recovery systems.

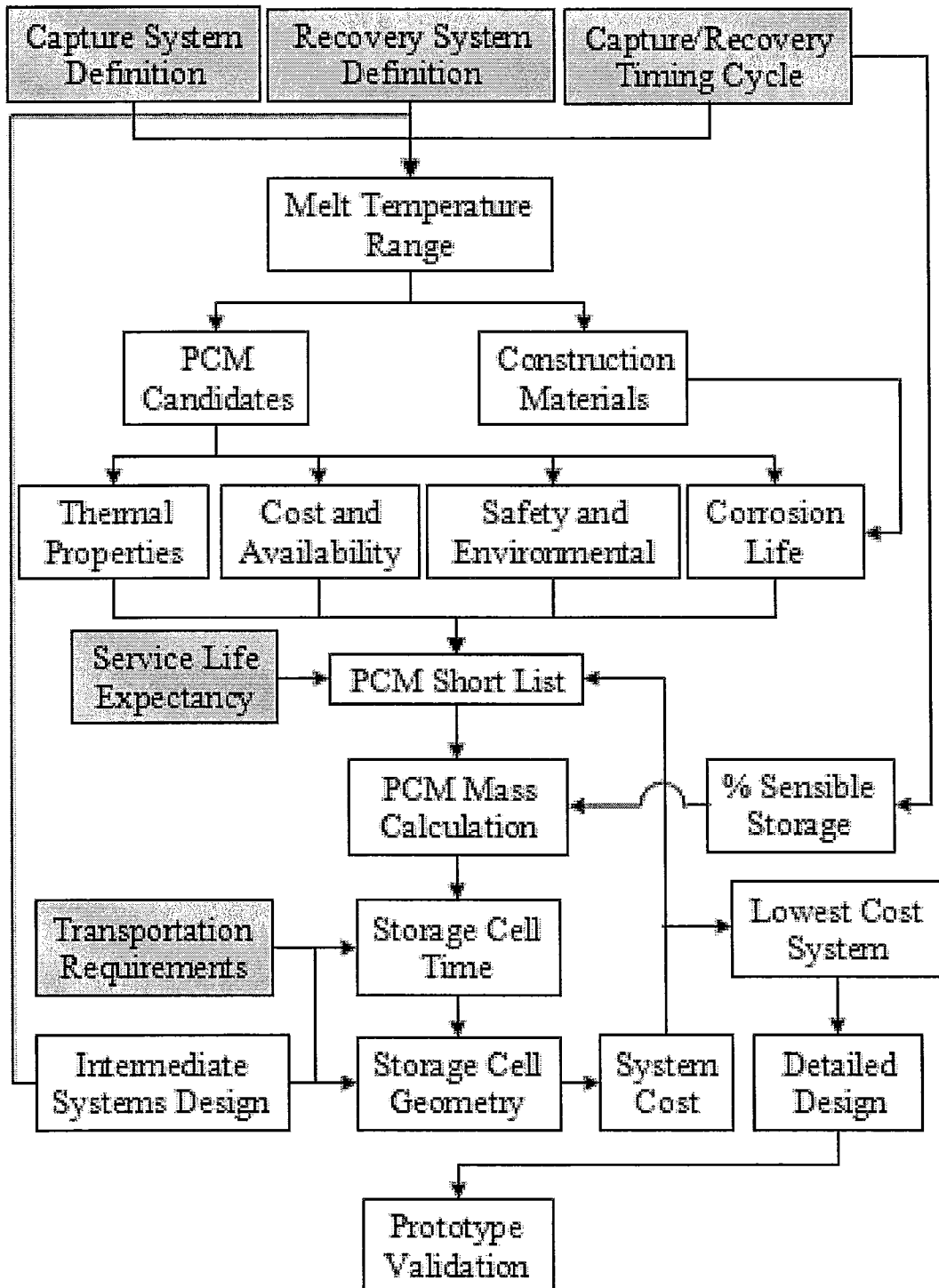


Figure 2.3: Design methodology for solid to liquid PCM thermal storage systems.

Once the design conditions and cycles are chosen for the capture and recovery systems, the melt temperature range for the phase change material can be chosen. With the chosen melt temperature range, a list of candidate materials can then be compiled. Along with the relevant heat transfer properties, each material on the list should have an approximate cost, health and safety concerns and list of compatible construction materials accompanying it. At this point, many of the materials on the list can be eliminated based on latent heat of fusion, cost or health and safety concerns if they differ significantly from the other candidates. While other properties, such as thermal conductivity and density, are also important, more weight should be given to latent heat of fusion and material cost as they have the largest effect on overall system cost.

This leaves a short list of candidate materials that will undergo a more rigorous analysis before a PCM is chosen. A requirement for the service life of the thermal battery must be set out in order to evaluate the PCMs based on thermal cycling stability. If the service life is a function of the system cost, an estimate should be made at this point based on the expected life of the phase change material and then iterative design cycles can be performed as necessary.

The latent heat of fusion of the remaining materials can be used along with the capture and recovery systems and cycles (including sensible heating where appropriate) to determine the mass of each listed PCM that would be needed to store the desired amount of energy. If a secondary fluid is being used for either of the capture or recovery cycles, the pumps, heat exchangers and plumbing can be designed at this point to determine the fluid temperature and mass flux entering the thermal battery.

Using flow data from the capture and recovery systems and the PCM properties the storage cell time can be chosen and the cell geometry determined using an appropriate analytical model or computational fluid dynamics. The cell charge time should be based on the heat removal and addition needs of the capture and recovery system, but left as long as possible to reduce costs. The transient behaviour of the capture and recovery systems as well as their duty cycles should be carefully considered when deciding on a target cell charge time. This will give a preliminary estimate of the material costs for the cell, including capture and recovery channels. This calculation can be performed for all candidate PCMs and for several storage times. Once enough model data has been collected, the PCM and geometry can be chosen from those previously analyzed. Usually the lowest cost system will be chosen, however additional considerations such as financial risk and environmental impact may affect the decision.

Detailed design calculations and prototype validation can then be done to validate some of the assumptions made in the modelling phase of the process and get a better estimate of cell charge/discharge time and cost. This detailed design and experimentation may include heat transfer surface enhancements, additives or other means of increasing the PCM effective thermal conductivity, such as electrohydrodynamic or mechanical enhancement of fluid motion. Some of these methods may result in a variable value for the effective thermal conductivity and a more advanced model or prototype iterations would need to be used to accommodate such findings.

CHAPTER 3 – PCM Thermal Storage Models

3.1 – PCM Mass

The mass of phase change material required to store a given amount of energy can be calculated using the latent heat of fusion of the PCM. This is shown in equation 7 with E_{store} as the amount of energy stored in the PCM, h_{sl} as the change in energy as the PCM changes from a solid to a liquid or liquid to a solid (also known as the latent heat of fusion) and m_{PCM} as the total mass of phase change material contained in the thermal battery.

$$m_{PCM}[kg] = \frac{E_{store}[J]}{h_{sl}[J/kg]} \quad (7)$$

In certain cases where the capture and recovery systems are at very different temperatures, it may be prudent to store some sensible thermal energy in order to reduce the size of the system. In this case, the mass of PCM will be sized using both the latent and sensible storage up to the safe operating temperature of the phase change material or capture system limits. The safe operating temperature is determined either by the degradation of the PCM, liquid to gas phase change of the PCM or limits of the construction materials. In this case, the mass of the PCM is calculated using equation 8 where ΔT_{SH} is the temperature difference above the melt temperature to which the PCM will be heated ($T_{max} - T_{melt}$) and C_p is the heat capacity of the phase change material.

$$m_{PCM}[kg] = \frac{E_{store}[J]}{h_{sl}[J/kg] + C_p[J/kgK] * \Delta T_{SH}[K]} \quad (8)$$

This simple calculation can be used as the first feasibility check to determine if space and budget are available for a PCM thermal battery.

3.2 – One-Dimensional Storage Cell Geometric Model

Once the mass of PCM required for the thermal energy storage system has been determined, the cell geometry, including the capture and recovery channels, must be determined. Since most thermal energy storage systems are large, it is feasible to assume that custom capture and recovery channels will be economical and therefore channel geometries will not be limited to commercially available dimensions. Channel thicknesses must be determined by careful consideration of pressure and corrosion requirements and flow dimensions by the desired convective heat transfer coefficient within the capture and recovery fluids. The spacing between the capture and recovery channels in which the PCM is located determines the time required to charge the individual storage cells. Since banks of round tubes would result in variable PCM thicknesses between neighbouring tubes, as seen in the upper two diagrams of figure 3.1, alternating rectangular channels will be assumed in the model. This will result in the uniform melt thickness seen in the lower diagram of figure 3.1. Using this assumption and neglecting any buoyancy and edge effects the storage cell can be modeled as one-dimensional heat transfer.

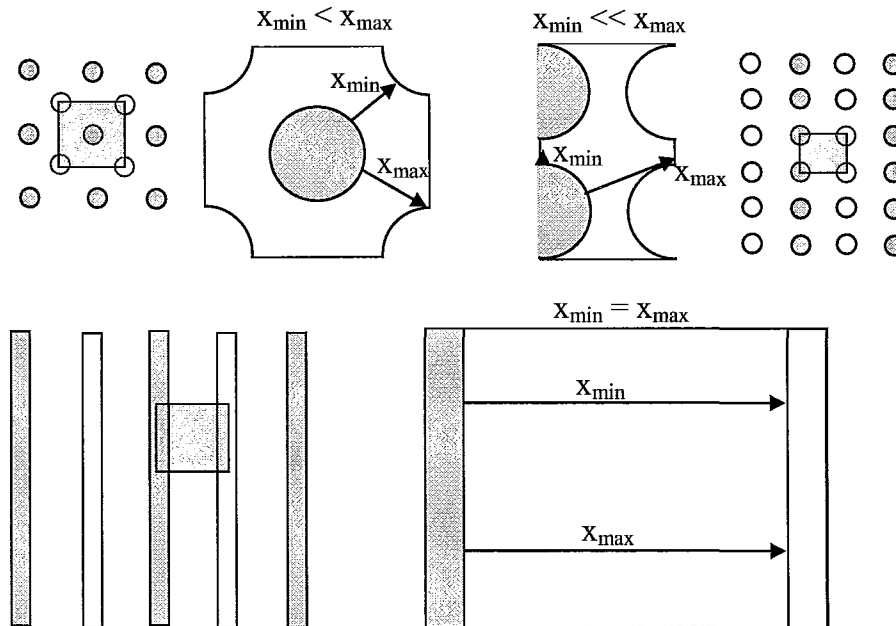


Figure 3.1: Non-uniform melt distances for round tube banks (staggered and aligned, white for capture tubes, grey for recovery tubes) versus uniform melt distance for rectangular channels.

3.3 – Analytical Model Single Storage Cell Time

The required time to fully charge a single thermal storage cell is dependent on the achievable heat flux into or out of the cell from the capture or recovery fluid. This heat flux is limited by the capture/recovery fluid flow, temperature and properties along with the thermal resistance of the cell. As the melt/solidification front propagates through the cell, this resistance will change. In the analytical model a pseudo-steady heat transfer assumption is used with time discretization to approximate the resistance at each melt fraction. Natural convection within the phase change material is neglected in the analytical model, as it is highly dependent on the detailed geometry and orientation of the cell, which are not specified in the preliminary design phase where this model is to be

used. This is a conservative assumption, as natural convection would only shorten the melt time estimated by conduction alone, or allow a larger spacing for a given melt time. Once a range of reasonable geometries for typical phase change material thermal storage cells is determined, further investigation into convection effects and other enhancements can be pursued.

3.3.1 – Pseudo-Steady Heat Transfer Model

In order to estimate the temperatures and thermal resistance in the phase change material thermal battery at each melt fraction, a pseudo-steady heat transfer model is used. This assumes that there is no heat flux imparted to the various components along the heat transfer path to bring about the changing temperature profile, but rather it is all transferred through to the melt front. This results in linear temperature profiles in each of the conduction components of the thermal battery, including the liquid phase of the PCM. This assumption does introduce a certain amount of error, especially at the beginning of a capture or recovery cycle, as the larger sensible thermal energy change causes the temperature profile to be non-linear. The non-linearity is caused by only part of the heat flux being transmitted to the neighbouring region of the material since some of it must be used to raise the temperature of the material. In a real system the temperature gradient must therefore decrease along the heat transfer path at the same rate as the heat flux for a material with constant thermal conductivity and cross-sectional area according to equation 9, Fourier's Law.

$$q'' = k \frac{\partial T}{\partial x} \quad (9)$$

The assumption of constant heat flux up to the melt front at a given melt fraction also causes appreciable error in cases where there is a significantly non-linear temperature profile due to certain combinations of system parameters and properties. This error was evaluated with the help of the CFD model in section 3.5.

Using this pseudo-steady assumption, a heat transfer balance can be performed at each melt fraction in order to solve for each of the interface temperatures. Rather than using set time steps, which would require iterative calculation of the melt front location, the time-step size is determined by setting the change in location of the melt front as 5% of the total PCM thickness. The heat fluxes calculated at any of the interfaces is then used as the average heat flux during that time step. This heat flux, along with the energy required to melt 5% of the PCM is used to get an estimate of the time required to progress from one melt front position to the next. It is also assumed that the capture or recovery convective heat transfer coefficient is known at each time step. While it is possible to use a convective heat transfer coefficient that changes with time, it would be more common to encounter a capture or recovery system with a constant flow rate, creating a constant convective coefficient. In this way the heat flux and time to melt are approximated for each melt fraction.

3.3.2 – Changing Temperature Profile and Sensible Energy

The fact that the linear temperature profiles do change between consecutive time-steps is partially accounted for by determining the sensible heat difference between the two profiles and adding that amount of thermal energy at the average heat flux for the time step in question. This allows for a more accurate energy balance, but still neglects

the effect of the slightly non-linear temperature profile caused by the sensible storage. This, in addition to the pseudo-steady heat flux balance, is used to determine a more accurate time required to melt a given amount of the PCM. Iteratively using this model with different geometries allows the determination of the PCM thickness required for a desired storage cell time.

3.3.3 – Equations Used in the Analytical Model

The one-dimensional pseudo-steady analytical model is composed of equations 10 through 13. These equations are solved for each melt fraction. The values of temperature at zero melt fraction are set to the initial temperature and the value of heat flux is set to zero. The temperature profiles at each subsequent melt fraction are based on the pseudo-steady heat flux balance of equation 10, assuming that immediately after time zero the capture or recovery flow is fully developed at the given bulk temperature and flow rate. The heat flux imparted to the melt front is therefore any of the three terms in equation 10. Equation 11 uses the first term, the convective heat transfer, to calculate the heat flux through the pseudo-steady system. The melted mass is then calculated by multiplying the melt fraction by the total PCM thickness, cross-sectional area and density as in equation 12. Equation 13 is used to calculate the time required to achieve the desired melt fraction by adding the previous time to the additional mass melted, multiplied by the latent heat of fusion and divided by the heat flux at the present melt fraction.

$$h_c(T_c - T_{tubd}(\gamma_n)) = k_{ss} \frac{(T_{tubd}(\gamma_n) - T_{tubel}(\gamma_n))}{l_{ss}} = k_{PCM1} \frac{(T_{tubel}(\gamma_n) - T_m)}{x_m(\gamma_n)} \quad (10)$$

$$Q(\gamma_n) = k_{PCM1} A_{cs} \frac{(T_{tube2}(\gamma_n) - T_m)}{x_m(\gamma_n)} \quad (11)$$

$$m_{melt}(\gamma_n) = \gamma \cdot l_{PCM} \cdot A_{cs} \cdot \rho_{PCM} \quad (12)$$

$$t_n = t_{n-1} + \frac{[m_{melt}(\gamma_n) - m_{melt}(\gamma_{n-1})] h_{slPCM}}{Q(\gamma_n)} \quad (13)$$

The size of melt fraction increments chosen can affect the solution and a melt fraction independence study was therefore performed. It was found that increments of 5% melt fraction produce final melt time results within 0.01% of the same model using 2.5% melt fraction increments. Increments of 10% showed results within 0.13% of the 2.5% increments, and 20% within 1.14% but only produce small number of temperature data points, therefore 5% melt fraction increments have been used.

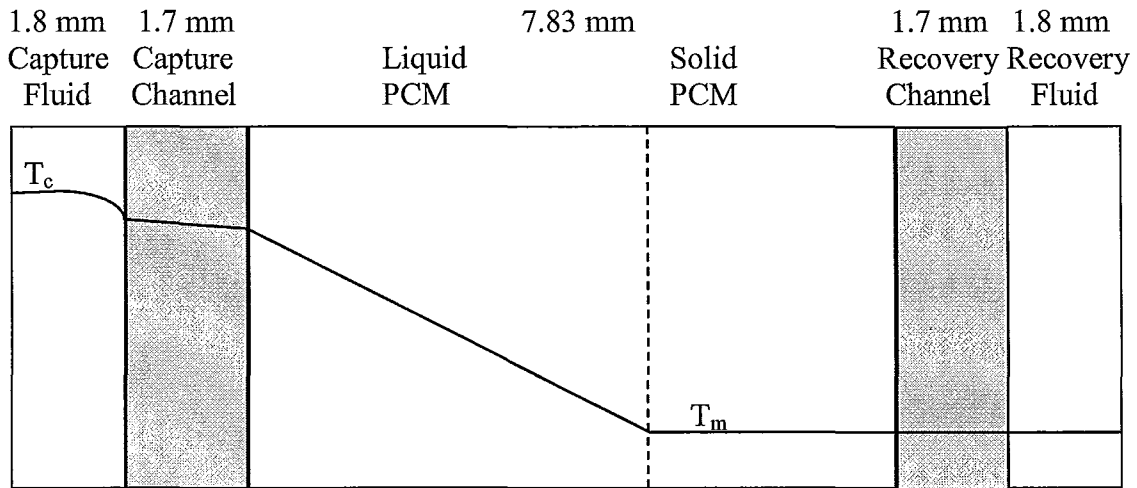
3.4 – Fluent Melting/Solidification Model

Numerical studies using the commercial software ANSYS-Fluent version 6.3.26 were used in this investigation. The transient studies were done using conduction only in the phase change material using the melting/solidification model by turning the solution of the flow and turbulence equations off, preserving only the solution of the energy equations. The melting/solidification model is designed to be used for two-phase flows and involves density and viscosity calculations in a “mushy zone”. This mushy zone is partially liquid and partially solid and its properties are determined using a lever rule based on the difference between the melting and freezing temperatures. The lever rule

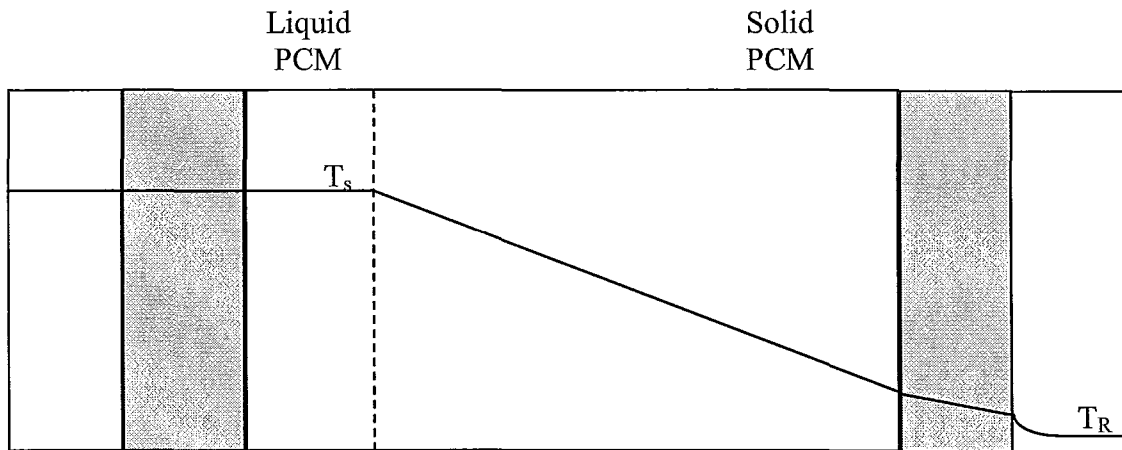
calculates the density, viscosity and heat capacity of the mushy zone based on a proportionally weighted average of the liquid and solid properties. Despite the fact that these calculated “mushy zone” properties are not used in a conduction-only solution, problems can arise in the model if the melting and freezing temperatures are set too close together. These problems can manifest as convergence issues or cause a discrepancy in the energy balance equations and are characterized by the integral of the heat flux not being equal to the change in stored energy of the system. For this reason, a check on the sum of the heat flux versus the enthalpy increase from the initial to final time step is necessary each time the melting/solidification model is used.

3.5 – Two-Dimensional Numerical Storage Cell Model

In order to test assumptions and help develop the mathematical model for the PCM thermal battery, a two-dimensional CFD model was created. This model, seen in figure 3.2, consisted of four layers: the capture channel wall, phase change material, recovery channel wall and recovery fluid. The boundary conditions for the base case were set to convective heat transfer on the capture channel wall and adiabatic walls for the other outer boundaries of the domain. An adiabatic condition was used for the edge of the recovery fluid domain because this represents only one-half of the fluid width and can therefore be considered as the centerline for one periodic repeating unit with no heat flux across this plane. Appropriate material properties were set up for the four regions and can be seen in table 3.1.



(a) Capture process (melting)



(b) Recovery process (solidification)

Figure 3.2: Two-dimensional CFD model geometry with temperature profiles for 50% liquid fraction during capture (a) and recovery (b).

Table 3.1: Material properties for the two-dimensional CFD base case.

Property	Units	Stainless Steel	Lauric Acid	Aluminum	Air
Density	[kg/m ³]	8000	869	2719	1.235
Heat Capacity	[J/kgK]	500	2150	871	1006.43
Thermal Conductivity	[W/mK]	16.4	0.17	202.4	0.0242
Kinematic Viscosity	[kg/ms]	N/A	0.0073	N/A	1.7894x10 ⁻⁵
Latent Heat of Fusion	[J/kg]	N/A	182,800	N/A	0
Melt Temperature	[K]	N/A	317.15	N/A	0
Freezing Temperature	[K]	N/A	316.15	N/A	0

Meshing and solving of the two-dimensional CFD models was done using ANSYS-Fluent and Gambit. The energy and melting/solidification models were used for these simulations. Solution of the flow and turbulence equations was turned off again for these cases, as only the solution of pure conduction in the liquid phase was desired. The simulated convective boundary condition at the capture channel wall does not require a flow solution due to the assumed constant convective heat transfer coefficient boundary condition previously discussed in section 3.3.1. Second order energy equations were used in the unsteady solver with the initial condition set at the uniform starting temperature.

A grid independence study was first performed to determine the required grid size for the CFD models. It was found that both the coarse and fine rectangular grids produced the same time to 100% melt, but there were slight differences in the heat flux profiles. Discontinuities in the heat flux versus time results were seen at intervals during the unsteady solution for both cases (2880 and 9216 elements), as seen in figure 3.3. It was hypothesized that these discontinuities were being caused by the melt front progressing parallel to the mesh divisions. This causes all of the cells in one row to achieve 100% melt and suddenly be permitted a temperature gradient simultaneously. In order to investigate this effect on the melt time, two triangular meshes were built. It was again seen that both of these meshes produced the same time to 100% melt as the rectangular cases, and produced the same heat flux at 10% melt, but did not show as pronounced irregularities in the heat flux versus time curve. Some irregularities are still seen, however, as the first few rows of cells are simply rectangular cells that have been

cut in half and the root problem therefore still exists at some melt front locations. With a paved triangular mesh in a rectangular geometry it is very difficult to avoid cells that closely approximate a hexahedral mesh without artificially skewing the geometry, which would also cause problems. The results for the triangular meshes are also shown in figure 3.3. Although the heat flux curves were smoother, the tetrahedral meshes produced unrealistic non-planar melt fronts since the line of 100% melt was forced to follow the contours of the cells. In light of these results, the coarser of the two triangular meshes (5956 cells) was chosen for the two-dimensional CFD studies in order to get heat flux data over time that makes more physical sense, but it was also noted that a rectangular mesh would produce acceptable final results and allow for the possibility of a planar melt front.

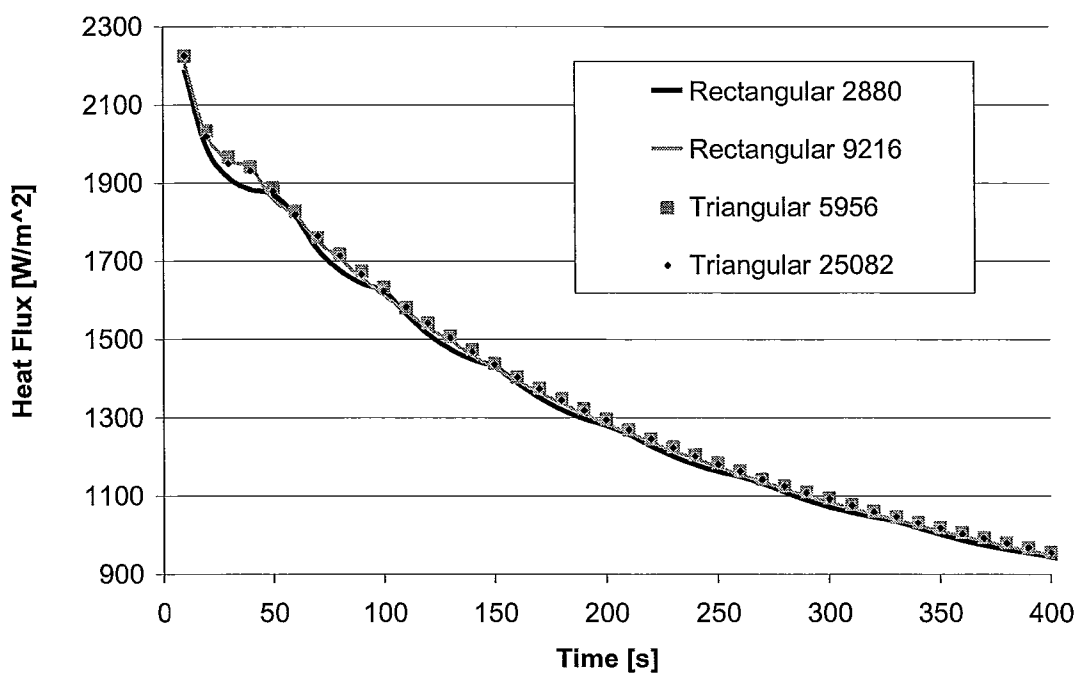


Figure 3.3: Heat flux versus time curves 0-400 s for the rectangular and triangular meshes.

A time-step study was also performed for the base case in order to determine the maximum time-step size that could be used in the unsteady simulations. It was originally hypothesized that because the only equations being solved were the energy balance and conductive heat transfer, the time-step used could be very large without significantly affecting the time to 100% melt. This was verified by using time-steps of 1, 10 and 100 seconds. It was shown that, with the exception of the accuracy due to the time-step increment, the 1, 10 and 100 second time-step cases produced the same time to full melt (2152, 2160 and 2200 seconds respectively). The heat flux at 10% melt fraction was also within 0.1% for the 1 and 10 second cases (1474 and 1475 W/m² respectively). It was therefore decided that a time-step size of 10 seconds would be used for the two-dimensional simulations in order to get good resolution in the output data without increasing the computational time unnecessarily. Along with this time-step size decision, a maximum energy residual is also required for the iterative solution of each time-step to optimize computational time. Based on the extremely small changes in heat flux and melt fraction values in the grid independence study for residuals below 10⁻⁸, seen in figure 3.4, it was decided to use 10⁻⁸ as the maximum energy residual value for the two-dimensional time-step convergence.

The base case for all of the two-dimensional CFD work therefore has the parameters, Fluent set up and model boundaries described in Appendix D. All deviations from the input parameters are outlined in the individual sections of the parametric studies. The base case time for the CFD model was 2160 s, while the analytical model base case time was 2219 s and the Stephan-Neumann base case full melt

time was 1307 s. As predicted, the Stephan-Neumann model predicts a shorter time to melt than the CFD and analytical models. The parametric study was based on the change in the CFD and analytical base case full melt times and is therefore expressed as a percentage change in the base case melt time.

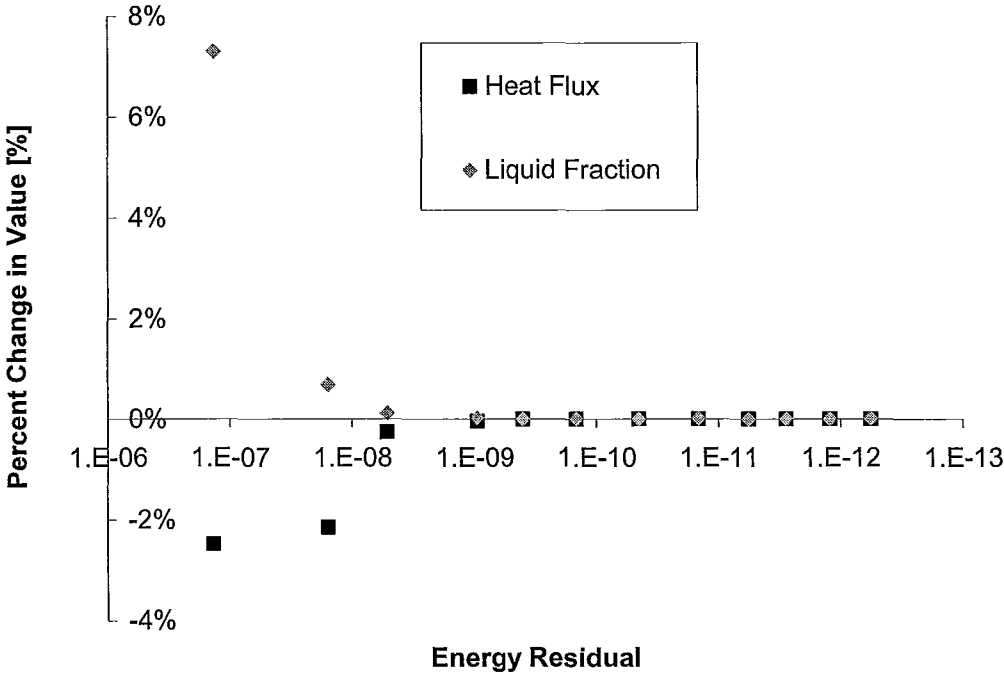


Figure 3.4: Change in heat flux and melt fraction vs. energy residual during a single time-step.

3.5.1 – Effect of Thermal Conductivity

Four different thermal conductivities are involved in each of the two-dimensional four layer models that have been studied: 1) that of the capture channel, PCM, recovery channel and recovery fluid for the capture cycle and 2) that of the recovery channel, PCM, capture channel and capture fluid for the recovery cycle. Using the Fluent melting

and solidification model, it is not possible to specify different thermal conductivities for the two phases, so these were constrained to be equal in the CFD simulations. The analytical model is simplified such that changing the thermal conductivity of the solid PCM region, the recovery channel and recovery fluid have no effect on the melt cycle and changing the thermal conductivity of the capture channel and capture fluid have no effect on the freezing cycle. This simplification is assessed by looking at the changes in the CFD model under these conditions. Changing the recovery fluid thermal conductivity by -60% to +400,000% (0.01 – 1000 W/mK) showed no change in the time to full melt, while changing the recovery channel thermal conductivity by +400% (1000 W/mK) showed a slight increase in time to full melt, as seen in figure 3.5.

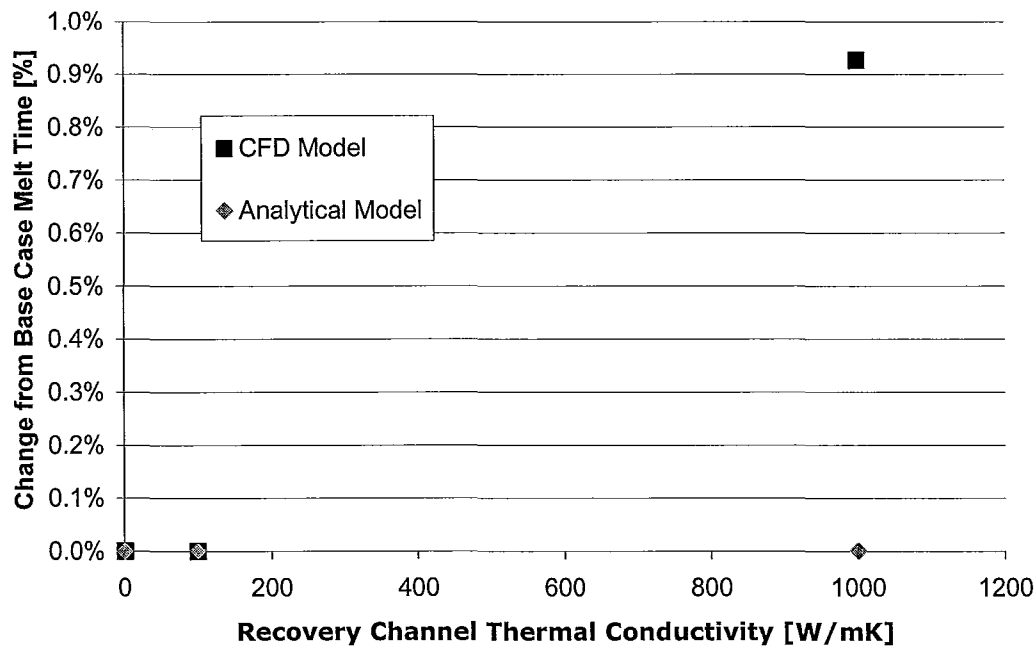


Figure 3.5: Effect of changing recovery channel thermal conductivity from 0.01 to 1000 W/mK during melt cycle.

Changing the capture channel thermal conductivity during the melt cycle, however, does have an effect in the analytical model, as this parameter is used to calculate the pseudo-steady thermal resistance of the cell. The effect of changing the capture channel thermal conductivity in both the analytical and CFD models by -90% +6000% (1 - 1000 W/mK) can be seen in figure 3.6. For changes between 500% and 6000% the CFD model showed poor convergence behaviour during the first four iterations and therefore produced unrealistic results due to exceptionally high heat fluxes during this period. The two data points in this range are therefore omitted from the graph, but the two models agree quite well for the other two data points. A second mesh was solved for the capture channel sensitivity study, but poor convergence in the first three iterations was still seen. Further attempt to improve convergence behaviour for the higher channel thermal conductivities was not successful, and the model limits will therefore be based on only the tested values (up to 202 W/mK).

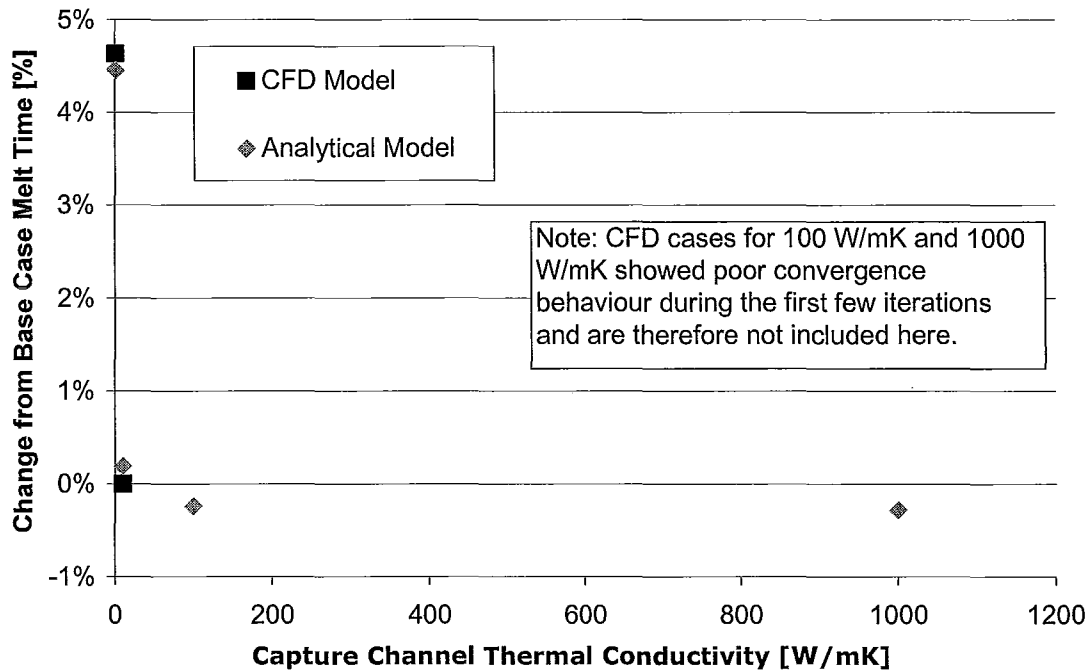


Figure 3.6: Effect of changing capture channel thermal conductivity from 1 to 1000 W/mK during melt cycle.

The effective thermal conductivity of the PCM is an important parameter in the determination of cell storage time for the thermal battery. This is referred to as “effective” thermal conductivity as it can include enhancements such as forced or natural convection, conductive fins, foams and fibres, nanotubes, particles or other additives. All of these would modify the “effective” thermal conductivity of the PCM used in the model. While research has been done on improving effective thermal conductivity of phase change materials, it usually involves an increase in the volume required to house the enhanced material (Mills et al., 2006). As this volume increase can have a detrimental effect on overall system size and cost, more research should be done into the cumulative effect of additives on thermal battery system design.

In order to ensure that a change in the effective thermal conductivity of the PCM produces realistic results in the analytical model, these changes are compared to the same change in the CFD model. Figure 3.7 shows the percentage difference in total melt time for three different effective PCM thermal conductivities that extend beyond the expected range for low melt temperature PCM enhancements found in Zalba et al. (2003). The two models show very good agreement in the effect of changing effective PCM thermal conductivity. The comparative sensitivity studies for the various thermal conductivities used in both the CFD and analytical models therefore show good agreement, which lends confidence to the simplifications made in the analytical model.

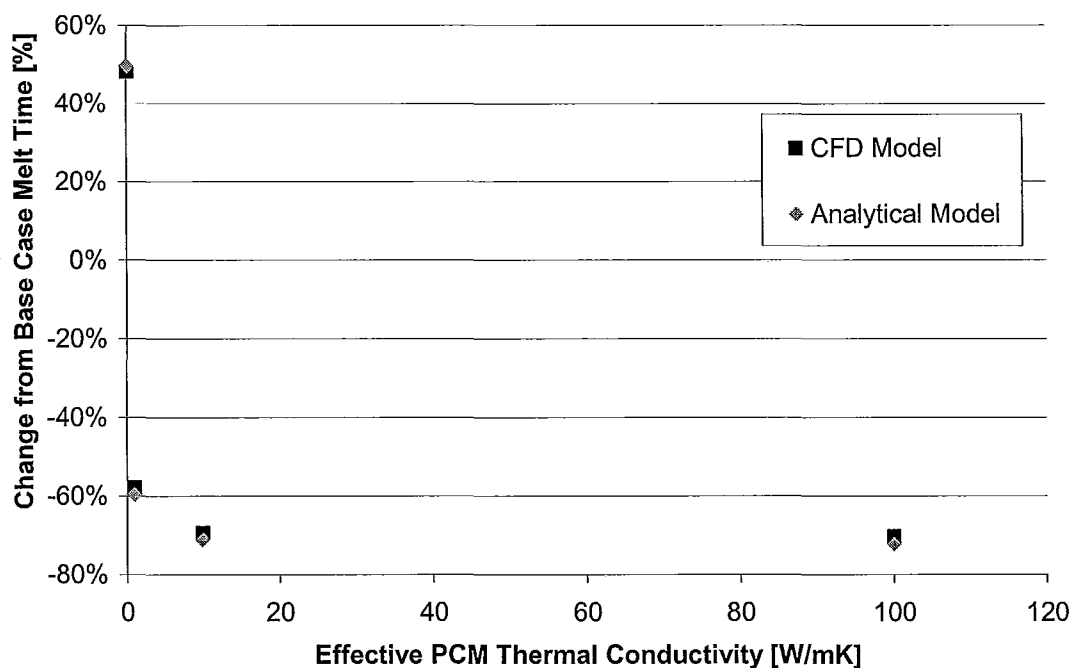


Figure 3.7: Effect of changing effective PCM thermal conductivity from 0.1 to 100 W/mK.

The result of changing the effective thermal conductivity of the PCM is greatest for values under 10 W/mK, with only a 1.5% difference in the total melt time between 10 W/mK and 100 W/mK. If improvements in effective thermal conductivity are to be made, this sensitivity study should be performed for the geometry and materials in question. For the base case geometry and properties studied here, increases up to 10 W/mK should be targeted. Care should be taken, however, to ensure that the additional volume occupied by the additives does not overbalance the decrease in PCM thickness for a given cell charge time. The figure of merit that should be used to determine the effect of conductivity enhancing additives is the total material cost for a given cell charge time.

3.5.2 – Effect of Latent Heat of Fusion

The latent heat of fusion is also an important parameter in the determination of thermal storage cell charge and recovery time. The effect of adjusting this parameter by -50% to +20% is seen in figure 3.8. Both the CFD and analytical models show similar responses to the change in latent heat of fusion of the PCM. This result also instils confidence in the analytical model.

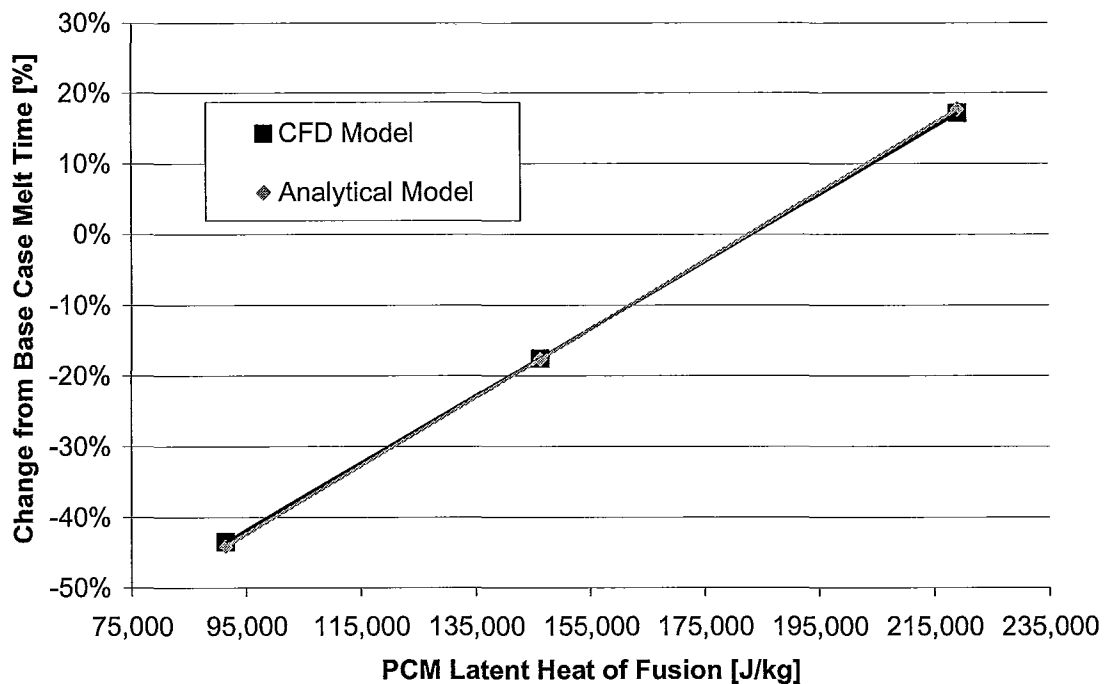


Figure 3.8: Effect of changing PCM latent heat of fusion from 91,400 to 219,360 J/kg.

3.5.3 – Effect of Sensible Energy Storage

Another important parameter in the determination of capture/recovery cycle time is the difference between the initial temperature and melt/freezing temperature. This parameter is of particular interest as the inclusion of only PCM sensible heat in the analytical model is assessed. Figure 3.9 shows the effect of changing the initial temperature from 1.05 K to 20 K below the melt temperature. Smaller differences were not possible in the CFD model due to the computational requirement of having a 1 K difference between the melting and freezing temperatures in the CFD melting/solidification model. The trends for both the CFD and analytical models are similar for a change in initial temperature difference, but the slopes are somewhat

different. As the amount of temperature difference increased, the disparity between the CFD and analytical models increased, with the analytical model under-predicting the time to full melt in the CFD model. This was as expected, due to the lack of consideration of the thermal mass of the components other than the PCM in the analytical model. This error was deemed to be acceptable for small degrees of initial temperature difference, but should be further investigated in systems that utilize sensible thermal energy storage as well as latent thermal energy storage.

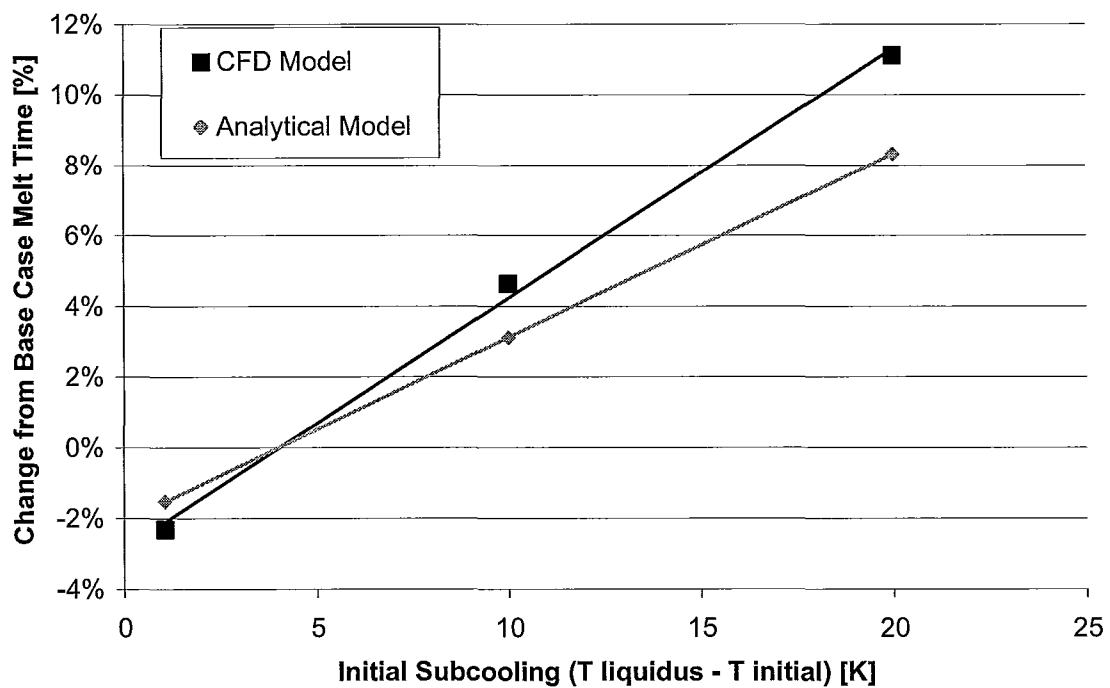


Figure 3.9: Effect of changing difference between initial and melt temperatures (1.05 to 20 °C).

3.5.4 – Effect of Capture/Recovery Temperature Difference

Since the driver for heat flux within the thermal battery is the temperature difference between the PCM melting or freezing temperature and the temperature of the capture/recovery fluid, this difference is also a very important parameter to study. Figure 3.10 shows the effect of changing the capture fluid temperature difference from 2 K to 50 K. For differences of 10 K or above the agreement between the two models was quite good. Lower temperature differences, however, produced a significant disparity between the full melt time predicted by the CFD and the analytical models. This was due to the increasing non-linearity in the temperature profiles caused by the lower heat flux into the cell, as seen in figure 3.11 compared to figure 3.12 which shows the base case (21 K temperature difference). This will be a limitation of the analytical model that must be clearly defined for users in order to prevent large sizing errors in situations with very small temperature differences between the PCM melting/freezing and recovery/capture temperatures. This will also be a source of error in the analytical model due to the assumption that the entire cell is transferring heat between the average bulk fluid temperature and the average cell wall temperature. For fluids with a significant residence time in the flow channel and therefore a large temperature drop in the flow direction, the error in under-predicting the capture temperature upstream of the average will not necessarily balance the error in over-predicting the capture temperature in the latter portion of the channel.

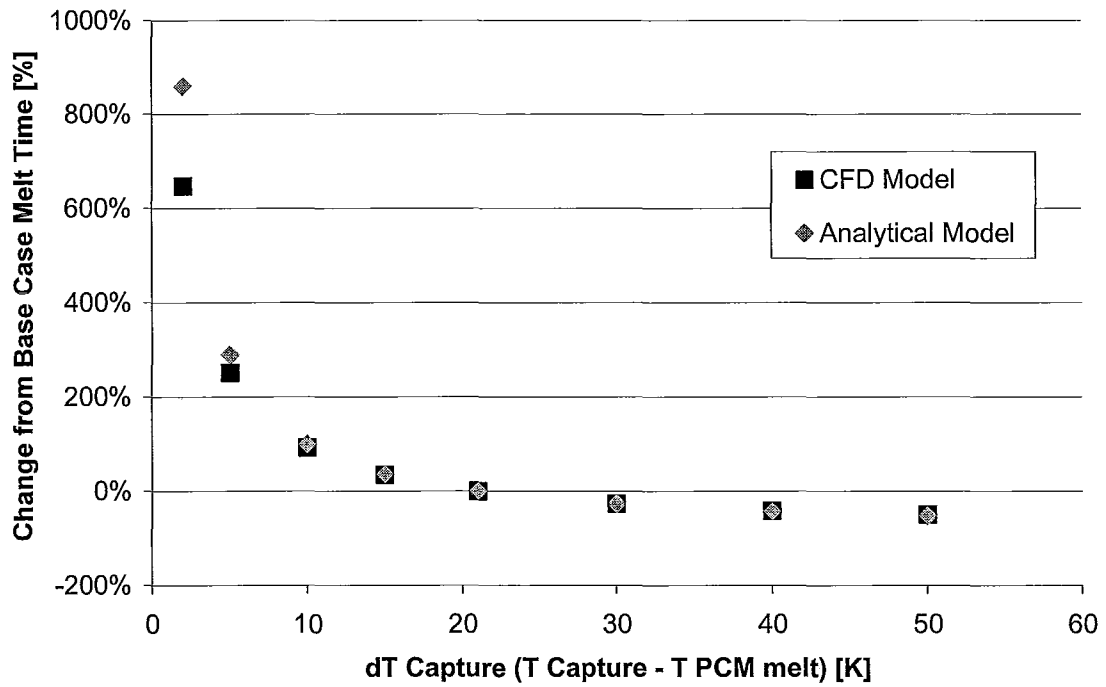


Figure 3.10: Effect of changing the capture fluid temperature difference (2 to 50 °C).

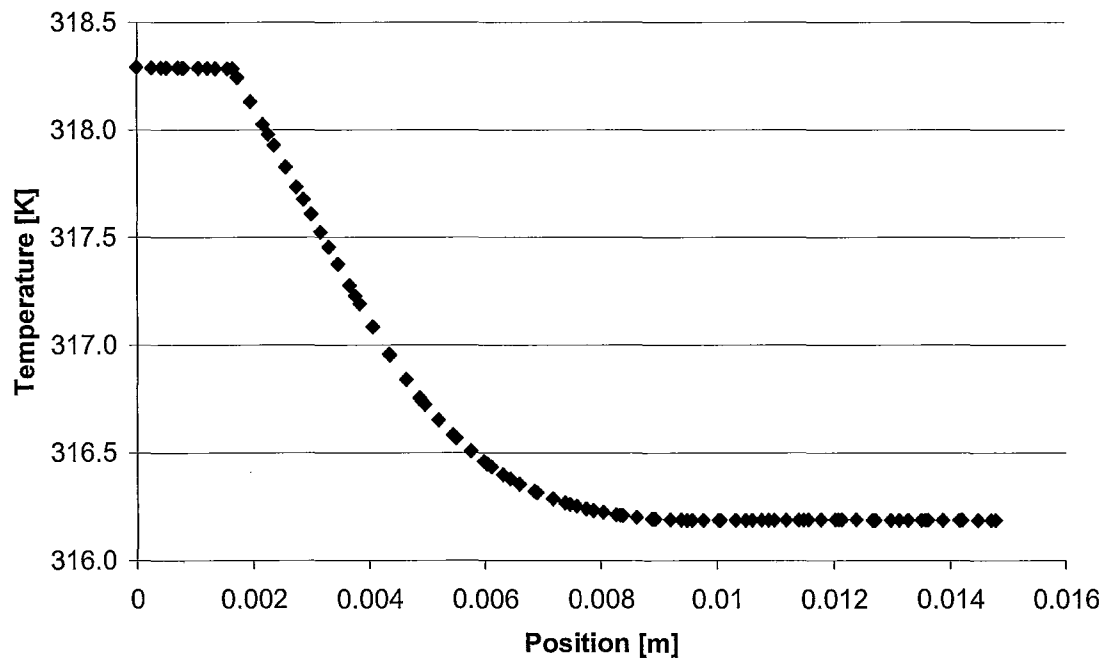


Figure 3.11: CFD temperature profile at 50% melt for a dT Capture of 2K.

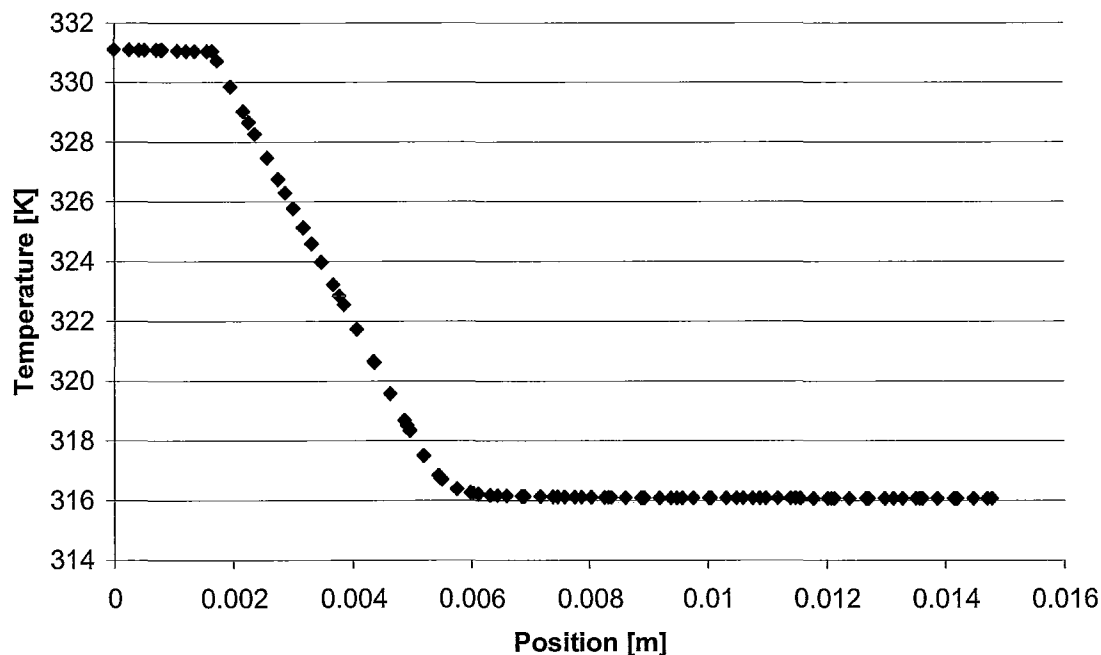


Figure 3.12: CFD base case temperature profile at 50% melt for a dT Capture of 21K.

3.5.5 – Effect of Dimensional Changes

The effect of changing the cell dimensions was investigated by producing several more meshes with the same boundary conditions as the base case, but different thicknesses for each of the four materials. The first geometries investigated were doubling or halving the PCM thickness. The time to melt the same thickness of PCM, 0.016 m, was compared. The base case and doubled thickness were found to have the same melt time, but the halved case took 3% longer than the base case. This supports the analytical model assumption that the geometry past the melt front has very little effect on the melt time.

This hypothesis was further investigated by testing a fourfold increase in the thicknesses of the recovery channel and recovery fluid. This geometric change resulted

in a 4% decrease in the time to half melt but only a 2% decrease in final melt time over the base case final melt time. These small changes for large geometry changes in the region beyond the phase change material further support the model assumption that nearly all of the heat flux is absorbed in the phase change front.

The final geometric parameter to be analyzed in the conduction-only model was the thickness of the capture channel. This was increased by twofold from the base case and resulted in a 1% increase in the time to both 50% and 100% melt over the base case.

The very small changes in melt time resulting from geometric changes in the capture and recovery channels show that any error in estimating the size and thickness of these portions of the phase change thermal energy storage cell will not have a significant effect on the sizing of the system. This is an important finding, as it further supports the use of the analytical model for initial thermal battery assessment without knowledge of the detailed design.

3.5.6 – Effect of Capture/Recovery Convective Heat Transfer Coefficient

Since this study focuses on laminar flow through the capture/recovery channel, the convective heat transfer coefficient does not change with flow rate in this range. The analytical model, however, was compared to CFD results for convective heat transfer coefficients of 10 to 10,000 W/m²K in order to ensure that the sensitivity showed the proper trends. Figure 3.13 shows this comparison with good agreement between the two models. It also shows almost no advantage to increasing the heat transfer coefficient above 1000 W/m²K for the analyzed geometry and properties.

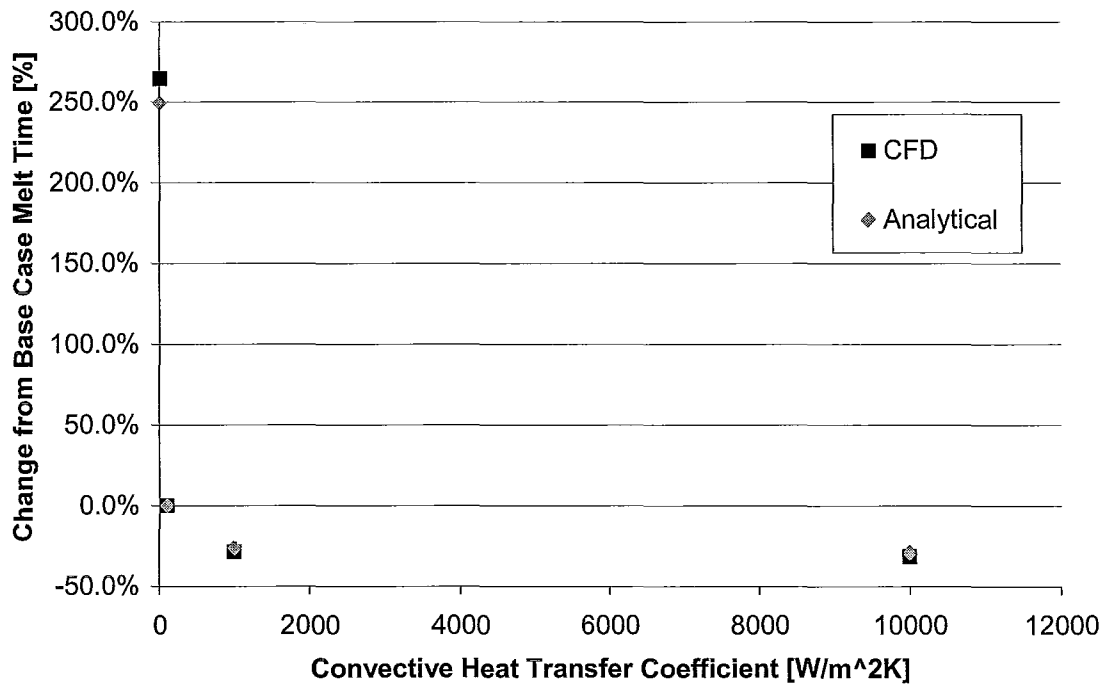


Figure 3.13: Effect of changing the capture fluid convective heat transfer coefficient from 10 to 10,000 W/m²K.

3.6 – Three-Dimensional Sample Cell Model

Because the melt time for the thermal battery is dependent mainly on the properties of the phase change material and its thickness, validation of the model should be done using various materials and thicknesses. This causes some difficulty, as most feasible phase change materials with similar melt temperatures also have very similar latent heat of fusion and thermal conductivity. It would therefore be quite beneficial to have a reliable numerical model with which to test the analytical model in order to reduce the time, cost and complexity involved in experimenting with a wide range of possible phase change materials. A three-dimensional CFD model was therefore created that had the same geometry as the experimental test cell discussed in Chapter 4. This allowed validation of the CFD model against a limited number of experimental results in order to

increase confidence in using CFD to investigate the effects of material properties and geometry changes.

3.6.1 – Lauric Acid Storage Cell

A model of the experimental set up using lauric acid as the phase change material was created to compare the results of the testing with those of the CFD model. Some simplifications were made to facilitate geometry creation and meshing of the CFD model. Sensor geometries were not included after it was discovered that this increased the mesh size well above the hardware capabilities. It was initially unknown if the presence of a baffle would significantly change the results of the CFD model, and a simplified geometry was therefore modeled to determine whether or not it should be included. Based on the results of this simple rectangular prism geometry of similar dimensions to the test cell modeled with and without a 2 mm thick baffle, it was seen that the baffle only changed the final melt time by 0.1%. For this reason the test cell geometry modeled in the 3D CFD simulations did not contain a baffle.

Due to the occurrence of sliver elements caused by any profiles coming together with a mating part with square corners, as seen in figure 3.14 all geometries were approximated as having square corners rather than filleted ones. Fittings and hoses were not included in the 3D CFD model. Instead, 50 mm inlet and outlet tubes were added above the top of the flow channel to capture the turning of the fluid in these regions. These simplifications resulted in the geometry seen in figure 3.15.

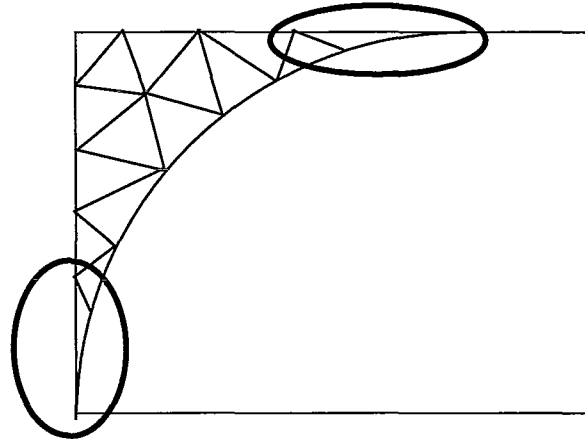


Figure 3.14: Sliver elements at junction of rounded and non-rounded parts.

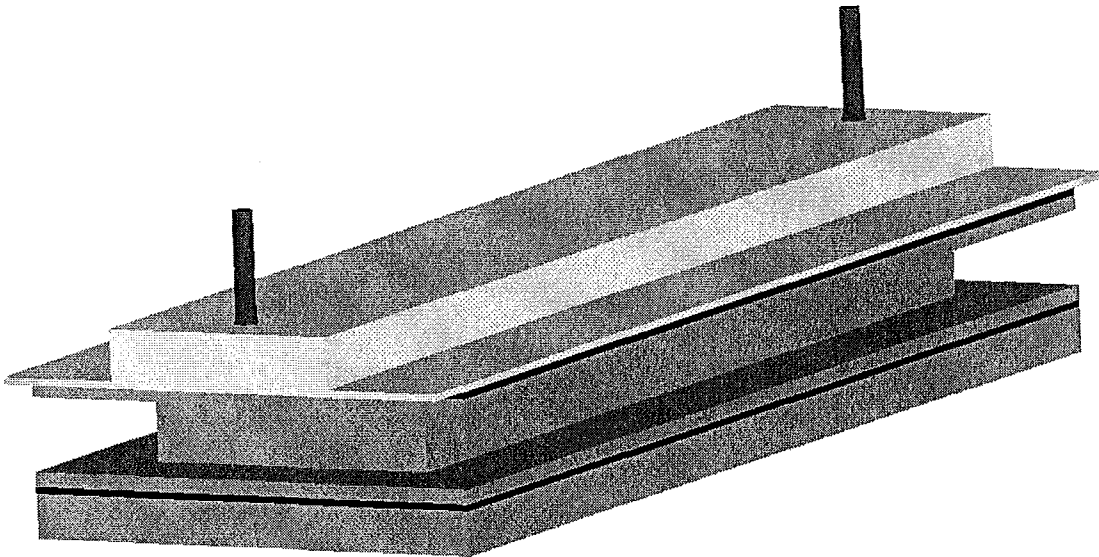


Figure 3.15: Lauric Acid storage cell CFD model geometry.

Based on the two-dimensional grid independence study and the difficulties associated with tetrahedral meshing in multiple files with subsequent merging, a hexahedral mesh was chosen for the three-dimensional test cell geometry. The cell size was based on the results of a three-dimensional rectangular prism grid independence study of the PCM region, seen in table 3.2. It was determined from this study that a hexahedral mesh of 1.18 million elements would be sufficient for the phase change material chamber. This resulted in a total mesh size of 6.4 million elements, of which cross-sections can be seen in figures 3.16 and 3.17.

Table 3.2: Grid independence results for three-dimensional CFD PCM chamber.

	Cells	Melt Time	Cells	Melt Time	Cells	Melt Time	Cells	Melt Time
Hexahedral	1710	63180	16302	63150	141726	68400	1180734	69610
Tetrahedral	146827	61280	474789	65290	997025	67150	2003170	68170

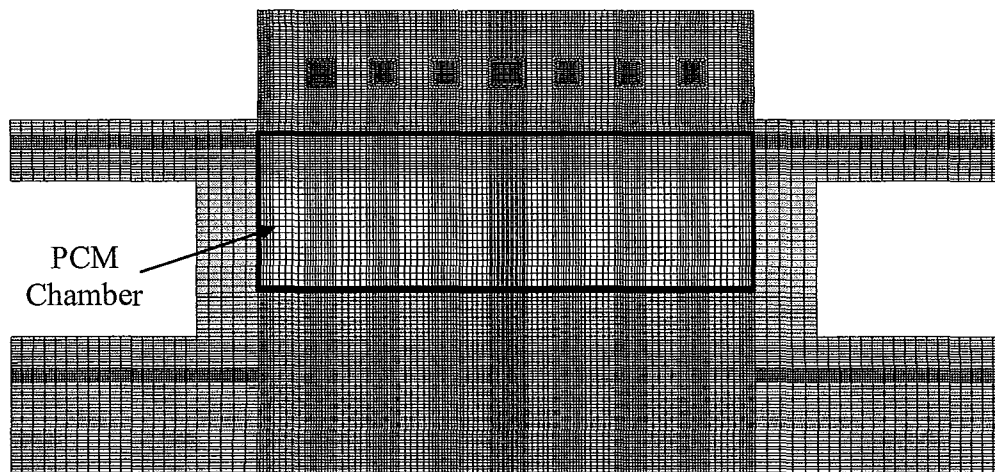


Figure 3.16: Lauric Acid storage cell CFD mesh transverse cross-section.

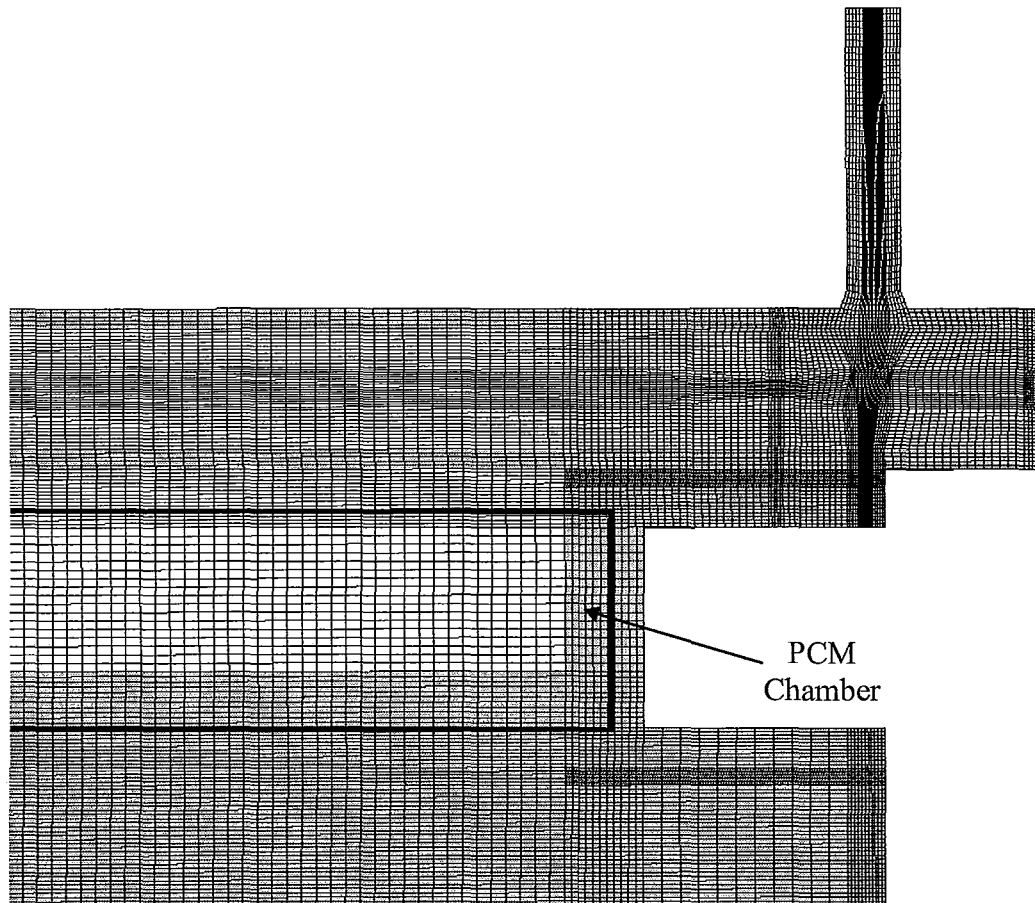


Figure 3.17: Lauric Acid storage cell CFD mesh lateral cross-section, inlet end.

The CFD model was run using the material properties and boundary conditions listed in Appendix D. First the flow in the capture/recovery channel was set to the initial temperature of the cell so that flow could be solved, keeping the entire cell at the correct temperature. The flow was solved using a k-epsilon turbulence model with enhanced wall treatment in order to have consistent model set up over the entire range of flow rates. A laminar model would have been unsuitable for higher flow rates as turbulent intensities of up to 13% were found in the inlet impingement zone when solving with the k-epsilon model. While some y-plus values were out of the desired range of 1-10 for the region

where the inlet flow impinges on the flow channel bottom, this region is not in contact with the phase change material chamber and refinement of the cells would have caused a large increase in the total number of cells in the model. However, based on the location of the cells, away from the main heat transfer zone, and the maximum y -plus of only 13, the small errors caused by these y -plus values were not expected to have a significant effect on the solution. Utilization of the k -epsilon turbulence model for predominantly laminar flow was verified for a flow rate of 0.00435 kg/s using a laminar model and the two solutions were found to be within 3.2% for both average and maximum velocity. The resulting time to full melt predicted by both models was 8.2 hours. An additional solution was also performed with a higher water flow rate of 0.0266 kg/s to match additional experimental conditions. The melt time predicted by this model was 8.0 hours. This slight decrease in melt time makes sense, as it would be expected that a higher flow rate would cause slightly higher local heat transfer coefficients, as the flow is not everywhere laminar and fully developed and therefore a slightly shorter time to full melt.

CHAPTER 4 – Test Facility

4.1 – Test Cell Design Criteria and Constraints

In order to ensure that the analytical and numerical models produced valid results, a test apparatus was designed to compare predicted melt and solidification times.

Constraints to ensure that the test apparatus would adequately test the predictions of both the analytical and numerical phase change material thermal storage models were:

- Able to measure the position and width of the melt front in the phase change material to within 10% of the full melt thickness (enough to check if there is a significant mushy zone but still a reasonable spacing for 1/16” thermocouples)
- Able to simultaneously record temperature, heat flux and flow data at an adequate rate to capture the transient behaviour of the melting and solidification processes (minimum 1 sample set per 10 seconds in order to obtain enough data to capture the transient behaviour)
- Insulated such that the thermal losses are either reduced to <10% of the total heat transfer or are known to within <10% of the total heat transfer (to more closely approximate a real system, which would need excellent insulation in order to prevent wasted thermal energy)
- Able to accommodate expansion and contraction of the PCM during the entire range of temperatures and states of the test matrix (different PCMs will have

different expansion coefficients, but the rig constraint is accommodation of up to 20% change in volume)

- Initial temperature of the cell controllable to within 1 °C to ensure a known initial condition and guarantee full melt or solidification
- Measurement capabilities for temperature profile within the PCM and capture/recovery flow rate
- Thermal energy source and sink temperature controllable to within 2 °C to keep the fluctuations in the capture or recovery fluid temperature to a minimum.

Criteria to make the test apparatus effective and easy to use included:

- Easy to assemble and clean
- Safe to handle during set up and operation
- Ease of adding and removing PCM
- Compact and light-weight
- Robust for use with different thermal energy sources and sinks and suitable for a wide range of operating temperatures
- Adjustable melt thicknesses
- Optically clear for visualization of melt front during some tests
- Large enough cross-section to evaluate one-dimensional assumptions, capable of operating in multiple orientations to test gravitational effects
- Flexible for the addition of conductivity or convection enhancement devices or materials

- Modular to accommodate reuse of some components for different test conditions and thermal cycling tests

The test cell designed using these criteria and constraints is shown schematically in figure 4.1, with detailed geometry and test procedures in Appendices A and B.

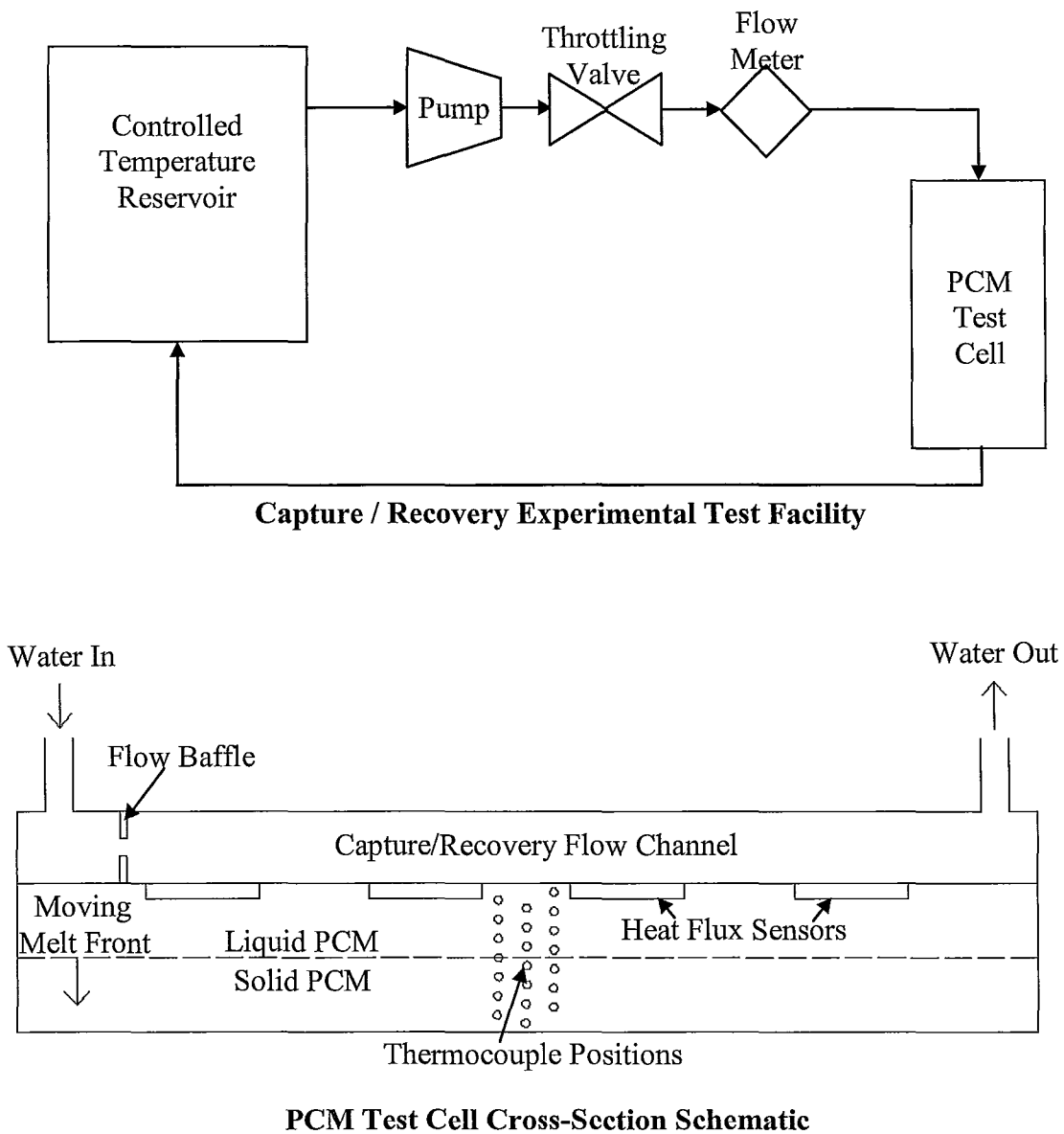


Figure 4.1: Schematic of the phase change material test cell.

4.2 – Phase Change Material Chamber

The melt time for a PCM thermal battery is dependent largely on the PCM properties and the melt thickness. This means that the thicker the PCM chamber is in the melt direction, the longer it will take the cell to reach 100% melt. The melt thickness chosen for the test apparatus was therefore a balance between reasonable melt time and enough space for several temperature measurement devices along the thickness. A flanged modular design for the PCM chamber was therefore used such that different thicknesses can be achieved by stacking several cells in series. The single cell thickness is 40 mm with room for 16 thermocouples placed in three columns. Since the investigation of gravitational effects is eventually desirable, the cell design is a rectangular cross-section with an aspect ratio of 4.5. This will allow evaluation of convective currents in the vertical orientation with two different geometries, one with the longer dimension aligned with gravity and one with the shorter dimension aligned with gravity. In order to have large enough dimensions to reasonably approximate one-dimensional heat transfer, the chamber width is 100 mm with a height of 460 mm. This gives a single cell volume of $1.77 \times 10^{-3} \text{ m}^3$ and a reasonable mass of PCM for handling, assuming the specific gravity of the phase change material is between 0.9 and 2.1, as in all the materials presented in tables 2.2 and 2.3. Despite the known volume of the PCM chamber, the mass of phase change material was verified using a scale with capacity of 5kg and precision of 1.0g (Starfrit, 2009). The test cells were made from clear

polycarbonate for potential visualization, but this was found to be unrealistic due to insulation requirements and the opacity of the solid phase change material. Holes were drilled in the short end of the PCM in order to fill the chamber with plugs to allow some leakage as the material melts and expands.

Attachment of the PCM chamber to the capture/recovery flow channel and backing plate was done using bolted flanges and gaskets. Additional test configurations are possible using more than one PCM chamber in series. The flanged design can be seen in figure 4.2 for the single PCM cell. Up to four of these parts can be attached in series, resulting in melt thicknesses of 40 mm, 80 mm, 120 mm and 160 mm. Additional adjustment of the melt thickness is possible by using a backing plate with a protrusion into the PCM cell cavity. Two backing plates, one flat and one with an 18 mm protrusion were fabricated giving additional melt thicknesses of 22 mm, 62 mm, 102 mm and 142 mm. Bolts were located, seven per side, at a spacing of 76 mm (3 in). No bolt holes were used along the shorter side of the rectangular PCM chamber in order to accommodate the capture and recovery module. Buna-N (Nitrile) gaskets at 3.2 mm (1/8 in) thickness and a layer of silicone caulking were used to seal between flanges.

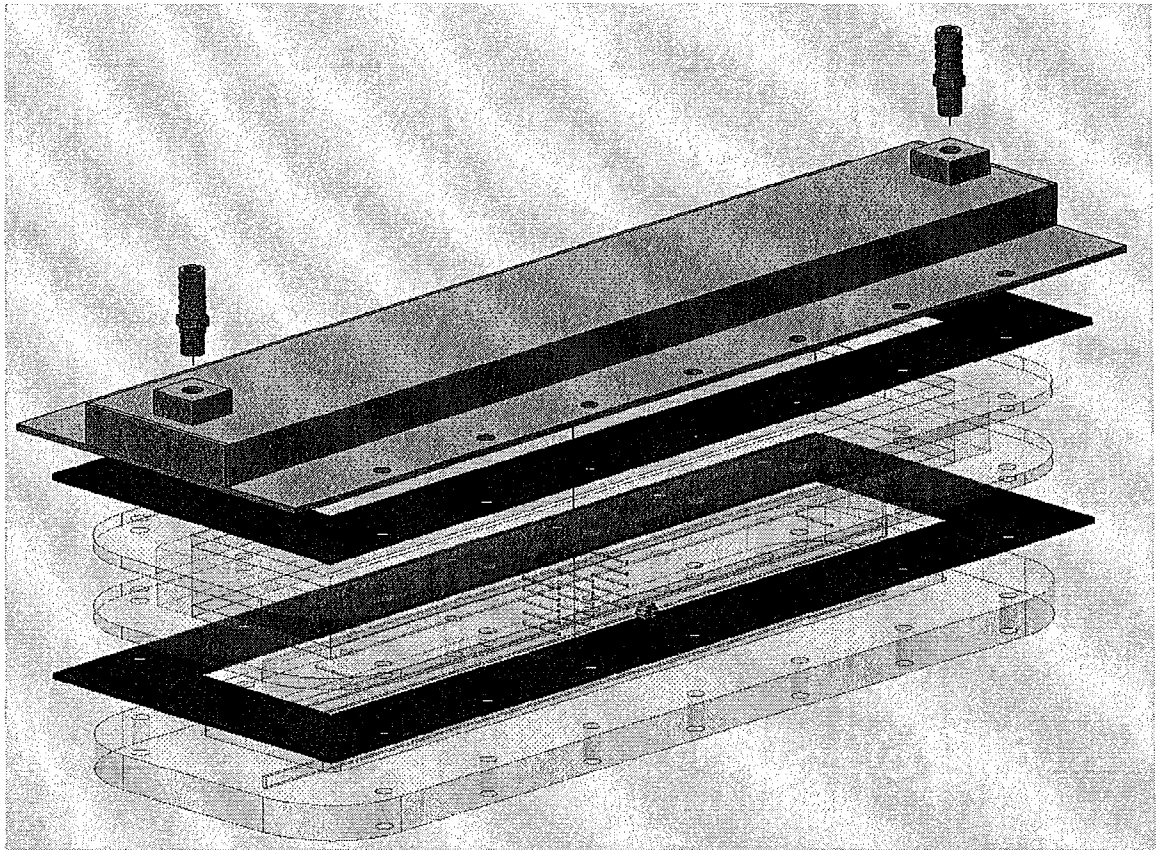


Figure 4.2: Flanged modular PCM chamber design.

To facilitate temperature measurements, a 2 mm thick 460 mm long polycarbonate baffle was placed along the centre line of the PCM chamber with a total of 18 1/16” holes to keep each of the temperature measurement devices in their intended location. A machined slot in the backing plate retains this baffle in place during assembly and testing. Additional baffles can be fabricated easily for the multi-cell configurations or different temperature measurement locations. The flat backing plate and baffle assembly can be seen in figure 4.3. Detailed drawings and specifications for all test components can be found in Appendix A.

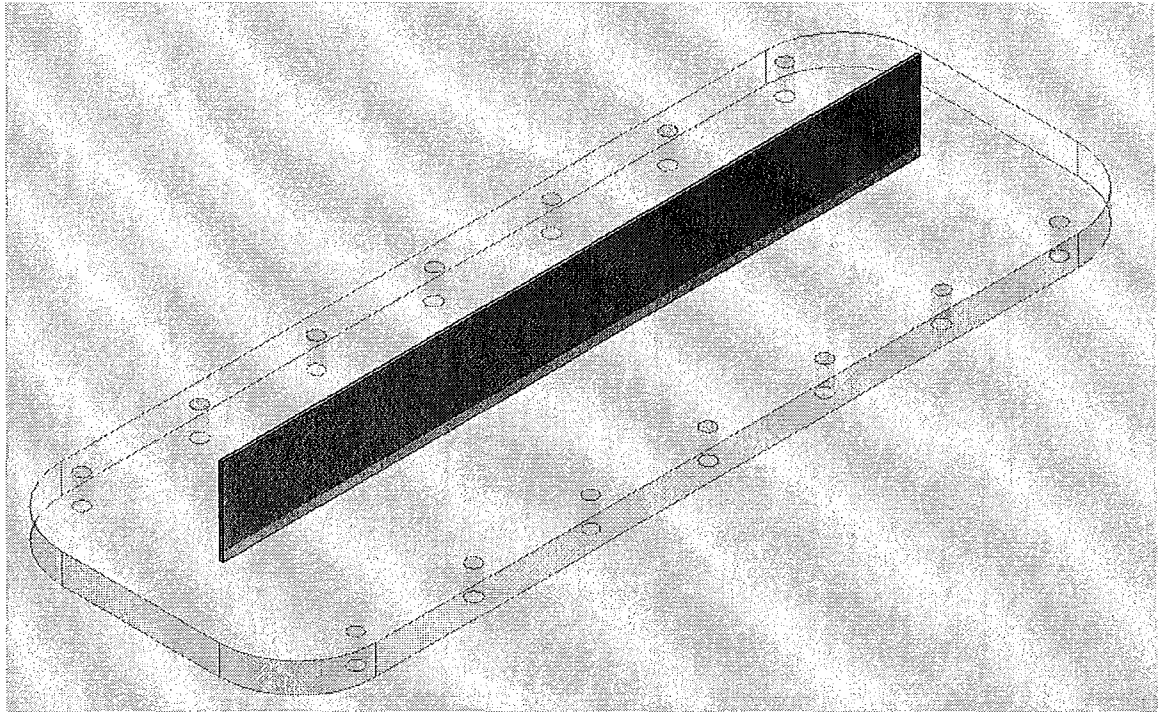


Figure 4.3: Flat backing plate with temperature measurement locator baffle.

4.3 – Capture/Recovery Fluid Channel

Since the thermal resistance of the phase change material alone is quite high, it was not necessary for the test apparatus to accommodate high flow rates, as the increase in convective heat transfer coefficient only has a small effect on the average heat flux into the PCM. This is demonstrated in the following calculations (equations 14 through 17) of the system thermal resistance up to the melt front corresponding to figure 4.4:

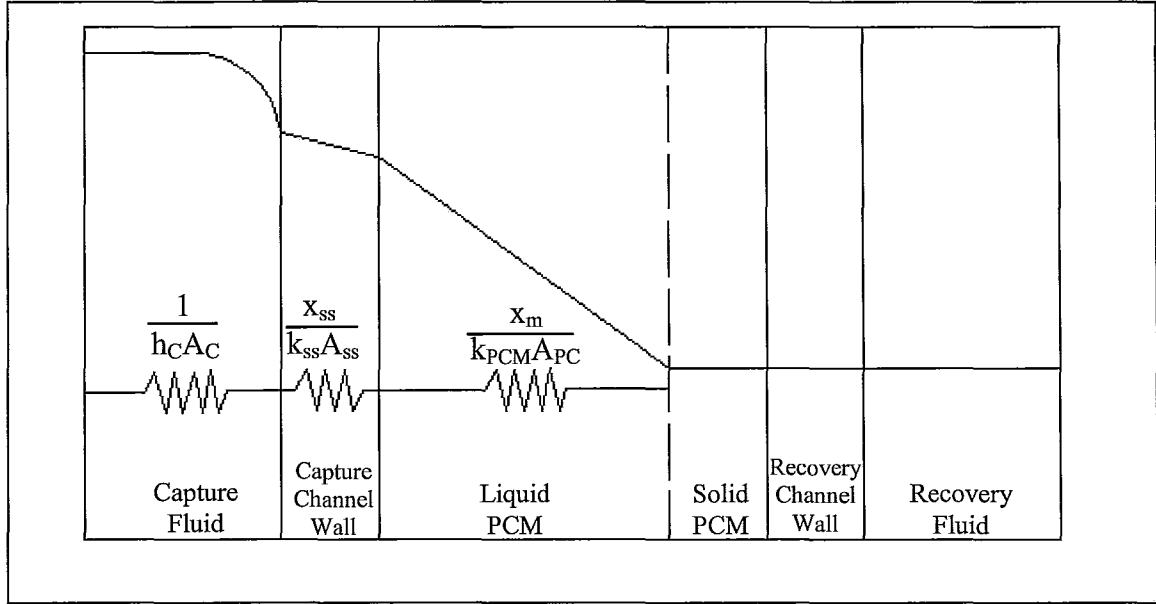


Figure 4.4: Electrical resistance analogy diagram for calculating the heat transfer resistance of a phase change material cell.

$$\frac{1}{UA} = \frac{1}{h_c A_c} + \frac{x_{ss}}{k_{ss} A_{ss}} + \frac{x_m}{k_{PCM} A_{PCM}} \quad (14)$$

$$A = A_c = A_{ss} = A_{PCM} \quad (15)$$

$$\frac{A}{UA} = \frac{1}{h_c} + \frac{x_{ss}}{k_{ss}} + \frac{x_m}{k_{PCM}} \quad (16)$$

$$x_{ss} = 0.0032\text{m} \quad x_m = 0 \rightarrow 0.04 \text{ m} \quad k_{ss} = 202.4 \text{ W/mK} \quad k_{PCM} = 0.17 \text{ W/mK}$$

$$\frac{A}{UA} = \frac{1}{h_c} + 1.6 \times 10^{-5} \left[\frac{m^2 K}{W} \right] + (0 \rightarrow 0.24) \left[\frac{m^2 K}{W} \right] \quad (17)$$

Thus the resistance of the flowing fluid has a greater effect at small values of x_m , the distance the melt front has propagated into the PCM. However, in a real system it takes time for the capture or recovery fluid flow to increase from zero at the initial condition to

full velocity at the bulk fluid temperature. The resistance equation was therefore considered when 10% and 90% of the PCM has been melted.

$$\frac{A}{UA} = \frac{1}{h_c} + 1.6 \times 10^{-5} \left[m^2 K/W \right] + 2.2 \times 10^{-2} \left[m^2 K/W \right] \quad @10\% \text{ melt}$$

$$\frac{A}{UA} = \frac{1}{h_c} + 1.6 \times 10^{-5} \left[m^2 K/W \right] + 2.0 \times 10^{-1} \left[m^2 K/W \right] \quad @90\% \text{ melt}$$

In order for the convection to comprise at least 5% of the thermal resistance with an estimated hydraulic diameter of 0.03m and a fluid conductivity of 0.6 W/mK and Prandtl number of 4.44, the value of h_c (the convective heat transfer coefficient) would have to be less than 900 at 10% melt and less than 100 at 90% melt. This means that increasing the convective heat transfer coefficient above 1000 would have only a small effect on the time required for 100% of the PCM to melt. It was therefore decided that the flow channel would be designed for a final temperature drop of approximately 1 °C and laminar flow.

The working fluid in the capture/recovery flow channel is water at temperatures between 5 °C and 75 °C. Using an estimated heat flow value of 90 W towards the end of the test, as determined from the quasi-steady resistance analysis shown in figure 4.4, the maximum flow rate for a 1 °C temperature difference was 0.0043 kg/s (0.26 LPM). The flow rate range for the test apparatus was therefore set to 0.0043 kg/s to 0.0266 kg/s (0.26 to 1.6 LPM).

With the given fluid and flow rate range, the internal cross-sectional dimensions to give laminar Reynolds numbers were calculated using equations 18 through 20.

$$\text{Re} = \frac{\rho V D_H}{\mu} \quad (18)$$

$$D_H = \frac{4A}{P} \quad (19)$$

therefore

$$\frac{4}{P} = \frac{\text{Re} \mu}{\dot{m}}$$

$$P = \frac{4 \dot{m}}{\text{Re} \mu} \quad (20)$$

This resulted in a channel perimeter of 0.228 m for a Reynolds number of 170 at the low mass flow and 1000 at the high flow. Since the PCM chamber minus a reasonable material thickness was 95 mm wide, the required depth was therefore 19 mm. Half of a rectangular aluminum channel measuring 101 mm by 51 mm with 3 mm wall thickness therefore comprised the upper portion of the flow channel. The lower portion was made by welding the resulting C channel on to a flat piece of aluminum large enough to accommodate the flange dimensions of the PCM chamber. The open ends were capped with appropriately sized aluminum sheet and fittings welded on to accommodate the fluid inlet and outlet.

A baffle near the inlet fitting distributed the flow more evenly within the capture/recovery channel. This baffle was constructed of a piece of aluminum sheet the same dimensions as the fluid flow cross-section with seven 9 mm holes drilled at even intervals along the horizontal centre-line. The effect on the flow distribution was confirmed using a three-dimensional computational fluid dynamics (CFD) study, the parameters for which are discussed in Chapter 4.5. A flow velocity map 3 mm from the

bottom surface of the flow channel is presented in figures 4.5 and 4.6 for flow rates of 0.26 L/min and 1.6 L/min. It can be seen in these figures that with the exception of a small stagnation zone (circled in the figures) in the centre after the flow passes through the baffle, the flow is relatively uniform across the width of the channel. Detailed drawings of the flow channel and flow distribution baffle can be found in Appendix A.

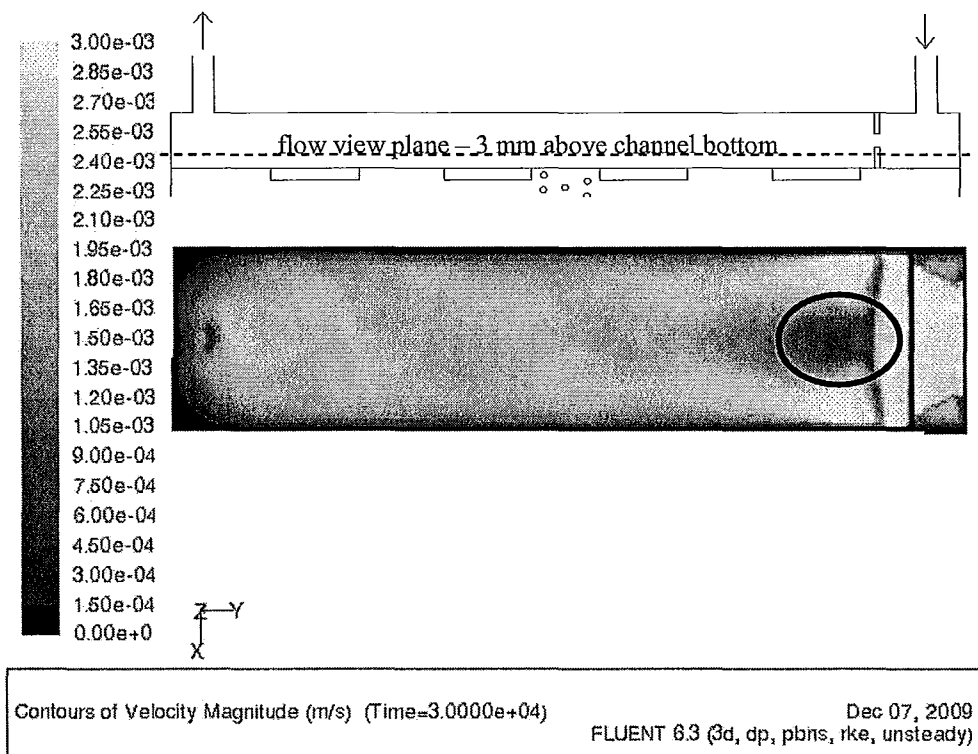


Figure 4.5: CFD flow distribution 3mm from the channel bottom for 0.26 L/min flow.

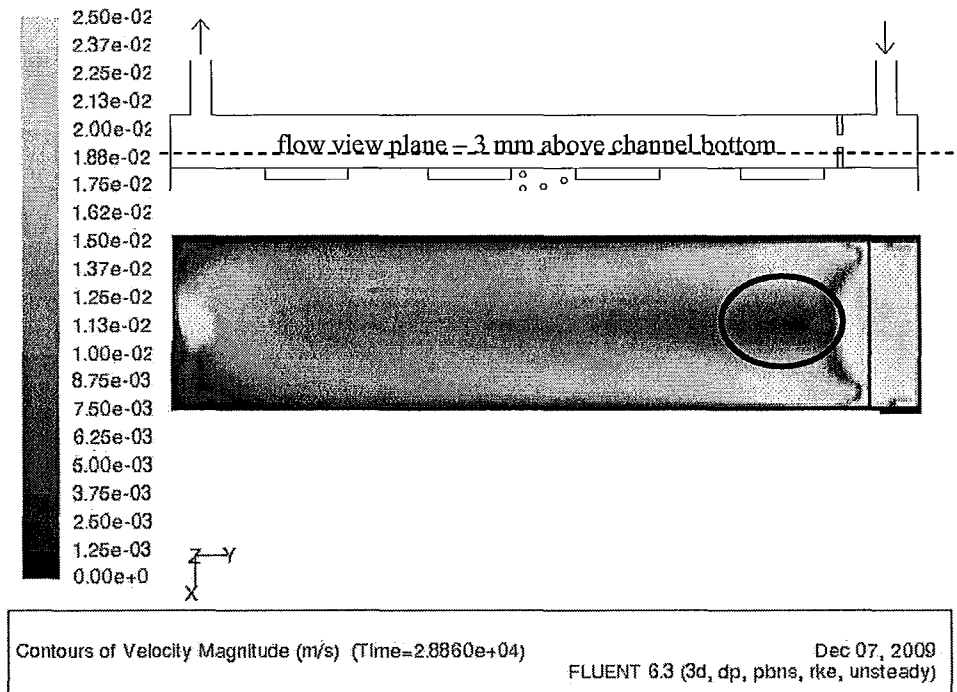


Figure 4.6: CFD flow distribution 3mm from the channel bottom for 1.6 L/min flow.

4.4 – Temperature Measurement

The temperature profile and the thickness of the melt zone as it propagates through the PCM were determined by recording temperature at several locations along the melt thickness. Sixteen thermocouples were located throughout the thickness of the PCM chamber, distributed in three columns.

In order to get an accurate temperature profile across the PCM thickness, the position of each thermocouple had to be known very accurately. Due to the forces generated in the PCM as it melts and solidifies, and therefore changes volume slightly, some method of holding the thermocouples in place was required. A central baffle was therefore employed to fix the position of the thermocouples. The locator holes, seen in

figure 4.7, had the same diameter as the thermocouple sheaths to ensure a tight fit and were located using a milling machine to ensure good positional accuracy (0.02 mm). The baffle material was chosen as polycarbonate to minimize the effect of the baffle on the melt time and temperature profile, as it has a similar thermal conductivity to many phase change materials. A three-dimensional CFD study was performed to determine the distance away from the baffle that the thermocouple junctions should be located in order to capture the PCM temperature with minimal distortion due to the presence of the baffle. This distance was set at 20 mm, based on the temperature profile in the liquid portion of the phase change material near the melt front at 25% melt, shown in figure 4.8. This is sufficiently far away from the baffle to measure the temperature of the phase change material outside the zone of influence of the baffle, which was approximately 12 mm on either side of the baffle centre.

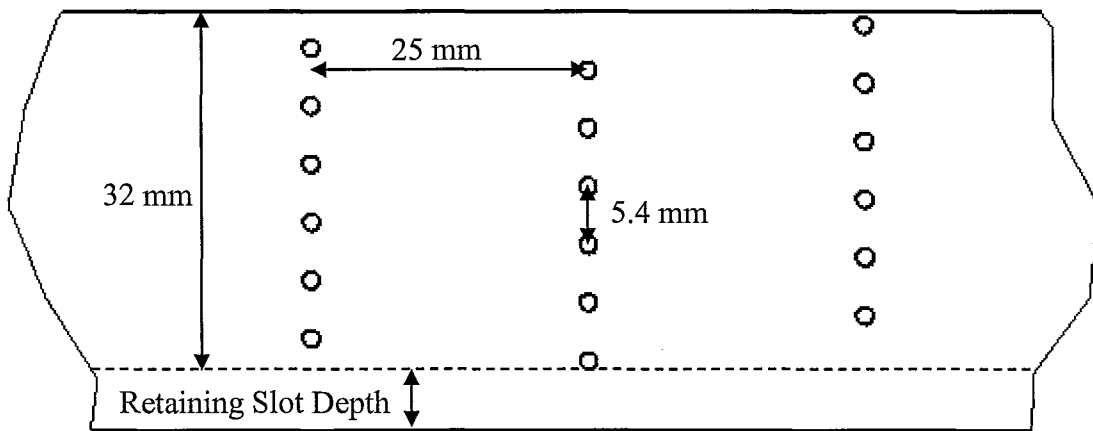


Figure 4.7: Thermocouple positioning hole pattern in the central baffle (thermocouple spacing in melt front propagation distance is 1.8 mm).

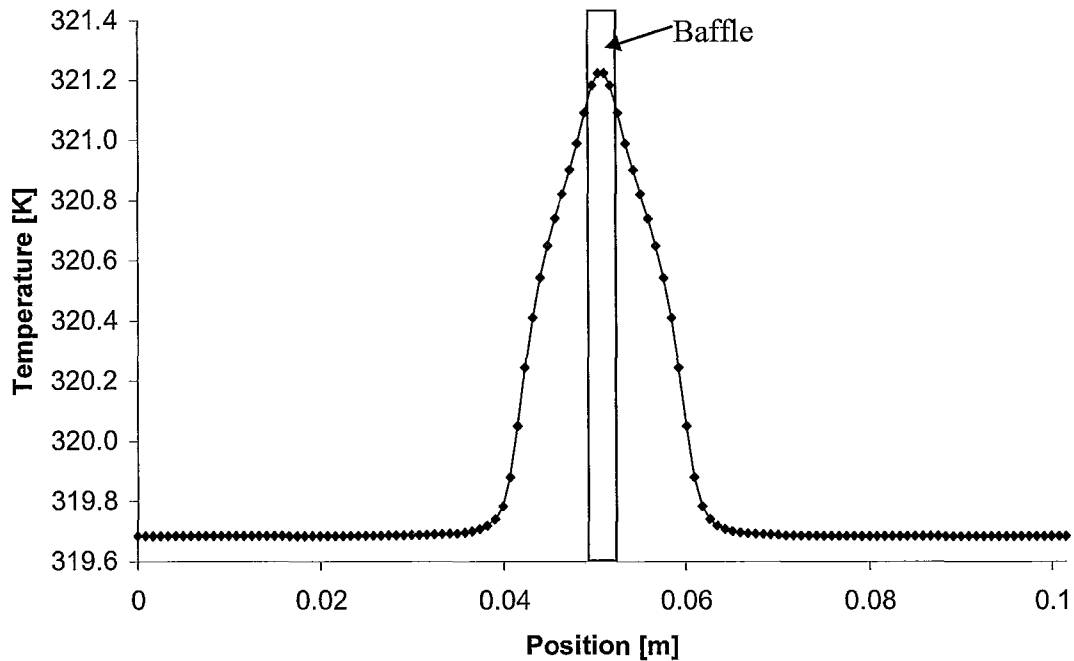


Figure 4.8: Temperature profiles near the baffle in the three-dimensional CFD study.

Type T thermocouples were chosen as they have the appropriate temperature range. Exposed junctions were selected in order to capture the temperature as accurately as possible at the chosen location.

4.5 – Flow Measurement and Control

A ThermoFisher Neslab RTE-10 Refrigerated bath with heating capabilities was used to maintain the capture/recovery water at temperatures between 5 °C and 75 °C to within approximately 2 °C. A miniature gear pump with flow rate up to 2 LPM and pressure drop capability up to 150 kPa was used to circulate the water through the flow channel. A flow meter capable of measuring flows between 0.11 and 2.6 LPM, Omega's

FP 5062, was used to determine the capture/recovery flow rate. Flow meter and pump specifications can be found in Appendix A.

4.6 – Heat Flux Measurement

Knowing the average heat flux into the PCM helps to validate the analytical model and give insight into the appropriateness of some assumptions. Measuring the average heat flux using the temperature difference and flow rate of the capture or recovery fluid would have been difficult due to the small water temperature differences between the inlet and outlet expected for the low heat flux either towards the end of the melt cycle or for high fluid flow rates. In order to measure the heat flux under these conditions, four heat flux sensors, Omega's HFS-4 model, with integral temperature measurement were cemented to the exterior of the flow channel where it contacts the PCM using high thermal conductivity epoxy. The position of the heat flux sensors can be seen in figure 4.9. These heat flux sensors were used to determine not only the average heat flux, but also the heat flux and temperature distribution on the surface of the flow channel. This helped to determine the validity of the quasi one-dimensional heat transfer assumption. The readings from these heat flux sensors were also time-integrated and checked against the amount of heat required to melt the known quantity of phase change material. Unfortunately, calibration of the heat flux sensors was unsuccessful as all available methods of verification available were less accurate than the heat flux readings expected in the experiments. Details on heat flux sensors can be found in Appendix A.

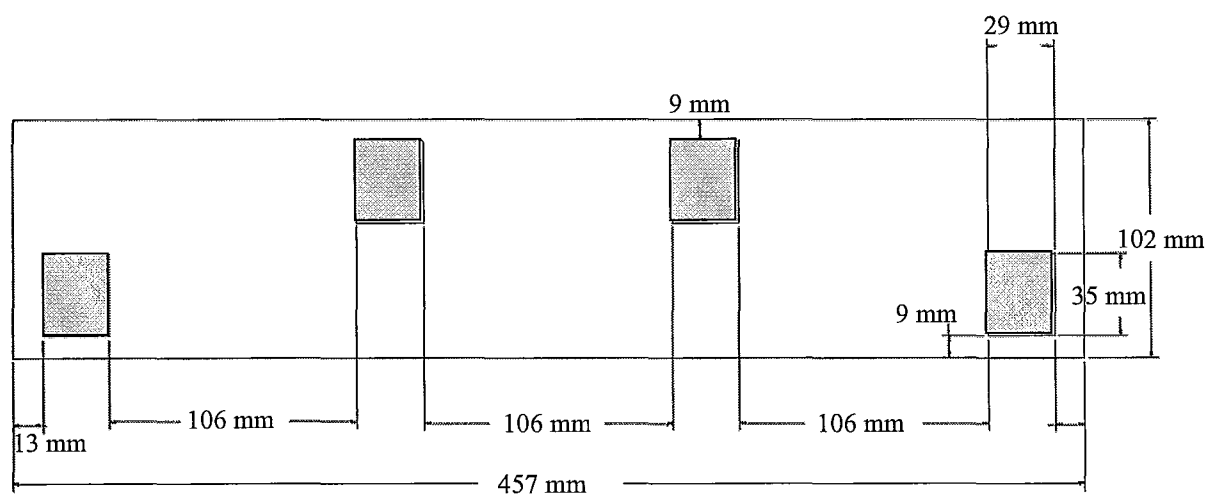
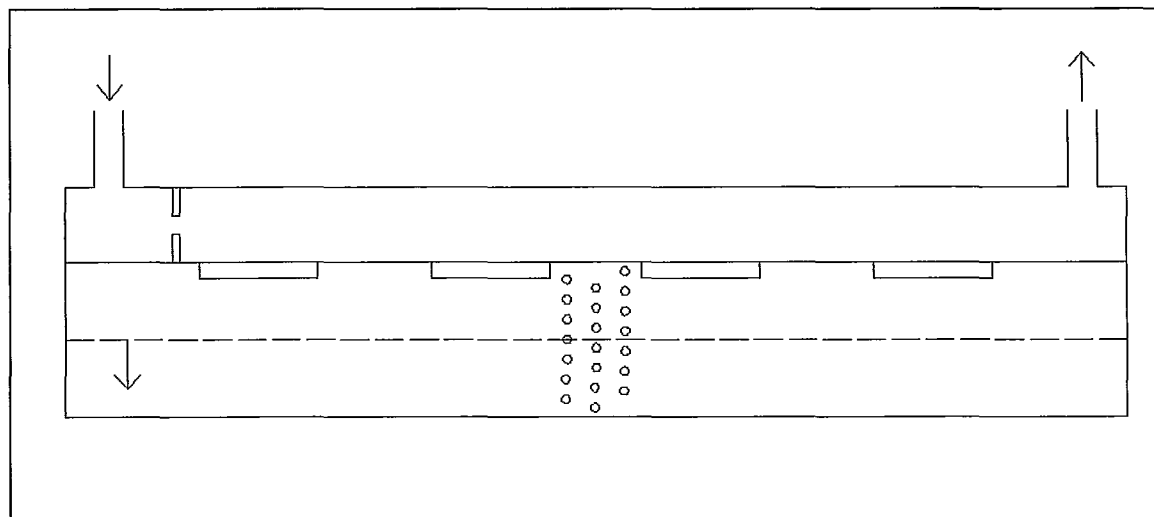


Figure 4.9: Position of heat flux sensors in the experimental set-up.

4.7 – Data Acquisition

A data acquisition system (DAQ) was required to interpret and record all output values from the thermocouples, heat flux sensors and flow meter. This data was recorded at least once every ten seconds and time-stamped in order to see how the values change with time. Enough channels to record 16-20 T-type thermocouples, four K-type thermocouples (cemented to the capture/recovery channel surface), four heat flux sensors

and the frequency signal from the flow meter were required. In order to meet these requirements, a Compact-DAQ system from National Instruments was used with a chassis that allows eight data acquisition cards simultaneously. The Compact-DAQ chassis sends the data to a computer via a USB cable and a custom LabView program records the data.

In order to record the thermocouple data a 16-channel thermocouple card, the NI-9213 was used. This allows recording of 14 of the thermocouples in the PCM chamber and the two flow temperatures. The flow meter requires a 5-24 V input and outputs a frequency signal at a slightly lower voltage. This voltage was determined by the relative resistance of the data acquisition and the pull-up resistor. Therefore a 24 V source was used in conjunction with a 2000 ohm resistor in order to produce a 14.4 V signal. With this signal it was possible to use the NI-9421 digital input card in slot six of the Compact-DAQ system, which has an integral counter, to measure the frequency of the flow meter. This card has a digital-on threshold of 13 V and a digital-off threshold of 5 V. This means that the 0-14.4 V frequency signal was properly interpreted.

The data was interpreted by LabView with all associated calibrations found in Appendix C applied to the raw signals. The LabView program then automatically sent the processed data to an Excel spreadsheet for further analysis.

4.8 – Experimental Uncertainty

According to Kline and McClintock (1953), experimental uncertainty of a measured value consists of a fixed (bias) error and random (precision) error. The total uncertainty is the root of the sum of the squared values of these two quantities. Bias errors can be obtained through calibration curves for most instruments. The experimental data recorded in this study were temperatures, heat fluxes and flow rate measurements.

Flow rate calibration was performed by collecting and weighing water passed through the meter for a given period of time and comparing it to the time-averaged values output by the data acquisition system. Calibration was performed using all of the hardware and software that is used in testing. The comparison was fit to a linear equation to obtain the calibration slope and offset for the flow meter, which can be found in Appendix C. Assuming a normal distribution, the standard deviation of the error between the reading and the measured value was found and the bias error for the flow meter set at +/- 12%, two standard deviations from the mean.

The thermocouple bias error consists of several cumulative sources. This includes: RTD calibration instrument uncertainty, RTD drift, RTD reference temperature uncertainty, RTD instrument uncertainty and thermocouple instrument uncertainty. Further uncertainty is introduced by the data acquisition system in the form of cold-junction compensation sensor uncertainty, gain error, offset error and gain error from source impedance (National Instruments, 2006). The PCM and flow thermocouples were calibrated against an RTD from 5 °C to 75 °C using the temperature controlled water bath. Using the same linear fit technique as the flow calibration but comparing to the

RTD as the “actual” value, the maximum range for two standard deviations of any of the thermocouples was 0.11 °C. This is smaller than the quoted +/- 0.5 °C from the manufacturer. The more conservative value from the manufacturer will therefore be used to determine the maximum possible error, while the tested range will be used for the expected error. The calibration coefficients for the thermocouples are found in Appendix C, table C.2. The bias of the RTD is quoted from the calibration lab as 0.057 °C, but due to potential gradients in the fluid bath and possible drift over time, this value will be increased by one order of magnitude to 0.57 °C. The expected cumulative bias for the thermocouples is therefore taken as 0.58 °C with the maximum cumulative bias at 1.1 °C. The K-Type thermocouples integral to the heat flux sensors were not calibrated, but rather the quoted error of +/-1 °C was used. Adding the expected and maximum bias from the data acquisition system brings the total bias error to +/- 1.2 °C and +/- 2.3 °C for expected and maximum errors respectively.

Random error is associated with the data fluctuations at a steady-state condition. In the case of the flow meter, this is quite complicated as it is difficult to achieve a constant flow rate for a long enough period of time to collect statistical data. For this reason, pumping noise will be included in the random error calculation for the water flow rate, even though it is physically present and therefore not really a component of the error. This results in a much larger flow rate error than is actually occurring. Taking 7500 data points without changing any of the pump system parameters gives a standard deviation of 0.0062 L/min for an average value of 2.73 L/min. A range of two standard

deviations corresponds to 4.5% of the flow rate. This value will therefore be used for the flow rate random error, giving a total flow rate error of +/- 13%.

Random error in the thermocouples is also difficult to assess due to the unsteadiness involved in taking temperature data over a long period of time. For this reason solidification data during natural cooling was used such that the temperature of the thermocouples in the phase change material chamber remained at the freezing temperature for an extended period of time. The random error found from taking two standard deviations of this data was 0.23 °C. This brought the total expected thermocouple temperature uncertainty to 1.2 °C with a maximum uncertainty of 2.3 °C. The expected uncertainty was used for error calculations.

Positional uncertainty also exists when using the thermocouple readings to estimate the position of the melt front or determine the temperature gradient. This uncertainty was set to +/- 2 mm after physical testing of the maximum movement of the thermocouples under a manual load. All of these sources of uncertainty will be taken into account when comparing the test data to the analytical and CFD models.

CHAPTER 5 – Experimental Results, Discussion and Comparison

5.1 – Experimental Phase Change Results and Model Validation

In order to compare the experiment to the analytical and CFD models, the figure of merit used is the time to melt at various locations, specifically the half-melt time at a depth of 0.016 m. The heat flux into the cell is also compared to ensure that the trends and magnitudes are as expected. The first occurrence of a thermocouple reading above the full melt temperature threshold of 43.5 °C is used to determine the time to convert the PCM to liquid at that location. The average of all recorded values of inlet and outlet capture fluid temperature is used as the bulk fluid temperature in the analytical model, with the initial temperature set as the average of the PCM thermocouple readings at time zero. This is an approximation since the average fluid temperature differs between the two tests and varies with the heat flux during the tests. The Reynolds numbers for the range of test cases were found using equation 21 with mass flow rates of 0.00435 and 0.0266 kg/s, a perimeter of 0.228 m and viscosity of 0.000453 kg/ms. Because the Reynolds number range was between 100 and 1100, laminar correlations were used for the capture/recovery flow. The Nusselt number of 4.44, based on fully developed flow in a rectangular duct with constant surface temperature and aspect ratio of 1:4 (Shah & London, 1978) was used to determine the convective heat transfer coefficient in the

capture/recovery fluid. Because the calculated entrance length range for this geometry is 10-25 hydraulic diameters, there is error involved in using a fully developed Nusselt number for this channel, which is only 0.6 m, or 20 diameters long. To estimate the magnitude of this potential error, the correlation for annular tubes with a diameter ratio of more than 0.5 was used. This produces a Nusselt number range between 4.43 and 5.74 (Kays & Perkins, 1972). A Nusselt number of 5.74 rather than 4.44 produced only a 2.5% difference in the time to 100% melt for the tested cases. The fully developed Nusselt number of 4.44 was therefore used to calculate the heat transfer coefficient of 84 W/m²K in the model using equation 22.

$$\text{Re} = \frac{\rho V D_H}{\mu} = \frac{4\dot{m}}{P\mu} \quad (21)$$

$$h = \frac{Nu k}{D_H} = \frac{Nu k P}{4A} \quad (22)$$

5.2 – Lauric Acid Storage Cell Low Flow

Figures 5.1 and 5.2 show the time to melt for the thermocouple locations within the lauric acid test cell for the first two tests with a capture flow of 0.26 LPM (0.00435 kg/s, Re = 170) at 63 °C. Since some of the thermocouples were damaged upon installation, temperature readings were not available for all of the positions within the PCM. Each of the available locations, however, has horizontal error bars of +/- 2 mm to represent the uncertainty in thermocouple position and melt time error bars of +/- 1.2 C, shown vertically. The half-melt time for the analytical model and CFD results are shown in table 5.1. The analytical model consistently under-predicts the measured time to half-

melt by about 21%, which is within the measurement error, while the CFD model under-predicts this same value by 36%. The CFD results use local temperatures and Nusselt numbers to calculate the heat transfer for each cell in the mesh, while the analytical model assumes a fully developed Nusselt number and uniform temperature for the entire domain. This explains some of the discrepancy between the CFD and analytical model and why the analytical model predicts a longer melt time.

Table 5.1 Comparison of half-melt time predictions for tests 1 and 2 with CFD, and analytical models.

	Test 1	Test 2	Analytical	CFD
Half-Melt Time [h]	3.09	3.18	2.48	2.00
Difference from Test Average	-1.4%	+1.4%	-21%	-36%

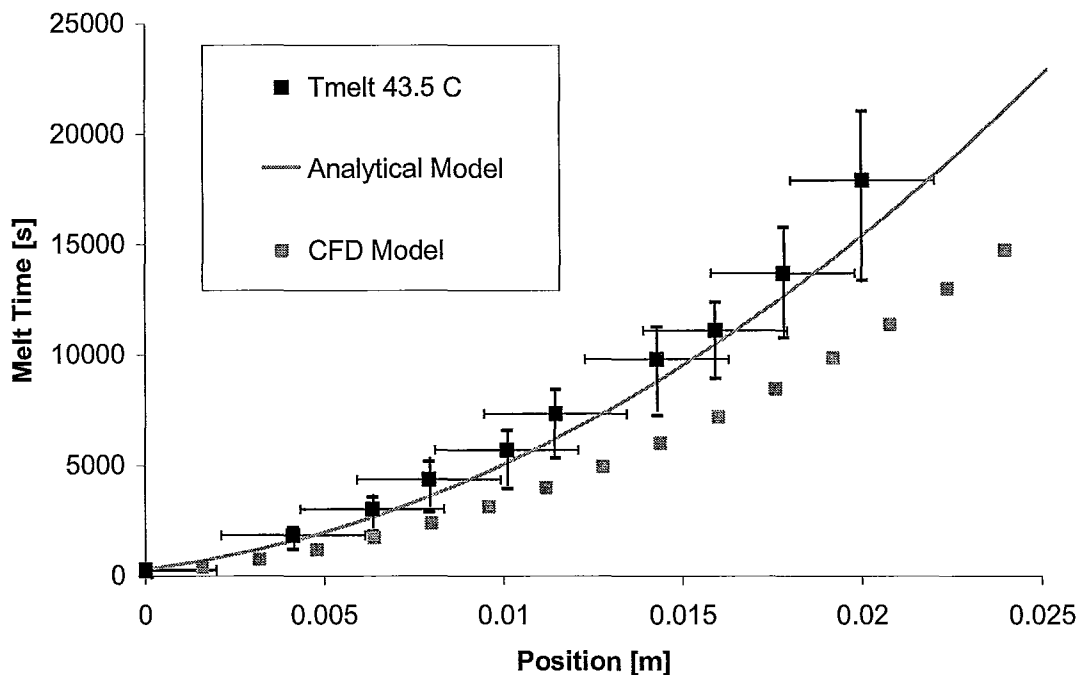


Figure 5.1: Lauric acid test 1 melt time results compared to analytical and CFD models.

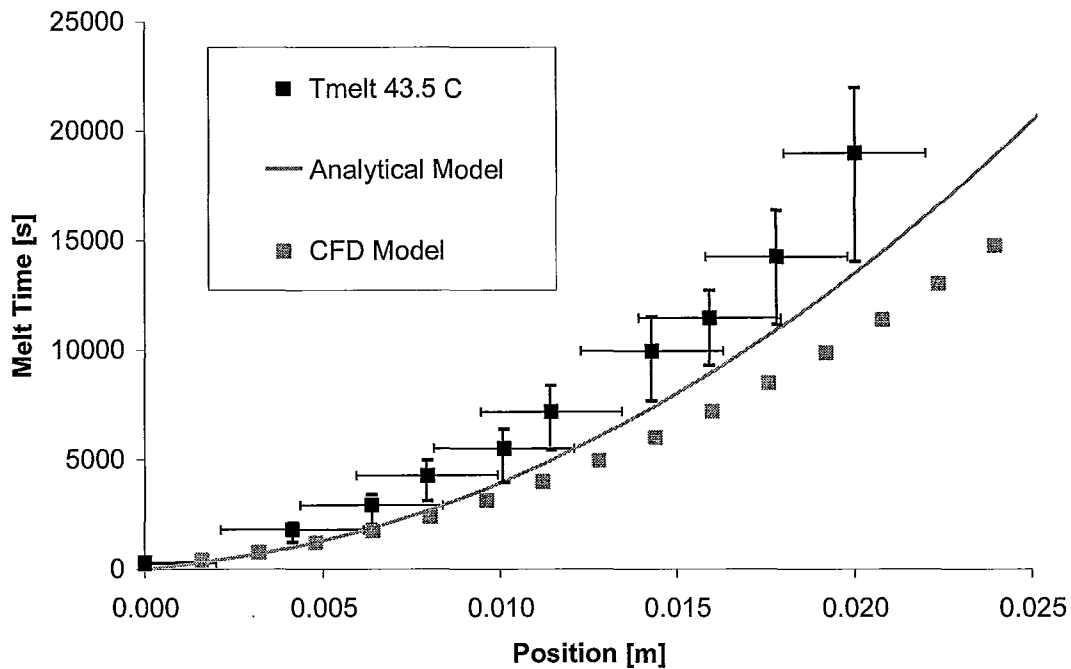


Figure 5.2: Lauric acid test 2 melt time results compared to analytical and CFD models.

Melt times for the two low flow cases are seen in figure 5.3 and data from the second test show agreement to within 10% of the first test for all melt fractions. The 50% melt time is within 2.2% and the final melt time within 6%. This shows that despite differences in initial temperature and average capture fluid temperature, melt time results are relatively repeatable. The original criteria for the experimental rig included sufficient insulation to ensure a uniform initial temperature for both capture and recovery tests. When the rig was built and tested, however, the insulation could not be applied as intended, resulting in significantly larger insulative losses than desired. This meant that the initial cell temperature was warmer in the centre and cooler near the outer edges and this varied between tests based on the room temperature and temperature to which the rig

was originally heated. In future testing it is recommended that the insulation be improved in order to mitigate the heat loss.

To further compare the test data with model results, figures 5.4 and 5.5 show the heat flux values for the test data, analytical and CFD models. Heat flow values were calculated using the heat flux and multiplying it by the relevant area. For the CFD case, this area was 0.129 m^2 and accounted for the averaged heat flux readings over the top, bottom and sides of the PCM chamber in order to capture all of the heat flow into the PCM. Since the output data was an area-weighted average of the total surface heat flux for this entire area, this value must be used to calculate the total thermal energy input to the cell. The test data and analytical solution use only the capture/recovery flow channel area in contact with the PCM, which is 0.046 m^2 . The channel surface was divided into four zones with the divisions equidistant between each pair of neighbouring heat flux sensors. The reading from each heat flux sensor was then assigned to the entire area containing that sensor and the four were summed to produce the total thermal energy input through the surface of the flow channel.

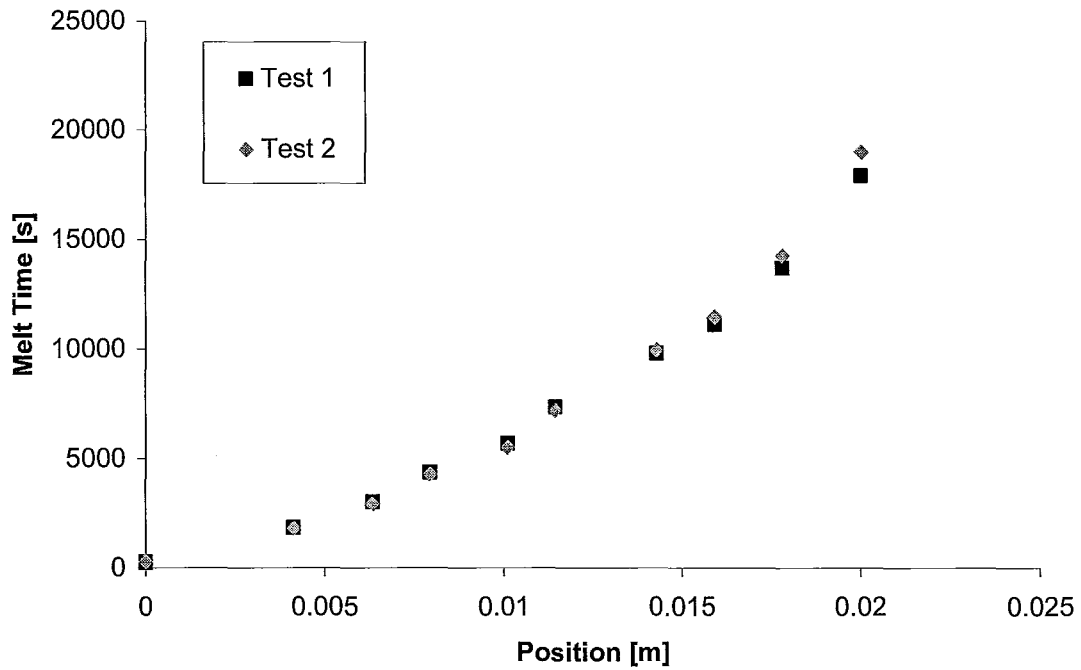


Figure 5.3: Repeatability comparison of lauric acid tests 1 and 2 melt time results.

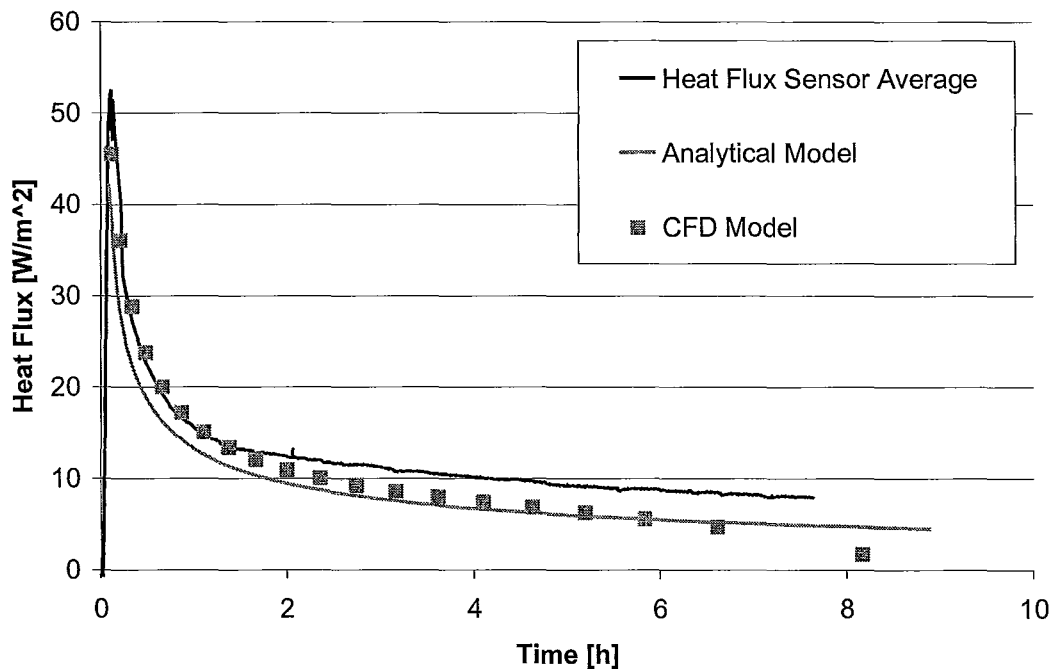


Figure 5.4: Lauric acid test 1 heat flux results compared to analytical and CFD models.

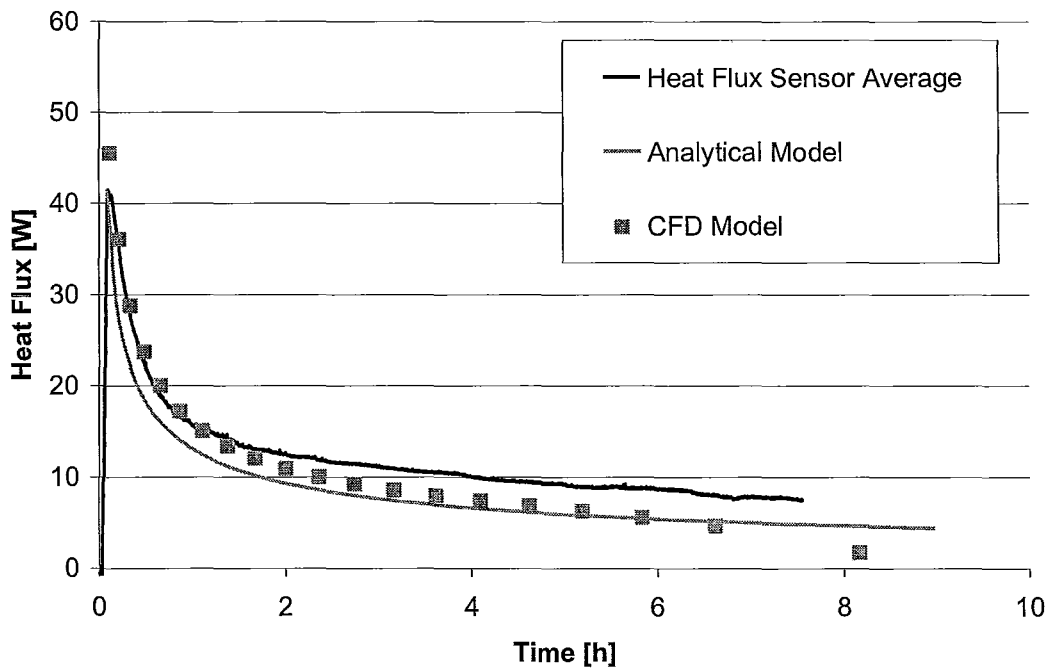


Figure 5.5: Lauric acid test 2 heat flux results compared to analytical and CFD models.

Both the CFD and analytical models under-predict the majority of the heat flux and melt time results seen in the first two test cases. It would be expected that if the heat flux is under-predicted by a model this would result in the melt time being over-predicted, but this would only occur for a perfectly insulated test apparatus. The fact that there are thermal energy losses to the surroundings, as approximated in Appendix C, causes additional heat flux through the capture/recovery channel wall that does not cause melting of the phase change material. Given these losses, it is therefore expected that the average of the heat flux sensor readings would be higher than the heat flux predicted by the analytical or CFD models, as seen in figures 5.4 and 5.5.

5.3 – Effect of Flow Rate

Increasing the capture fluid flow rate from 0.26 LPM to 1.6 LPM decreased the half-melt time by 34% as compared to the 43% decrease expected from the analytical model due to the differences in initial and bulk fluid temperature (initial temperatures of 35.9 °C in test 1 and 40.0 °C in test 3 and capture fluid bulk temperatures of 62.9 °C in test 1 versus 65.4 °C in test 3). The times to melt for test 3 with the 1.6 LPM flow rate can be seen in figure 5.6. The analytical model prediction for half-melt is 3% higher than the experimental data in this case, while the CFD under-predicts by 11%. The improvement in the predictive capability of the analytical model in this case may result from the decrease in the capture fluid residence time. This produces a much more uniform capture temperature and is therefore closer to the one-dimensional assumption used in the model. The heat flux prediction for this higher flow case is also improved, as seen in figure 5.7.

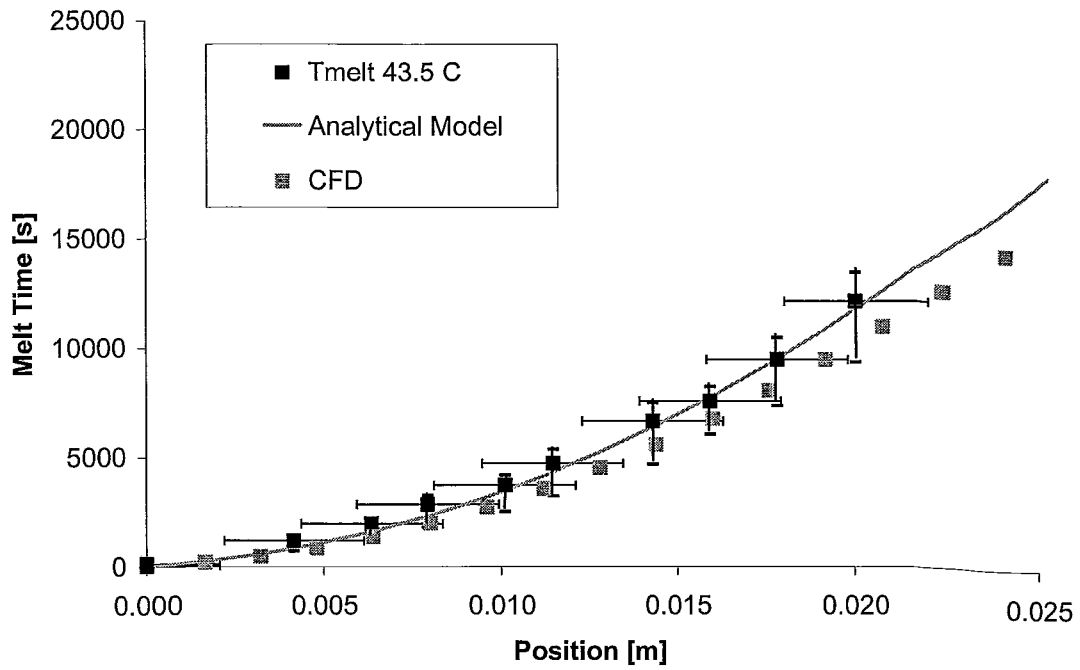


Figure 5.6: Lauric Acid test 3 melt time results compared to the analytical model.

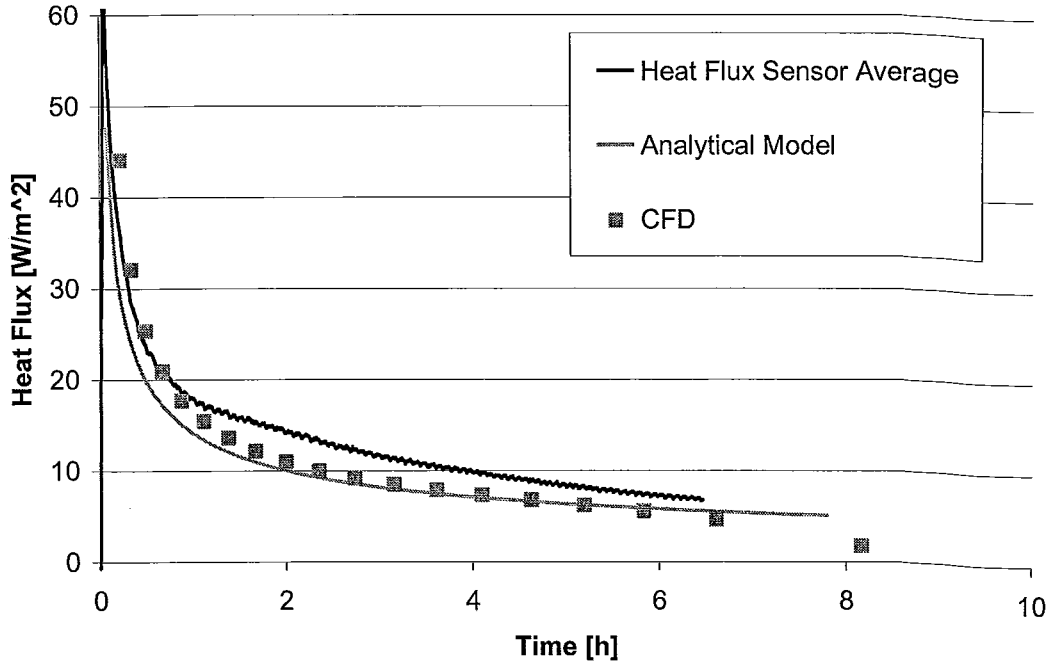


Figure 5.7: Lauric Acid test 3 heat flux results compared to CFD and the analytical model.

5.4 – Effect of Flow Direction

The presence of the flow baffle in the capture/recovery flow channel has an effect on the fluid flow pattern. For this reason, the high flow rate test was repeated twice with the capture channel plumbed in the opposite direction to evaluate these effects. There were two differences in the geometry of tests 3 and 4. The first of these is a slight change in the way the fluid entered and exited the flow channel. For tests 1 through 3 the tee fittings that allowed the thermocouple to be inserted into the flow immediately adjacent to the bosses were oriented with the run branches pointed away from the flow channel. The addition of quick disconnect fittings between tests 3 and 4, as well as handling issues caused by the long thermocouple leads protruding upward from the fittings, necessitated turning these fittings such that the run was oriented parallel to the flow channel. This may have caused small differences in the flow entering the channel, but these effects do not show a significant effect on the melt times.

The melt time results for these three high flow tests are shown in figure 5.8 and are very similar, with the exception of one outlier point. The melt time for 50% melt (0.016 m) is more than that for 63% melt (0.020 m), which does not make physical sense for a planar melt front. This outlier may be caused by uneven melting of the phase change material since these two thermocouples are positioned in different columns in the baffle, by trapped gas bubbles or foreign matter inclusions within the phase change material at the thermocouple skewing the melt data, or by a change in position of some of the thermocouples.

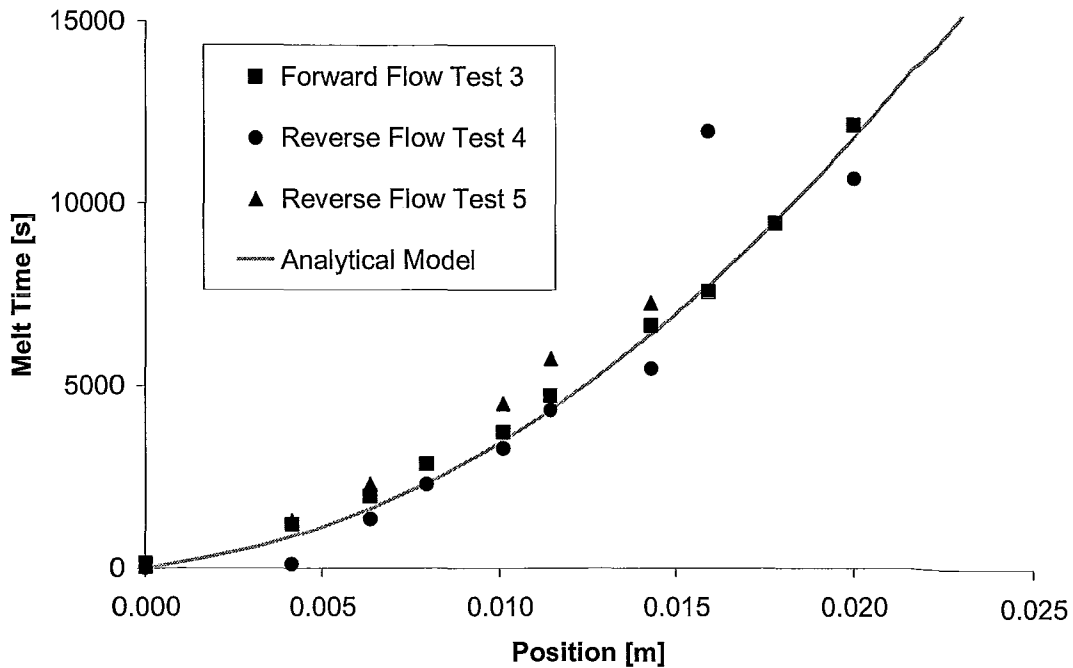


Figure 5.8: Lauric Acid tests 3 and 4 comparing flow direction for 1.6 LPM capture flow.

Investigation into the cause of the outlier in figure 5.7 involved draining the phase change material from the apparatus and observing the thermocouple position and condition within the test cell. The first observation that was made was the discoloration of the phase change material. New lauric acid is opaque white in the solid form and clear in the liquid form. When the lauric acid was drained from the test cell it was translucent yellow-orange in colour and solidified to an opaque yellow-orange. Since this discoloration was not observed in thermal cycling in glass containers, it was hypothesized that the phase change material reacted with one of the apparatus materials. Inspection of the silicone caulking showed a similar yellowing of the sealant to the phase change material. It was therefore hypothesized that a chemical reaction between the silicone

caulking used to help seal the flanged components of the test cell and the phase change material may have caused the discoloration of the lauric acid. A simple test was conducted to verify this hypothesis by placing a sample of cured silicone in a glass container with new phase change material and cycling it twice above and below its melt temperature. No yellowing of the phase change material and silicone was seen during this investigation as in the original tests, disproving the hypothesis that a reaction between only the PCM and silicone sealant was causing the discolouration. It is therefore recommended that further material compatibility testing be performed for additional material combinations that occur within the cell.

With the exception of the possibility of uneven melting caused by local material property changes due to this chemical reaction, a reasonable explanation was not found for the outlier and more investigation is therefore required.

5.5 – Discussion

The analytical model developed in this study produces reasonably similar results to those from CFD analysis with similar boundary conditions and experimental data. This supports the use of this model in preliminary sizing calculations and preliminary assessment of phase change material thermal storage systems. The under-prediction of the melt times may be attributed to thermal energy losses due to insufficient insulation in the test apparatus. If this is not the case, however, and the model under-predicts melt times for well insulated systems, it means that a system sized on a given melt time may have a slightly thicker PCM layer than the final design requirement. This would cause a

corresponding under-prediction of the volume multiplier based on a given capture and recovery channel geometry. This is not likely, however, as natural convection within the liquid phase change material should increase the heat flux of the cell above that predicted by the analytical model. The effect of an error in the prediction of the melt time will have less of an effect for longer storage cell times due to the smaller volume multipliers calculated in these cases. For example, a 20% error in the PCM thickness for a geometry where the PCM occupies 50% of the cell causes a volume multiplier range of 1.83 to 2.25, while a 20% error in the PCM thickness for a geometry where the PCM occupies 90% of the cell has a volume multiplier range of only 1.09 to 1.14. This does not change the cost of the phase change material required to store the required amount of energy, but can have a significant effect on the total system volume and the cost of the capture and recovery channel materials in the system. The effect of a 20% error in PCM cell thickness on an actual system will be evaluated using the H₂Green Distributed Storage System thermal energy storage battery design in the following chapter.

CHAPTER 6 – Sample System Sizing

6.1 – H₂Green Distributed Storage System Thermal Storage Sizing

Sizing of a sample system is demonstrated based on inputs from the proposed Distributed Storage System (DSS) from H₂Green Energy Corporation. The capture and recovery systems are based on utilizing the DSS at McMaster Innovation Park, a 170,000 square foot industrial research facility owned by McMaster University. This demonstrates the utility of the analytical thermal battery sizing methodology in determining the size and economic feasibility of utilizing thermal energy storage in a specific application.

6.2 – H₂Green Distributed Storage System

H₂Green's DSS is an energy storage system based on time-of-day electricity pricing. The system stores energy from the electrical grid at times when it is cheap and abundant for use during times when it is costly and limited in availability. This system can also be used to store energy during excess supply of renewable energy sources when demand is not present. The storage system can be made in various sizes using various different types of energy storage such as pumped hydro, compressed gas, mechanical flywheels and chemical energy (such as turning water to hydrogen and oxygen). The system under investigation is a small-scale storage system that uses hydrogen as the storage medium in order to store and recover energy for an office building, as depicted in

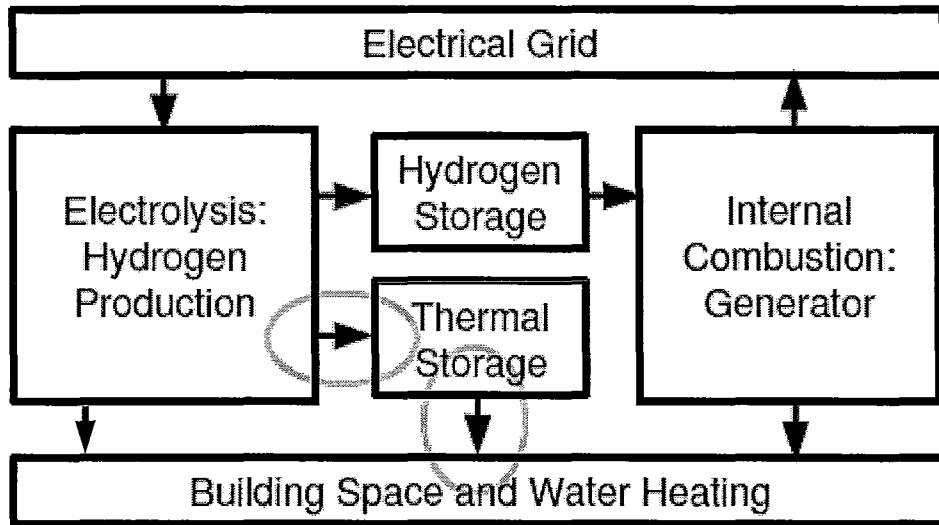


Figure 6.1: Schematic representation of the H₂Green Distributed Storage System.

figure 6.1. The electrolysis and electrical generation system sizes were not predetermined, but rather based on the thermal load of the site.

The hydrogen is created using a commercial electrolysis unit during off-peak pricing periods and electricity regenerated using a high efficiency hydrogen internal combustion engine (ICE) during peak pricing periods. No hydrogen or electricity production occurs during mid-peak pricing periods, as this provides a lower rate of return.

Time-of-day pricing in the province of Ontario in January 2009 was used to determine the timing cycle and is shown in table 6.1 (Ontario Energy Board, 2009). This gives a maximum capture time of 57 hours during weekends with a capture to recovery time ratio of 102 : 30 during the summer and 102 : 35 during the winter. In order for this system to break even in terms of operating efficiency for electrical storage only, the ratio

Table 6.1: Time-of-day electricity pricing in Ontario, January 2009 (Ontario Energy Board, 2009).

Day of the Week	Time	Time-of-Use	Price (cents/kWh)
Weekends & Holidays	All day	Off-peak	4
Summer Weekdays (May 1st - Oct 31st) View chart	7:00 a.m. to 11:00 a.m.	Mid-peak	7.2
	11:00 a.m. to 5:00 p.m.	On-peak	8.8
	5:00 p.m. to 10:00 p.m.	Mid-peak	7.2
	10:00 p.m. to 7:00 a.m.	Off-peak	4
Winter Weekdays (Nov 1st - Apr 30th) View chart	7:00 a.m. to 11:00 a.m.	On-peak	8.8
	11:00 a.m. to 5:00 p.m.	Mid-peak	7.2
	5:00 p.m. to 8:00 p.m.	On-peak	8.8
	8:00 p.m. to 10:00 p.m.	Mid-peak	7.2
	10:00 p.m. to 7:00 a.m.	Off-peak	4

for peak to off-peak price of 8.8 : 4 would require a round-trip storage efficiency of $4/8.8$ or 45%.

Analysis of the proposed system can give an estimate of the storage efficiency and therefore determine whether it meets the break-even efficiency for storage only. Product literature from Hydrogenics Corporation shows that the HySTAT-A electrolysis unit requires 4.8 kWh (1.7×10^7 J) to produce one normalized cubic meter of hydrogen at a maximum storage pressure of 25 bar (Hydrogenics, 2009). Compressing the gas by eight fold (400 bar) requires additional energy, resulting in an input requirement of 6.4 kWh/Normalized_m³ (Praxair, 2009). A turbo-charged internal combustion engine can be used to turn the hydrogen back into mechanical and then electrical energy and could achieve a conversion rate of approximately 50% of the higher heating value of hydrogen (Shudo, 2007). This results in 1.77 kWh (6.37×10^6 J) of energy being produced for every normalized cubic meter of hydrogen gas. The maximum attainable storage efficiency of such a system would therefore be $1.77 / 4.8$ or 37%. If compression to

400 bar is required for storage at a compression efficiency of 75% (Praxair, 2003), this number is further reduced to 28%. Since both are lower than the break-even operating efficiency of 45% dictated by the pricing ratio, additional sources of revenue must be included to produce an economically feasible system.

While feed-in tariffs for off-peak energy storage are a possibility in the future, they are not currently available and were therefore not evaluated in this study. Sale of oxygen gas from the electrolysis process is also a potential source of income, but contracts would have to be negotiated with a buyer and these would be highly dependent on the pressure and purity of oxygen that is provided. As these values were also unavailable, this source of revenue were also not evaluated in this study. Displacement of natural gas heating costs for the building in which the system is housed using a thermal energy storage system was calculated with readily available data.

6.3 – Capture and Recovery System Definition

The thermal energy storage system will be based on the phase change material thermal battery design process presented earlier in figure 2.3 and reproduced in figure 6.2 with numbered steps for easy reference.

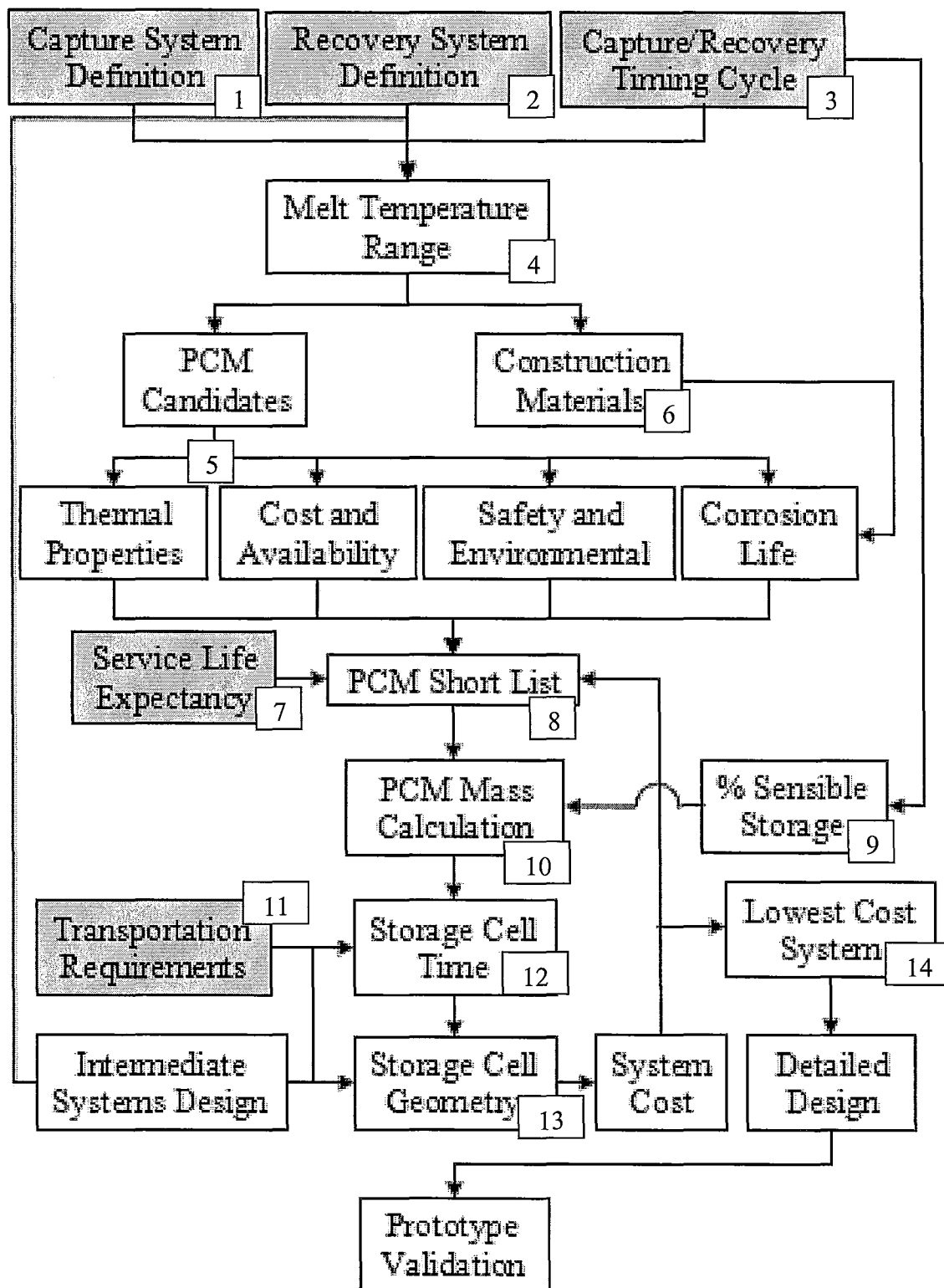


Figure 6.2: Design methodology for H₂Green Distributed Storage System thermal battery.

The capture system, specified in step 1, will therefore be the electrolysis unit which produces excess thermal energy at approximately 80 °C (353.15 K), the optimum operating temperature of the unit. In order to preserve as much of the availability of the thermal energy as possible, a closed system utilizing the primary fluid as a heat transfer medium (liquid caustic solution, with approximately the same properties as water) has been used. While there is also excess thermal energy from the hydrogen internal combustion engine (ICE) while it is generating electricity, this occurs primarily at times when the building is occupied, and this energy can therefore be used directly for heating or hot water needs without storing it in the thermal battery.

The recovery system for the DSS, specified in step 2, was the building's HVAC system. The sizing was performed with focus on the winter months, but a similar system may be used in the summer months in conjunction with an absorption cooling system to aid the in conditioning. It was therefore assumed that the recovery system uses the primary fluid (air) in an open system that adds thermal energy to fresh air from the outdoors and provides it to the building. The goal was to heat the recirculated air from 20°C to 50 °C so that it can be mixed with fresh air to provide warm air at approximately 30 °C to the occupied space. The capture/recovery cycle, specified in step 3, was therefore based on capturing during times of off-peak electricity cost and recovering during times when the building is occupied and heating is required. Based on the specified capture and recovery systems, the PCM melting and freezing temperatures should be in the range 60-70 °C (333.15-343.15 K), as specified in step 4 of the design process.

6.4 – PCM Selection

Using PCM material summaries from a literature review (Zalba et al. 2003) with updated properties from the manufacturers (Rubitherm, 2009) a list of candidate materials for energy storage is prepared as step 5 and presented in table 6.2 along with required construction materials (step 6). All available properties were included to evaluate the different materials and narrow the list based on undesirable heat transfer properties, high cost or service life expectancy of less than 10 years (step 7). In the search for additional properties of Sodium Hydroxide it was determined from figure 6.4.1 that the required concentration of NaOH in water to achieve the listed properties is approximately 68% by weight (Dow Chemicals, 2009). This is much higher than the saturation solution quantity of 52% at room temperature (Solvay Chemicals, 2009), seen in figure 6.4.2, which would result in a decrease in concentration due to precipitate forming if the solution were cooled, as is likely during initial manufacture, shipping and start-up. This would then change the properties, making this material unacceptable for use as a PCM. Since RT65 is a stabilized form of paraffin, it will be used instead of n-triacontane to evaluate the paraffin family. Several of the materials on the list are not common chemical compounds and prices were therefore not available from suppliers for Polyglycol E6000 and Palmitic Acid, which were eliminated on this basis, but should be investigated further when data becomes available. The short list (step 8) is thus the highlighted materials in table 6.2.

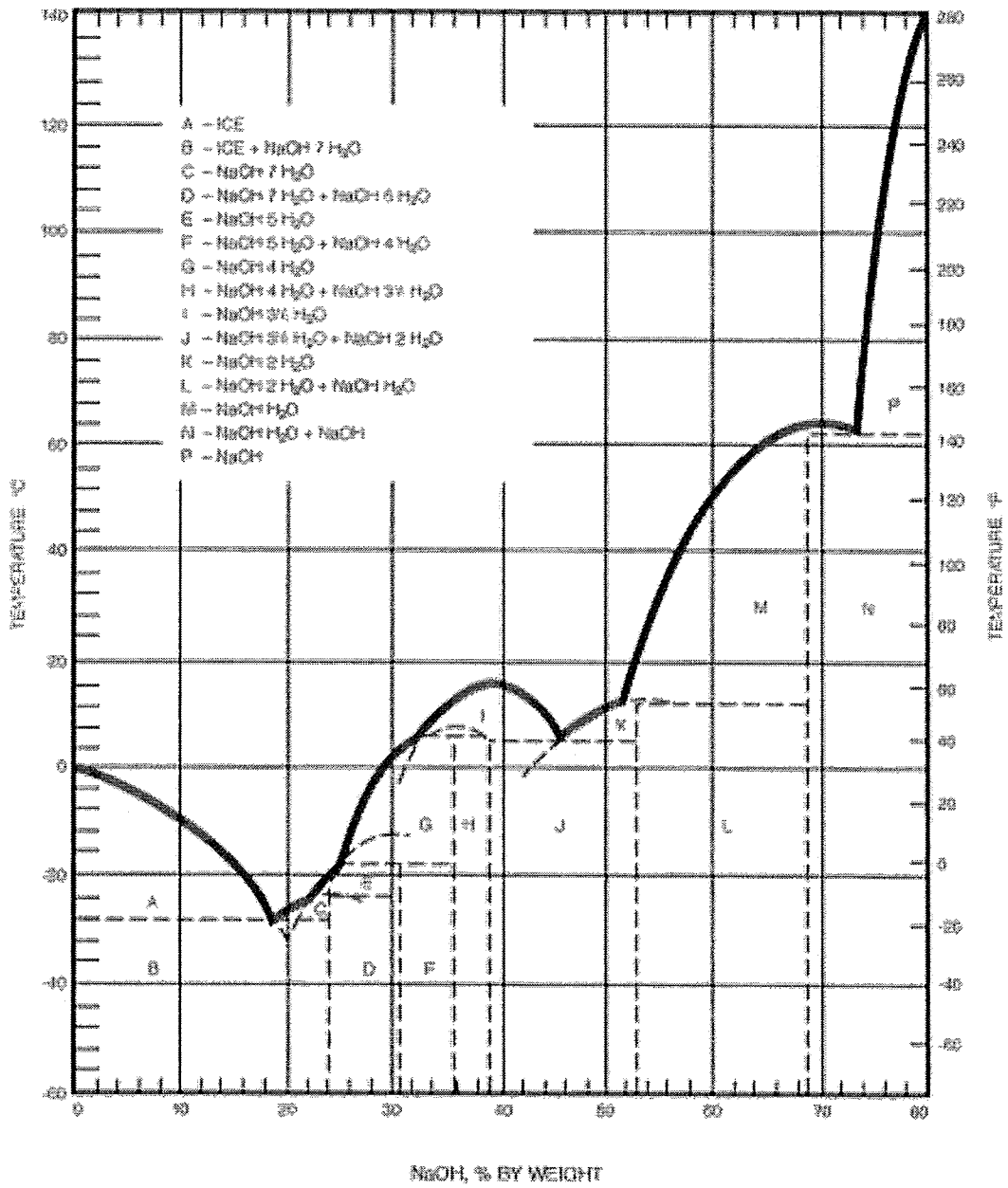
The decision of whether or not to store some sensible energy is based on the capture/recovery systems and timing as well phase change material properties. In the case of the proposed system, there is only a small temperature difference between the

capture fluid at 80 °C and the PCM melt temperature (60-70 °C). This would make resistance to imparting sensible energy on the PCM above its melt temperature significant, as there is very little gradient to drive the heat transfer. Because of this small temperature difference, only 4 degrees of sensible thermal energy will be stored to ensure the PCM has fully melted.

In order to perform step 10, calculation of the PCM mass required, we first need to look at the heating and electrical needs of the building in question in order to properly size the thermal battery and distributed storage system. Since excess electricity would be sold back to the grid, the system will be sized based on heating requirements.

Table 6.2: List of PCM candidates with melt temperatures between 60 and 70 °C.

Name	Melt temperature [C]	Heat of Fusion [kJ/kg]	Density (l) [kg/m ³]	Required Volume [m ³ /MJ]	Required Mass [kg/MJ]	Price [\$/kg]	Cost per MJ [\$/MJ]	Required Materials
Sodium Hydroxide	64	227.6	1690	2.60E-03	4.39	\$0.95	\$4.17	Stainless Steel
Tetrasodium Pyrophosphate Decahydrate	70	184	1820	2.99E-03	5.43	\$5.45	\$29.62	Stainless Steel
Polyglycol E6000	66	190	1085	4.85E-03	5.26		n/a	Aluminum
Stearic Acid	69	203	848	5.81E-03	4.93	\$1.30	\$6.40	Aluminum
Palmitic Acid	64	186	850	6.33E-03	5.38		n/a	Aluminum
Paraffin C31 (n-Triacontane)	67	189	830	6.37E-03	5.29		n/a	Aluminum
RT65	66	152	780	8.43E-03	6.58	\$3.79	\$24.95	Aluminum



NOTE.
 THE CURVE INDICATES THE POINT AT WHICH CRYSTALS EXIST IN CONTACT WITH SOLUTION.
 From T.P. HOU, Manufacture of Soda Ash, 2nd Ed. N.Y., Reinhold Publishing Corp., 1942.
 From Industrial Engineering Chemistry, Vol. 48, No. 11, p. 2401.

Figure 6.4.1: Solidus temperature for NaOH + H₂O systems (Dow Chemicals, 2009).

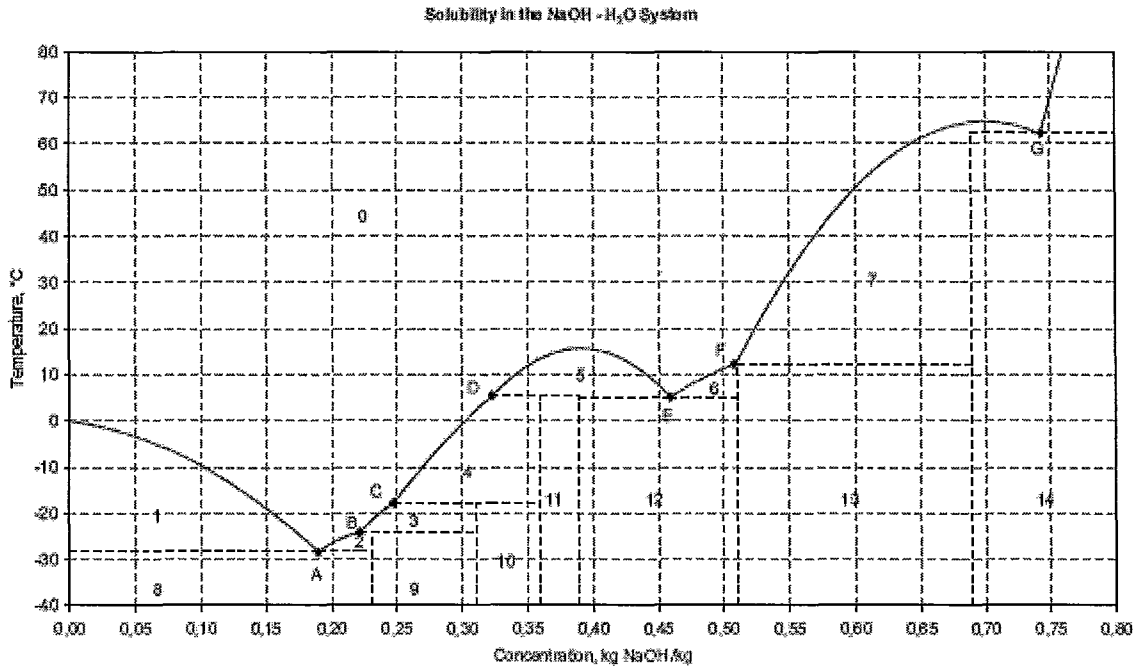


Figure 6.4.2: Saturation levels for NaOH + H₂O systems (Solvay Chemicals, 2009).

6.5 – McMaster Innovation Park Heating Needs

McMaster Innovation Park (MIP) used a projected \$44,000 of natural gas combustion with forced air circulation for its space heating and hot water needs in 2009. Forced air heating is common practice for many facilities in Canada due to the climate necessitating heating in the winter and cooling in the summer. The approximate natural gas monthly usage at MIP for the year 2009 can be seen in table 6.3 (Sandwell Consulting, 2008).

Table 6.3: Estimated natural gas usage per month [therms] at McMaster Innovation Park (Sandwell Consulting, 2008).

Jan	Feb	Mar	Apr	May	Jun	Jul	Aug	Sep	Oct	Nov	Dec	Total
16316	14363	16945	6374	1947	494	149	198	1377	5170	8337	16770	88442

Thermal energy usage for the winter months (December to March) therefore averages to 16,100 therms (1700 GJ) per month. At an assumed 85% gas furnace efficiency based on the higher heating value of natural gas (38,200 kJ/Normalized_m³), this is an average winter heating requirement of 334 GJ each week. With 57 hours of capture time during the weekend and an additional 9 hours during four week nights, this results in a total capture time of 93 hours. Not all of this energy needs to be stored, however, as some of it can be used directly when it is produced. Assuming the heat load is constant for the entire month, the hourly heat load average for the winter months is 2.0 GJ/hr. In order to produce all of the thermal energy required for the week during the 93 hours of capture time, this results in an hourly thermal energy production requirement of 3.6 GJ/hr. Not all of the thermal energy produced requires storage, however, as 2.0 GJ/hr can be used directly. The storage capacity requirement for the phase change material thermal storage system is therefore 1.6 GJ/hr for 57 hours, or 91 GJ. In order to store this 91 GJ of thermal energy from the distributed storage system, the mass and volume of each short listed PCM, calculated in step 10, is shown in table 6.4. Both the RT65 and stearic acid will undergo further calculations although the RT65 was expected to cost much more.

Table 6.4: Required PCM mass and cost to store 91 GJ of latent thermal energy.

Material	Melt Temperature	Heat of Fusion	Density (l)	Required Volume	Required Mass	Price	PCM Cost
	[C]	[kJ/kg]	[kg/m ³]	[m ³]	[kg]	[\$/kg]	[\$]
Stearic Acid	69	199	940	489	459347	\$1.30	\$597,151
RT65	64	152	780	771	601382	\$3.79	\$2,279,236

Because the DSS sizing was based on the thermal energy requirements of McMaster Innovation Park, no transportation of the thermal energy was required in this case. This means that step 11 did not impose any additional requirements on the system. It was prudent, however, to design the cells such that they can be installed using a standard lift truck and fit through standard sized equipment doors for ease of replacement. This also accommodates future needs if transportation becomes desirable. The next phase of the design was therefore the determination of the cell storage time, step 12.

6.6 – PCM Thermal Storage System Sizing Results

The model inputs for the cell storage time sizing of the DSS thermal energy storage system can be seen in tables 6.5 and 6.6 for the different PCMs. Due to the corrosive nature of the capture fluid, separate capture and recovery channels were required. Several different geometry iterations were performed, with the outputs for each simulation found in tables 6.7 and 6.8 along with the raw material costs for each configuration. For each simulation the capture channels were assumed to be stainless steel with a total thickness of 6.7 mm and a wall thickness of 1.6 mm. The recovery channels were made of aluminum with a total thickness of 4.6 mm and a wall thickness of 1 mm. Because the channels are of different metals, the effect of a galvanic charge between the channels should be evaluated in the phase change material to ensure that significant corrosion and contamination of the PCM do not occur. The commodity prices of stainless steel and aluminum are approximately \$3 and \$2 per kilogram respectively.

It can be seen from these results, plotted in figure 6.3 that the longer the charge time, the less material costs in the thermal storage system. This is balanced by the capture and recovery systems' need for constant heat flux to ensure the system temperature does not undergo large fluctuations.

Table 6.5: Common inputs for the thermal energy storage system for McMaster Innovation Park.

Function	Units	Capture Fluid	Capture Channel	PCM	Recovery Channel	Recovery Fluid
Material		Water	Stainless Steel	Stearic Acid	Aluminum	Air
Density	[kg/m ³]		8000	940	2719	1.225
Heat Capacity	[J/kgK]		500	2380	871	1006.43
Thermal Conductivity	[W/mK]		16.4	0.3	202.4	0.0242
Latent Heat of Fusion	[J/kg]			198800		
Freezing temperature	[K]			340.95		
Melt temperature	[K]			341.95		
Thickness	[m]		0.000508	Table 6.6	0.0015875	0.001778
Convective Coefficient	[W/m ² K]	100				
Bulk Temperature	[K]	353.15				
Initial Temperature	[K]		337.95	337.95	337.95	337.95

Table 6.6: Phase change material inputs for the thermal energy storage system.

Function	Units	PCM1	PCM2
Material		RT65	Stearic Acid
Density	[kg/m ³]	780	940
Heat Capacity	[J/kgK]	2200	2380
Thermal Conductivity	[W/mK]	0.2	0.3
Latent Heat of Fusion	[J/kg]	152000	198800
Freezing temperature	[K]	336	341
Melt temperature	[K]	337	342
Thickness	[m]	Table 6.7	Table 6.8
Initial Temperature	[K]	333	338

Table 6.7: Model outputs for the RT65 thermal energy storage system for several geometries.

PCM Thickness	Melt Time	PCM	SS	AL	PCM Cost	SS Cost	AL Cost	Cell Materials
[m]	[hr]	[%]	[%]	[%]	[\$]	[\$]	[\$]	[\$]
0.0075	0.5	78.2%	5.3%	16.5%	\$2,279,236.00	\$ 3,653,970	\$ 2,587,278	\$ 8,520,484
0.0113	1	84.4%	3.8%	11.9%	\$2,279,236.00	\$ 2,425,202	\$ 1,717,220	\$ 6,421,657
0.0167	2	88.9%	2.7%	8.4%	\$2,279,236.00	\$ 1,641,005	\$ 1,161,951	\$ 5,082,192
0.0208	3	90.8%	2.2%	6.9%	\$2,279,236.00	\$ 1,317,537	\$ 932,913	\$ 4,529,686
0.0243	4	92.1%	1.9%	6.0%	\$2,279,236.00	\$ 1,127,769	\$ 798,542	\$ 4,205,547
0.0216	5	91.1%	2.1%	6.7%	\$2,279,236.00	\$ 1,000,174	\$ 708,196	\$ 3,987,607
0.0302	6	93.5%	1.6%	4.9%	\$2,279,236.00	\$ 907,443	\$ 642,536	\$ 3,829,215
0.0327	7	94.0%	1.5%	4.6%	\$2,279,236.00	\$ 838,067	\$ 593,412	\$ 3,710,715
0.0351	8	94.4%	1.4%	4.3%	\$2,279,236.00	\$ 780,763	\$ 552,837	\$ 3,612,836

Table 6.8: Model outputs for the stearic acid thermal energy storage system for several geometries.

PCM Thickness	Melt Time	PCM	SS	AL	PCM Cost	SS Cost	AL Cost	Cell Materials
[m]	[hr]	[%]	[%]	[%]	[\$]	[\$]	[\$]	[\$]
0.0053	0.5	71.7%	6.9%	21.4%	\$ 597,151	\$ 1,119,892	\$ 792,965	\$ 2,510,009
0.0083	1	79.9%	4.9%	15.2%	\$ 597,151	\$ 714,368	\$ 505,824	\$ 1,817,343
0.0127	2	85.9%	3.4%	10.7%	\$ 597,151	\$ 468,015	\$ 331,389	\$ 1,396,554
0.0161	3	88.5%	2.8%	8.7%	\$ 597,151	\$ 369,363	\$ 261,536	\$ 1,228,050
0.0190	4	90.1%	2.4%	7.5%	\$ 597,151	\$ 312,911	\$ 221,564	\$ 1,131,626
0.0216	5	91.1%	2.1%	6.7%	\$ 597,151	\$ 276,081	\$ 195,485	\$ 1,068,717
0.0239	6	91.9%	2.0%	6.1%	\$ 597,151	\$ 249,386	\$ 176,583	\$ 1,023,120
0.0260	7	92.5%	1.8%	5.6%	\$ 597,151	\$ 229,059	\$ 162,191	\$ 988,401
0.0280	8	93.0%	1.7%	5.3%	\$ 597,151	\$ 212,856	\$ 150,717	\$ 960,724

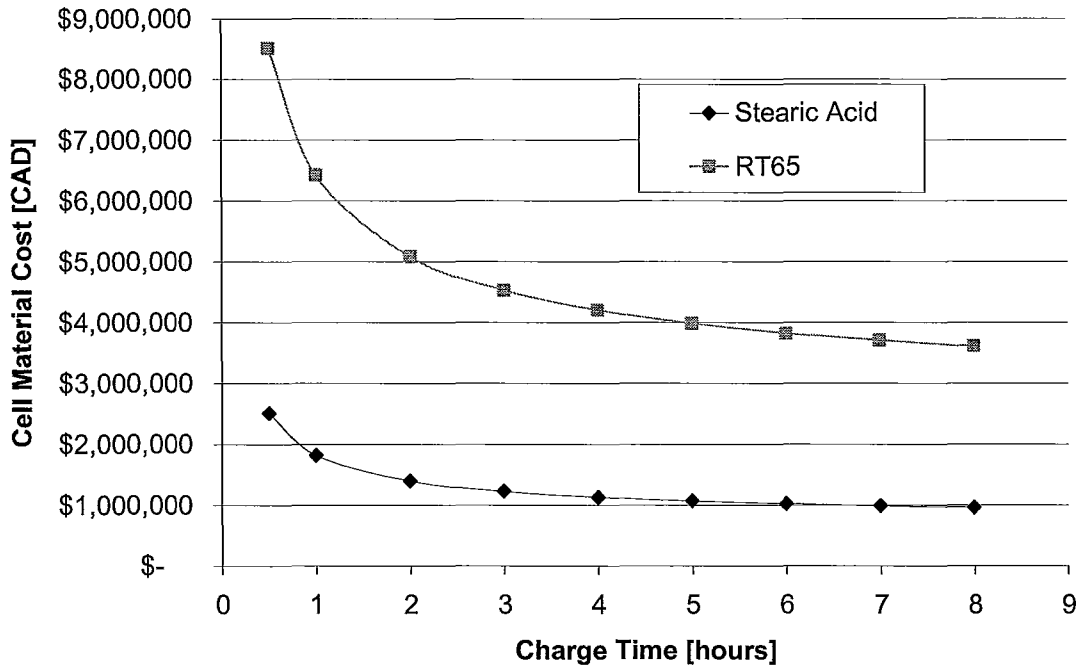


Figure 6.3: Cell material cost versus charge time for stearic acid and RT65 cells.

In the case of the DSS thermal battery with 91 GJ of storage and either 489 m³ of stearic acid or 771 m³ of RT65, the limitation was on physical cell size rather than thermal size, so the cell storage time can be as long as feasible based on the capture and recovery cycle timing. The shortest off-peak capture period (Ontario Energy Board 2009), as seen previously in table 6.1, was 10:00 pm to 7:00 am on weekdays, or 9 hours of storage. Conversely the recovery was required for the remaining 15 hours per day to meet heating needs in the winter months. Based on the material cost versus charge time curve and these capture and recovery times, a cell storage time of 6 hours was therefore chosen. This allows for some staggering of cell capture cycles to produce a more constant system heat flux, if necessary, while reducing the number of partially charged cells at the end of a cycle. These partially charged cells may cause atypical solidification

behaviour upon recovery or melt behaviour upon charging as the melt front may become significantly non-planar during the storage period due to potential dendritic growth of the solid.

Based on the cell material cost, the RT65 system was eliminated at this point and calculations continued only with stearic acid. The capture heat flux profile for the stearic acid 6-hour capture time cell with a PCM thickness of 23.9 mm can be seen in figure 6.4. The capture cycle heat flux profiles for cells staggered to start at 15 minute intervals is seen in figure 6.5. Figure 6.6 shows the recovery heat flux for the 6-hour capture time cell with an average bulk air temperature of 25 °C. The effect of an error of +/- 20% in cell charge time (4.8 to 7.2 hours) was also evaluated and shown to cause only a +/- 5% change in the cell material cost for the 6 hour cell. This percentage would, however, be larger for a cell with a shorter charge time.

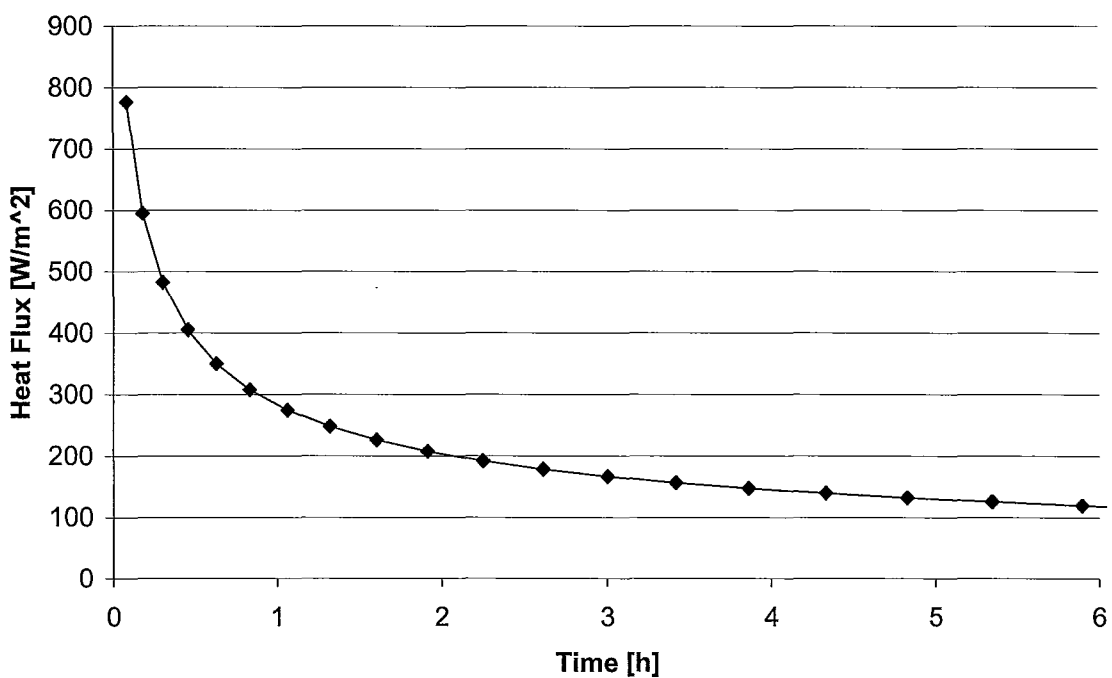


Figure 6.4: Capture cycle heat flux over time for 6-hour stearic acid capture cell.

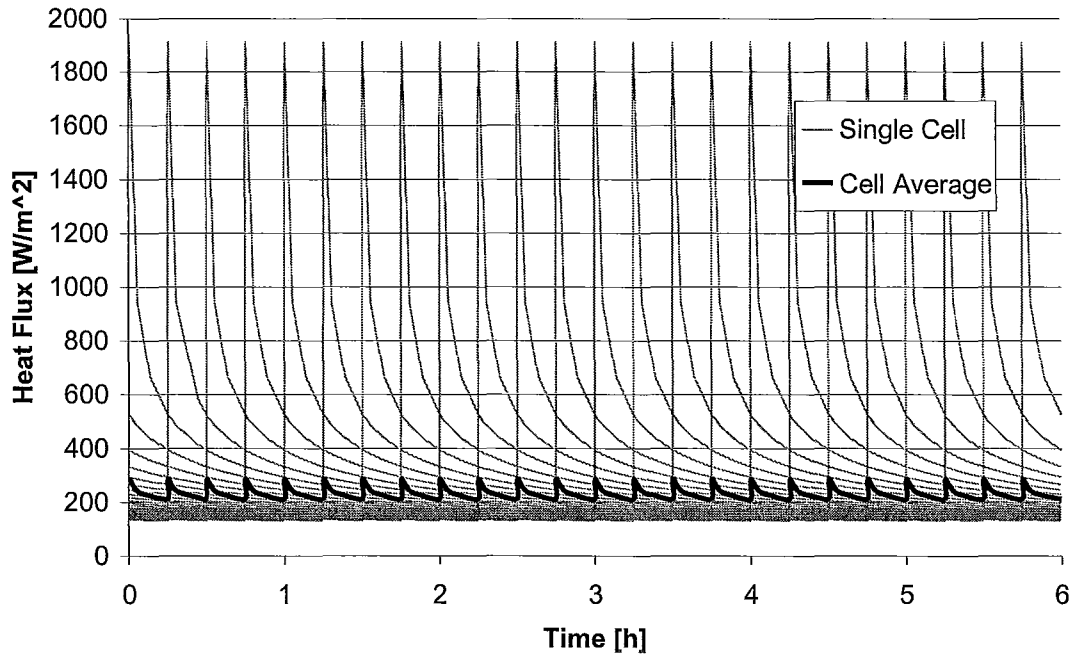


Figure 6.5: Net capture cycle heat flux using 6-hour stearic acid capture cells staggered at 15 minute intervals.

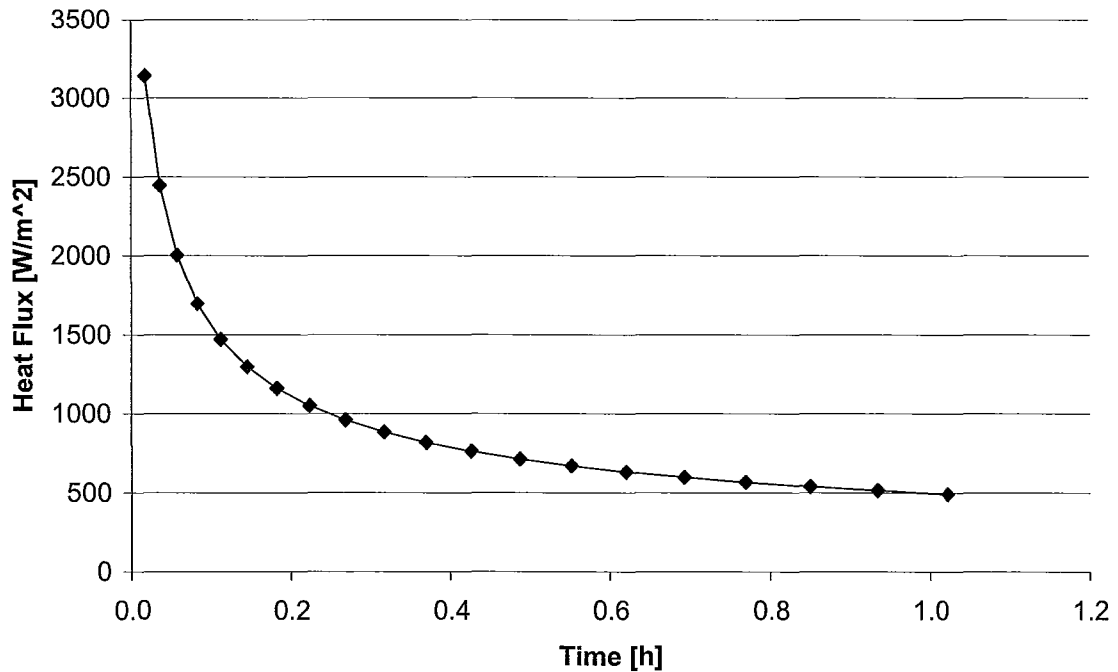


Figure 6.6: Recovery cycle heat flux over time for 6 hour stearic acid capture cell (1 hour recovery time) with an average bulk recovery fluid temperature of 25 °C.

6.7 – DSS System Sizing Results

Dependent on the volumetric restrictions for the distributed storage system and thermal battery, a decision was required on whether or not the hydrogen will be compressed before storage. The system volume and electrical requirements were determined for both cases in order to provide all the relevant information for this decision. The system designed without compression was denoted as system A with the system using a storage pressure of 400 bar denoted as system B. As noted in section 6.2, system A has a total electrical storage efficiency of 37% and system B 28%. The electrical output of the system is the portion of the total energy that is not thermal energy. The electrolysis efficiencies of 74% for system A and 55% for system B were based on Hydrogenics' (2009) HySTAT-A product literature and compression data from Praxair (2003). For the proposed system with 91 GJ of weekly thermal energy storage from electrolysis this resulted in a required hydrogen production of 880 Normalized_m³/h for system A and 660 Normalized_m³/h for system B each week. This would require 60 and 44 HySTAT-A cell stacks respectively (Hydrogenics, 2009). Given the cumulative winter on-peak electricity pricing time of 35 hours per week, and a generating efficiency of 50% of the higher heating value of hydrogen (Shudo, 2007), 1.77 kWh/Normalized_m³, the distributed storage systems would require generation sets of 4200 kW and 3200 kW for systems A and B respectively. With an average on-peak demand of 410 kW during the winter months (Sandwell Consulting, 2009) this resulted in at least 3790 kW or 2790 kW of excess energy that can be sold back to the grid, while completely eliminating the need to purchase electricity at on-peak prices. Also, the

thermal energy created by these generators can either be used to generate more electricity or can be sold on the thermal energy market due to its high availability.

The volume required for hydrogen storage was calculated from the longest storage time of 57 hours over the weekend. This means that a storage capacity 57 / 93, or 61% of the hydrogen gas must be available. System A, with a storage pressure of 25 bar would therefore require 2.7% of the normalized volume and system B, with a storage pressure of 400 bar would require 0.22% of the normalized volume calculated using the ideal gas law modified with a compressibility factor (Incropera & DeWitt, 2002). This results in a hydrogen storage capacity of 1360 m³ for system A and 82 m³ for system B, a 16-fold gas storage space advantage for the system with gas compression.

The volume required for the thermal storage system is the same for both systems A and B and is calculated by multiplying the required PCM volume by the volume ratio. This volume ratio is calculated by dividing the PCM thickness by the total cell thickness from the centre of the capture channel to the centre of the recovery channel and adding an additional 20% for insulation, fluid routing and structural materials. This volume ratio for the 6 hour capture cell is 1.48, resulting in a total thermal storage system volume of 730 m³. Summaries of both systems A and B are shown in table 6.9 for comparison.

Table 6.9: Summary of Distributed Storage Systems A and B, with and without storage compression.

Parameter	Units	System A	System B
Thermal Energy Storage	GJ	91	91
Cell Material Cost	CAD	\$1.02 M	\$1.02 M
Thermal Storage Cell Volume	m ³	730	730
Storage Pressure	Bar	25	400
Storage Efficiency	%	37%	28%
Electrolysis Efficiency	%	74%	55%
Weekly Hydrogen Production	Normalized m ³	25,000	19,000
H ₂ Generation Capacity	Normalized m ³ /h	440	330
HySTAT-A Cell Stacks		60	44
Generator Set Capacity	kW	4200	3200
Minimum Excess Capacity	kW	3790	2790
H ₂ Storage Capacity	m ³	1360	82

While adding a thermal storage system to the DSS does not change the thermodynamic efficiency of the round-trip storage efficiency, it does turn the thermal energy caused by the inefficiency in the electrolysis process into useful energy. For this reason, a new efficiency for the electrolysis process was defined that is based on the useful thermal energy not contributing to the component efficiency. Since all of the thermal energy from the electrolysis is used, the new efficiency of this component was therefore defined as 100%, increasing the round-trip storage efficiency by a factor of 1.36. This made the new average efficiencies for systems A and B 49.8% and 37.4% respectively for December to March, 47.5% and 35.7% for November to April and 42.8% and 32.1% for the entire year.

The total cost of the system requires specific quotes for additional system components such as hydrolysis units, gas storage cylinders, hydrogen internal combustion generator sets and associated electrical equipment. It was determined, however, that the thermal storage system will cost more than one million Canadian dollars. Given a

projected payback period of 30 years, one thirtieth of this cost is \$63,000. Since the potential natural gas savings from using a thermal storage system is 45% (the heating load not occurring during thermal energy production) of the \$44,000 spent on natural gas per year based on 2009 projections, additional sources of revenue from feed-in tariffs, carbon offset credits and oxygen sales would need to be realized to create an economically feasible system.

The carbon offsets realized from eliminating the need for natural gas heating at McMaster Innovation Park was calculated based on 5.32 metric tonnes of carbon dioxide per 1000 therms of natural gas combustion (Natural Gas, 2009). For the total 88,442 therms of natural gas used by MIP this results in a carbon dioxide savings of 470 tonnes. Since the average car produces approximately 4-5 tonnes of carbon dioxide per year (Moblu, 2009), this is an equivalent amount of carbon dioxide savings to taking more than 100 cars off the road.

CHAPTER 7 – Conclusions and Recommendations

7.1 – Analytical Model

An analytical model was developed in this study based on one-dimensional pseudo-steady heat transfer through a phase change material thermal storage cell with laminar capture and recovery flow and rectangular channels. This model is intended for use in preliminary consideration of thermal energy storage systems where detailed geometry and phase change material property information is not available and other two or three dimensional models can therefore not be used. This model was compared to test data and a three-dimensional CFD model without natural convection and found to have good agreement with both. The parametric behaviour was also compared to a two-dimensional CFD model without natural convection and found to match the trends. The model limitations that were tested in the parametric study are listed in table 7.1. In addition to these, table 7.2 presents additional limitations and recommendations. While further refinements to the model are both possible and advised, the model developed in this study can be used for preliminary sizing of thermal energy storage systems.

Table 7.1: Summary of successfully tested ranges for model input parameters.

Parameter	Units	Minimum	Maximum
PCM Latent Heat of Fusion	J/kg	91,400	219,360
PCM Thermal Conductivity	W/mK	0.1	100
PCM Heat Capacity	J/kgK	1075	2580
Capture/Recovery Fluid Thermal Conductivity	W/mK	0.01	10
Capture/Recovery Fluid Heat Capacity	J/kgK	100	5000
Capture/Recovery Fluid Convective Heat Transfer Coefficient*	W/m ² K	10	10,000
Capture/Recovery Flow Regime*		Laminar	Laminar
Capture/Recovery Channel Thermal Conductivity	W/mK	1	202
Capture/Recovery Channel Heat Capacity	J/kgK	100	5000
Capture/Recovery Temperature – Melt Temperature	°C	2	50
Initial Subcooling or Superheating	°C	1.05	20

*Note: the convective coefficient was tested for a much wider range of values than would be afforded for laminar flow, however the model is currently set up for laminar flow only.

Table 7.2: Additional model limitations and recommendations for use.

Parameter	Recommendation or Limitation
Geometry	Rectangular Channels
Capture/Recovery Temperature to Melt Temperature Difference	No less than 5 °C
Phase Change Material Melting Temperature to Solidification Temperature Difference	Less than 1 °C – any more than this should be verified experimentally
Channel Orientation	Vertical – to ensure trapped gas bubbles do not hinder heat transfer
Channel Thickness	Less than 40 mm – larger geometries should be verified experimentally

7.2 – Further Model Development and Validation

Further evaluation of the assumptions used in the analytical model should be performed based on realistic thermal battery geometries. In order to determine a reasonable range of phase change material thicknesses, several more systems should be sized based on a wide range of thermal storage applications. This range of thicknesses, combined with engineering estimates of reasonable cell heights and widths, will then provide a range of geometries and boundary conditions that should be investigated to assess natural convection and linearity of temperature profiles in the liquid phase change material. Quantifying the effect of natural convection, discussed later in section 7.4, and

non-linear temperature profiles using either CFD or equations from the literature will then indicate whether or not these assumptions should be eliminated from the model or modified to more accurately represent the behavior of real thermal energy storage systems.

7.3 – PCM Effective Thermal Conductivity Enhancement

A comprehensive literature review on effective thermal conductivity enhancements should be performed with specific focus on the effect of overall system size and cost. Additional investigation into other methods of heat transfer enhancement, such as maximizing natural convection cells in the liquid phase through optimized geometric design or utilizing electrohydrodynamics to increase velocities in the liquid phase would also aid in decreasing the capture and recovery time for a given thickness. Enhanced heat transfer structures, such as fins, within the PCM can also be investigated as they will aid in both the capture and recovery processes. All enhancements, however, should be evaluated based on the effect they have on overall system cost and size.

7.4 – Convective Heat Transfer in Liquid PCM

Even without any enhancements, convective heat transfer cells will form in the liquid phase change material. This is highly dependent on the detailed geometry of the cells and therefore difficult to predict in the preliminary feasibility study.

Experimentation should therefore be done on any expected geometries not in the literature to try to determine the effect of convective cells on the effective thermal conductivity in the phase change material. In this way, estimates of this effect can be

applied to the model to improve the accuracy of the system sizing. The use of effective thermal conductivity in estimating convective heat transfer cells can also be evaluated and a modified analytical model created if it is found deficient.

7.5 – PCM Properties Library

One of the major hurdles facing phase change material thermal battery design is a lack of readily available material property information. Creation of a phase change material properties database including freezing temperature, melt temperature, density versus temperature equations, latent heat of fusion, heat capacity, liquid thermal conductivity, solid thermal conductivity, liquid viscosity and thermal cycling stability would allow designers to evaluate a wider range of phase change materials. This would also enable automatic phase change material selection via sizing software, greatly reducing the time required for a designer to evaluate the benefits of a thermal storage system.

7.5.1 – Thermal Conductivity Testing

While methods exist for measuring thermal conductivity of solids accurately, the phase change material database requires thermal conductivity near the melting and freezing temperatures. This necessitates test methods capable of measuring thermal conductivity in both solids and liquids. Many solid materials also exhibit anisotropic thermal conductivity behaviour, and testing of a single sample in more than one direction is also desirable. Methods must therefore be developed for testing the thermal

conductivity of both liquid and solid phase change materials near their phase change temperature.

7.5.2 – Thermal Cycling Stability Testing

While some thermal cycling stability testing has been done in the past, it has usually been for less than 1000 cycles. Considering the service life requirements for a large-scale thermal storage system, the number of cycles should be increased to more accurately reflect the actual number of cycles a system would undergo in 30 years. This would change based on the capture and recovery cycle, but is approximately 11,000, assuming one full cycle per day.

7.6 – H₂Green Distributed Storage System

While the H₂Green distributed storage system for McMaster Innovation Park is technically feasible, further information is needed to determine economic feasibility. Since energy storage systems that shift the load on the electrical grid from on-peak to off-peak times are not currently included in Ontario's Feed-In Tariff program, a contract would have to be negotiated to determine the price paid for the electricity provided to the grid at on-peak times. Pricing for oxygen sales would also have to be negotiated with a potential buyer based on the quantity, pressure and purity of oxygen produced by the electrolysis units. The potential for carbon offset credits should also be explored and a better estimate of material costs based on actual quotations could also be obtained now with known quantities and preliminary geometries.

REFERENCES

- Bush, Rick and Wolf, Gene. "Utilities Load Shift With Thermal Storage".
tdworld.com/substations/thermal-storage-utilities-load-20090801/index.html,
Transmission and Distribution World, Penton Media Inc. Web. 19 Oct. 2009.
- Carlsaw, H.S. and Jaeger J.C. Conduction of Heat in Solids, 2nd Ed. Oxford University
Press, New York (1964).
- Cole Parmer - RK-07012-20 Miniature Gear Pump Specifications.
http://www.coleparmer.ca/catalog/product_view.asp?sku=0701220&px=RK. Web.
22 Nov. 2009.
- Domanski, R., Rebow, M., Nagano, K. and Gorczak, D. Investigation of Free
Convection in Melting Zone During the Solidification and Melting of PCMs. IEA, ECES
IA Annex 10, Phase Change Materials and Chemical Reactions for Thermal Energy
Storage 6th Workshop Stockholm, Sweden (2000).
- Dow Chemicals – Caustic Soda Product Information, [http://www.dow.com/
PublishedLiterature/dh_0048/0901b80380048f1a.pdf?filepath=causticsoda/pdfs/noreg/10
2-00417.pdf&fromPage=GetDoc](http://www.dow.com/PublishedLiterature/dh_0048/0901b80380048f1a.pdf?filepath=causticsoda/pdfs/noreg/102-00417.pdf&fromPage=GetDoc). Web. 18 Nov. 2009.
- Drage, Graham. "Phase Change Material Used In Temperature Controlled Packaging &
Transport". A1 Articles (2009). http://www.a1articles.com/article_978704_53.html.
Web. 25 Oct. 2009.
- Engineered Systems. "Thermal Storage Finds Cool Results In Midwestern Cities".
[www.esmagazine.com/Articles/Case_In_Point/a195e38468ba8010VgnVCM100000f932
a8c0___](http://www.esmagazine.com/Articles/Case_In_Point/a195e38468ba8010VgnVCM100000f932a8c0___), BNP Media. Web. 24 Oct. 2009.
- Glacier Tek – RPCM Coolvest, www.glaciertek.com. Web. 19 Oct. 2009.
- Hummel Croton Inc. – Stearic Acid MSDS –
www.hummelcroton.com/msds/steara_m.gtml. Web. 14 Dec. 2009.
- Hydrogenics - HySTAT-A Energy Station product literature, [http://www.hydrogenics
.com/onsite/pdf/HySTAT-A%20Energy%20Station_web.pdf](http://www.hydrogenics.com/onsite/pdf/HySTAT-A%20Energy%20Station_web.pdf), accessed Jan 23, 2009.
- Incropera, F.P., DeWitt, D.P. Fundamentals of Heat and Mass Transfer, 5th Ed. John
Wiley and Sons, New York (2002).
- Intertec – DD830-0e Safe Link with Passive PCM Cooling System. www.intertec.info.
Web. 25 Oct. 2009.

Kays, W.M. and Perkins, H.C. in Rohsenow, W.M., Harnett, J.P. and Fanic, E.N. Handbook of Heat Transfer Fundamentals, Chapter 7, McGraw-Hill, New York, 1985 (1972).

Kenisarin, M. and Mahkamov, K. Solar energy storage using phase change materials, Renewable Sustainable Energy Review 11 (9) (2007), pp. 1913-1965.

Khudhair, A. and Farid, M. A review on energy conservation in building applications with thermal storage by latent heat using phase change materials. Energy Conversion and Management 45 (2004), pp.263-275.

Kline, S.J. and McClintock, F.A. Describing Uncertainties in Single-Sample Experiments. Mechanical Engineering 73 Jan (1953). pp. 3-9.

Makrolon – Makrolon 2405 Datasheet. <http://www.bayermaterialsciencenafta.com/resources/d/document.cfm?Mode=view&f=13F00037-E0C4-6D2A-E45AA7C274ABEA9F&d=14A728A5-EDFB-DE18-1B841BB81F34D6D5>, Bayer Material Science LLC, 2007. Web. 27 Oct. 2009.

MacCracken, M., “Energy Storage: A Critical Path to Sustainability”. CALMAC Manufacturing Corporation - Lessons Learned, 6 (2009), pp 49-50. Web. 13 Dec. 2009, http://www.calmac.com/documents/EnergyStorage_ACriticalPathToSustainability_LessonsLearned2009.pdf

Mills, A., Farid, M., Selman, J. and El-Hallaj, S. Thermal conductivity enhancement of phase change materials using a graphite matrix. Applied Thermal Engineering 26 (2006), pp. 1652-1661.

Moblu – Frequently Asked Questions - How much CO₂ does an average car produce in a year?, <http://www.moblu.ca/faq#4>, 18 Dec. 2009.

Nagano, K., Mochida, T., Iwata, K., Hiroyoshi, H. and Domanski, R. Thermal Performance of Mn(NO₃)₂•6H₂O as a New PCM for Cooling System. IEA, ECES IA Annex 10, Phase Change Materials and Chemical Reactions for Thermal Energy Storage 6th Workshop Stockholm, Sweden (2000).

National Instruments - NI-9213 16-Channel Thermocouple Module Data Sheet. <http://sine.ni.com/ds/app/doc/p/id/ds-69/lang/en>. Web. 22 Nov, 2009.

Natural Gas – Environment and Technology Data - <http://www.naturalgas.org/environment/naturalgas.asp>. Web. 18 Dec. 2009

Neslabs - Endocal RTE-Series Refrigerated Bath/Circulator Instruction and Operation Manual. NESLAB Manual P/N 013853 Rev. 03/22/93, (1993).

Omega - HFS-3, HFS-4 Thin Film Flux Sensors User's Guide. M1844/1105 (2005).

Omega - FP-5060 Series Micro-Flow Sensors User's Guide. M-2579/0307 (2007).

Omega - ANSI and IEC Colour Codes and Thermocouple Tolerances.
http://www.omega.com/temperature/pdf/tc_colorcodes.pdf. Web. 22 Nov 2009.

Ontario Energy Board – Electricity Prices in Ontario,
<http://www.oeb.gov.on.ca/OEB/For+Consumers/Understanding+Your+Bill+Rates+and+Prices/Electricity+Prices+in+Ontario>. Web. 23 Jan. 2009.

Praxair - “Hydrogen Delivery, Liquefaction and Compression”,
http://www1.eere.energy.gov/hydrogenandfuelcells/pdfs/liquefaction_comp_pres_praxair.pdf, presentation delivered to Strategic Initiatives for Hydrogen Delivery Workshop, May (2003). Web. 12 Jan. 2009.

Rubitherm – RT Latent Heat Materials Product Information http://www.rubitherm.com/english/pages/02a_latent_heat_paraffins.htm. Web. 18 Nov. 2009.

Salton, Jeff. “Phase Change Materials for the Perfect Cup of Coffee”.
www.gizmag.com/phase-change-cup-coffee/12596/, Mike Hanlon Publisher. Web. 19 Oct. 2009.

Sandwell Consulting - Internal Document, “MIP- 182923 BLOCK LOAD”, calculated at 02:26 PM on 09/11/2008.

Sari, A. Form-stable paraffin/high density polyethylene composites as solid–liquid phase change material for thermal energy storage: preparation and thermal properties. *Energy Conversion and Management* 45 (2004), pp. 2033-2042.

Sari, A. Eutectic mixtures of some fatty acids for latent heat storage: Thermal properties and thermal reliability with respect to thermal cycling. *Energy Conversion and Management* 47 (2006), pp. 1207-1221.

Sari, A. and Karaipekli, A. Thermal conductivity and latent heat thermal energy storage characteristics of paraffin/expanded graphite composite as phase change material. *Applied Thermal Engineering* 27 issues 8-9 (2007) pp.1271-1277.

Seebeck, T.J., *Magnetische Polarisation der Metalle und Erze durch Temperaturdifferenz. Abhandlungen Deutsch Academie der Wissenschaften zu Berlin, Engelmann, Leipzig* (1895) written 1822-1823, 265-373.

Shah, R.K. and London, A.L. Laminar Flow Forced Convection in Ducts. Academic Press, New York, (1978).

Shudo, T. Improving thermal efficiency by reducing cooling losses in hydrogen combustion engines. International Journal of Hydrogen Energy 32 (2007) 4285-4293.

Sigma-Aldrich – Stearic Acid Product Search – www.sigmaaldrich.com/canada-english.html. Web. 14 Dec. 2009.

Soda-Fabrik & Société Badische Anilin - Brevet D'Invention: Procédé pour la production d'ammoniaque a partir de ses éléments. République Française - Office National de la Propriété Industrielle (1910).

Solar Millenium – The Parabolic Trough Power Plants Andasol 1 to 3 www.solarmillennium.de/upload/Download/Technologie/eng/Andasol1-3engl.pdf, Solar Millenium AG (2008). Web. 25 Oct. 2009.

Solvay Chemicals – Caustic Soda Information Sheet, http://www.solvaycausticsoda.com/docroot/caustic/static_files/attachments/pch_1110_0007_w_en_ww_.pdf. Web. 18 Nov. 2009.

Starfrit – Electronic Kitchen Scale 93018 – www.starfrit.com/Products/kitchen/Gadgets/Kitchen%20Scales/93018.aspx?sc_lang=en-CA. Web. 13 Dec. 2009.

Verma, P., Varun and Singal, S. Review of mathematical modeling on latent heat thermal energy storage systems using phase-change material. Renewable and Sustainable Energy Reviews12 (2008), pp. 999-1031.

Williams, Marie. Chicago District Cooling Plant Exceeds Expectations. The Official Newsletter of International District Energy Association 14 (2) (1998), p 8. Web. 24 Oct. 2009.

Xiao, M., Feng, B. and Gong, K. Preparation and performance of shape stabilized phase change thermal storage materials with high thermal conductivity. Energy Conversion and Management 43 (2002), pp. 103-108.

Zalba, B; Marin, J; Cabeza, L; Mehling, H. Review on thermal energy storage with phase change: materials, heat transfer analysis and applications, Applied Thermal Engineering 23 (2003) pp. 251-283.

APPENDIX A – EXPERIMENTAL APPARATUS DESIGN DETAILS

A.1 – PCM Chamber

The PCM chambers were made to order by P&A Plastics at 150 Main St. E. in Hamilton, Ontario at a cost of approximately 82 Canadian dollars per unit. The material used was Makrolon polycarbonate from Bayer Material Science. Dimensions of the PCM chamber can be found in figure A.1. The properties of Makrolon can be found in the product data sheet in table A.1 (Makrolon, 2009).

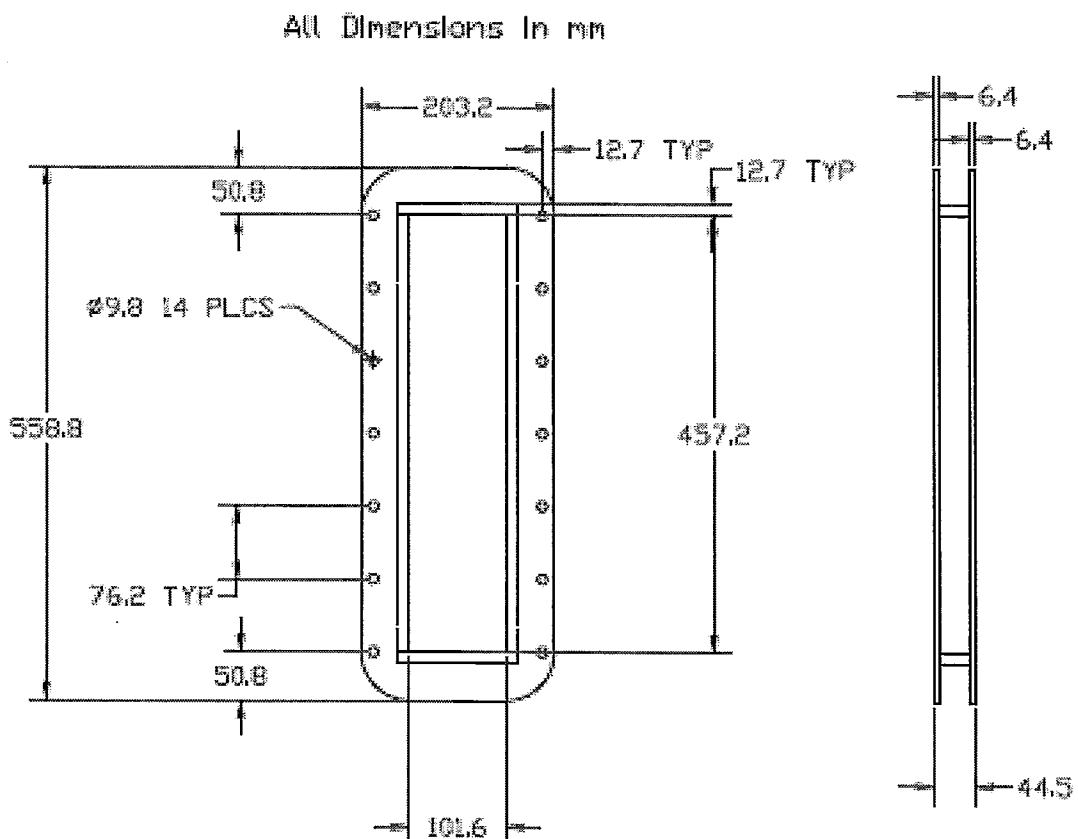


Figure A.1: PCM chamber dimensions.

Table A.1: General and thermal properties of Makrolon polycarbonate (Makrolon, 2009).

Typical Properties* for Natural Resin	ASTM Test Method (Other)	Makrolon® 2405/2407/2456 Resins	
		U.S. Conventional	SI Metric
General			
Specific Gravity	D 792		1.20
Density	D 792	0.043 lb/in ³	1.20 g/cm ³
Specific Volume	D 792	23.1 in ³ /lb	0.83 cm ³ /g
Mold Shrinkage	D 955	0.005–0.007 in/in	0.005–0.007 mm/mm
Water Absorption, Immersion at 73°F (23°C): 24 Hours	D 570		0.12%
Equilibrium			0.30%
Melt Flow Rate ^a at 300°C/1.2-kg Load	D 1238		20 g/10 min
Thermal			
Deflection Temperature, Unannealed: 0.250-in (6.4-mm) Thickness 264-psi (1.82-MPa) Load	D 648	259°F	126°C
66-psi (0.46-MPa) Load		273°F	134°C
Coefficient of Linear Thermal Expansion	D 696	3.34 E-05 in/in/°F	6.0 E-05 mm/mm/°C
Thermal Conductivity	C 177	1.39 Btu-in/(h-ft ² -°F)	0.20 W/(m-K)
Specific Heat	D 2766	0.28 Btu/(lb-°F)	1,172 J/(kg-K)
Relative Temperature Index: 0.059-in (1.5-mm) Thickness	(UL746B)		125°C
Electrical			115°C
Mechanical with Impact			125°C
Mechanical without Impact			
Vicat Softening Temperature, 50 N, 50°C/h	D 1525	291°F	144°C

A.2 – Capture/Recovery Flow Channel

The capture/recovery flow channel was fabricated in-house from 6061 aluminum sheet 1/8” thick and a rectangular aluminum channel 4” x 2” x 0.120” thick, cut in half and tack-welded to the 24” x 8” sheet. The edges were later sealed with silicone caulking to prevent leaks. The ends of the channel were capped with 0.120” aluminum plate and fittings attached using welded on 1” thick custom-made bosses threaded to fit a 1/4” NPT fitting. Detailed drawings of the Capture/Recovery flow channel can be seen in figures A.2 and A.3.

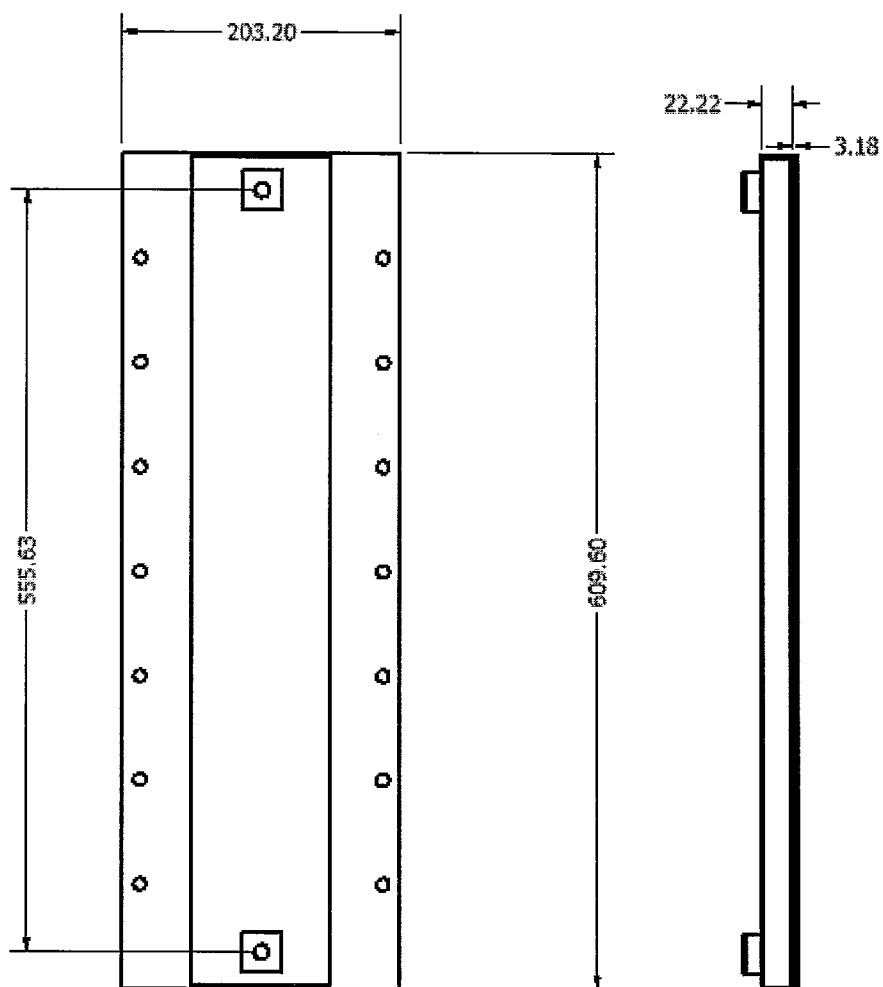


Figure A.2: Capture/recovery flow channel external dimensions in millimetres.

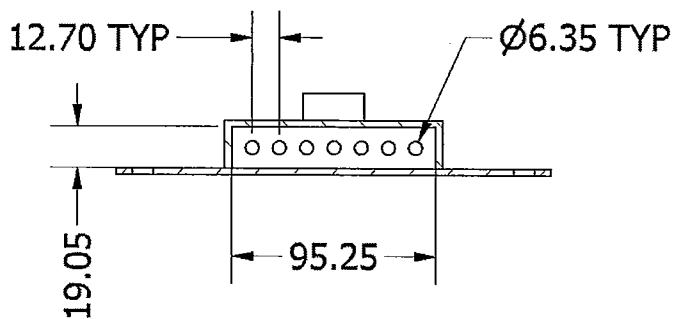


Figure A.3: Capture/recovery flow channel internal dimensions in millimetres.

A.3 – Refrigerated Bath

The temperature controlled bath used to set the capture/recovery fluid temperature is a Neslabs RTE 110 Refrigerated bath from ThermoFisher Scientific. Due to a malfunction in the unit, it was not possible to use the internal circulation pump to provide flow through the test loop, and an external pump was therefore required. The specifications for this bath can be seen in tables A.2 and A.3.

Table A.2: Temperature specifications for the Neslabs RTE 110 refrigerated bath (Neslabs, 1993).

	RTE-110	RTE-210
Temperature Range		
<i>Basic controller</i>	-25°C to +100°C	-24°C to +100°C
<i>Analog controller</i>	-25°C to +100°C	-24°C to +100°C
<i>Digital controller</i>	-30°C to +130°C	-28°C to +130°C
<i>Programmable controller</i>	-30°C to +130°C	-28°C to +130°C
Temperature Stability^{1,2}		±0.1°C
Temperature Stability^{1,3}		±0.01°C
Cooling Capacity^{1,4}	>500 watts at +20°C >300 watts at 0°C >175 watts at -10°C	>475 watts at +20°C >300 watts at 0°C >150 watts at -10°C

Table A.3: Physical specifications for the Neslabs RTE 110 refrigerated bath (Neslabs, 1993).

	RTE-110	RTE-210
Heater⁶ (Watts) Main Boost	800 NA	
Bath Work Area (H x W x D) Inches Centimeters	5 x 5 x 5.75 12.7 x 12.7 x 14.6	10 x 10 x 5.75 25.4 x 25.4 x 14.6
Bath Volume Gallons Liters	1.3 5.0	3.2 12.3
Unit Dimensions⁶ (H x W x D) Inches Centimeters	20 x 8.785 x 12.375 49.8 x 22.5 x 31.4	20 x 12.375 x 17.25 49.8 x 31.4 x 43.8
Unit Dimensions⁷ (H x W x D) Inches Centimeters	25 x 8.785 x 12.375 63.5 x 22.5 x 31.4	25 x 12.375 x 17.25 63.5 x 31.4 x 43.8
Shipping Weight Pounds Kilograms	70 32	90 41

A.4 – Pump

The pump used to circulate the water through the test loop is the RK-07012-20 miniature gear pump from Cole Parmer, manufactured by Greylor Company. Pump specifications can be found on the supplier’s website, www.coleparmer.ca, and are reproduced in table A.4.

Table A.4: Pump specifications for the RK-07012-20 miniature gear pump (Cole Parmer, 2009).

Wetted parts		DELRIN [®] plastic, 304 stainless steel, Buna N, and PTFE [®] PTFE
Max pressure		21 psi
Max temperature		200°F (93° C)
Max flow rate	Liters/min	2.52
	GPM	0.67
Port size		3/16" hose barb
Particulates		no
Run dry		no
Relief valve		no
Suction lift	dry	4"
	wet	10 ft
Duty cycle		continuous
Viscosity		200 cp max
Motor	Amps	2.0
Power cord		8" cord, no plug
Power	VDC	12
Dimensions		4"Lx1-3/4"Wx2-5/8"H

A.5 – Flow Meter

The flow meter used in the test apparatus is an Omega FP-5062 Micro-Flow Sensor. The calibration parameters and flow range for this sensor are seen in table A.5 and the wiring diagram in figure A.4. The recommended 10 kΩ pull-up resistor was replaced with a smaller 2 kΩ resistor due to the resistance of the data acquisition system. Line voltage was supplied via a 24 V, 0.75 A power supply. Pressure drop across the flow meter, physical dimensions and other specifications are seen in figures A.5 through A.7.

Table A.5: Flow meter calibration constants for the FP-5062 Micro-Flow Sensor (Omega, 2007).

Model	Pulses per U.S. Gal	Pulses per Litre	Pulses per mL	Flow Range	Pulse Range
	1/Gal	1/L	1/mL	L/min	Hz
FP-5062	9950	2629	2.629	0.11 - 2.6	5-114

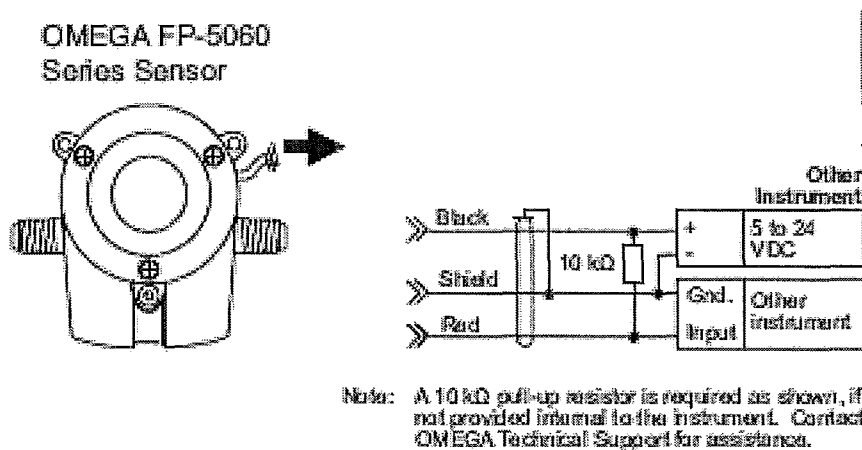


Figure A.4: Wiring diagram for the FP-5062 Micro-Flow Sensor (Omega, 2007a).

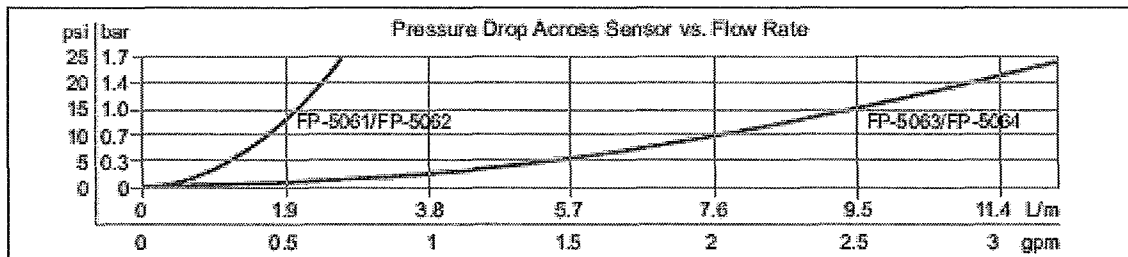


Figure A.5: Pressure drop across the FP-5062 Micro-Flow Sensor (Omega, 2007).

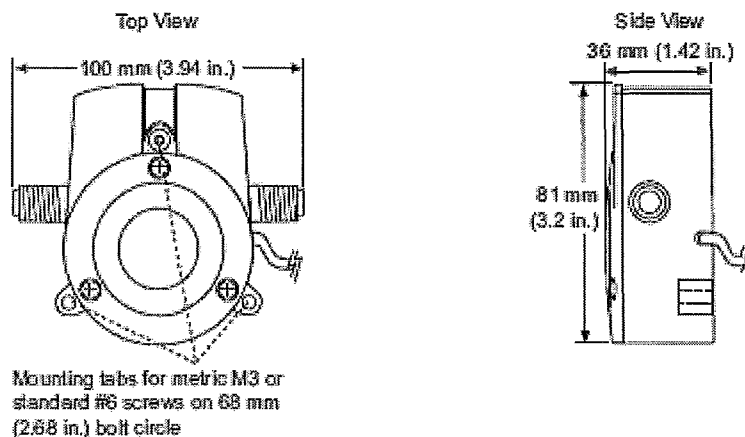


Figure A.6: Dimensions of the FP-5062 Micro-Flow Sensor (Omega, 2007).

Linearity: ±1.2% of full range	Quality Standard
Repeatability: ±0.5% of full range	• Manufactured under ISO 9001 and ISO 14001
Connections: 1/4 in. NPT (male) or ISO 7/1 - R1/4 (male)	
Cable length: 9 m (25 ft.), can splice up to 300 m (1000 ft.) max.	
Cable type: 2-conductor twisted pair w/shield (Belden 8451)	
Weight: 250 g (9.6 oz.)	
Wetted Materials	Fluid Conditions
• Sensor body and cover: 40% glass filled Polyphenylene Sulfide	Max. pressure/temperature:
•Rotor: PEEK, natural, unfilled	0 to 80°C (32 to 176°F) @ 5.5 bar (80 ps) max
•Rotor O-ring: Viton®	
•Cover O-ring: Viton®	

Figure A.7: Specifications of the FP-5062 Micro-Flow Sensor (Omega, 2007).

A.6 – Thermocouples

Thermocouples were ordered from Omega Canada under part number TMQSS-062E-12. These are 1/16 inch diameter, 12 inch long, stainless steel sheath, exposed-junction, T-type thermocouples with miniature quick connect connectors. The T-Type thermocouple range is -270 °C to 400 °C and the EMF over the full range is -8.05 mV to 69.553 mV (Omega, 2009). The published tolerance of these thermocouples is 0.5 °C or 0.4% above 0 °C and 1 °C or 1.5 % below 0 °C (Omega, 2009).

A.7 – Heat Flux Sensors

The heat flux sensors attached to the capture/recovery flow channel are Omega HFS-4 Thin Film Flux Sensors. The construction of these sensors is seen in figure A.8 and consists of several thermocouple junctions separated by thin layers of material with known thermal properties. The dimensions of the sensors are found in figure A.9 and placement of the sensors on the capture/recovery flow channel is seen in figure A.10. The electrical properties of the heat flux sensors are found in table A.6.

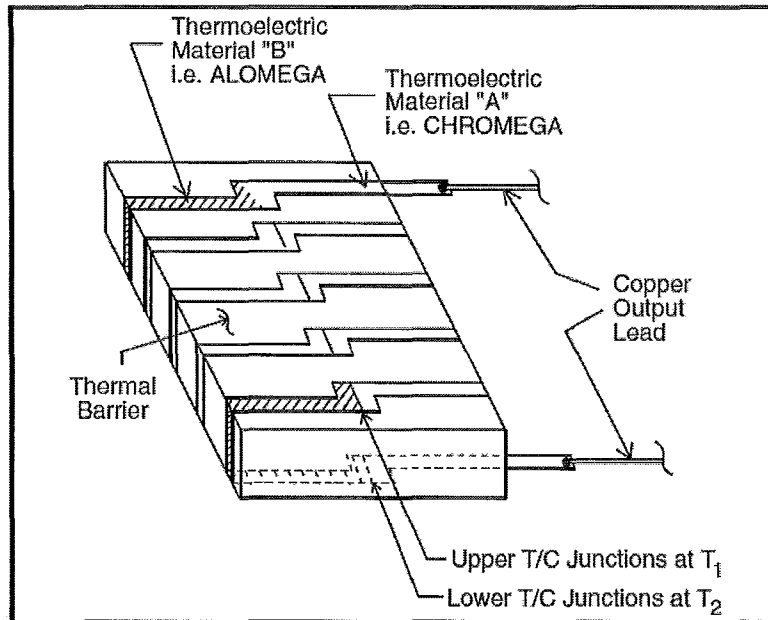


Figure A.8: Layered construction of the HFS-4 heat flux sensors (Omega, 2005).

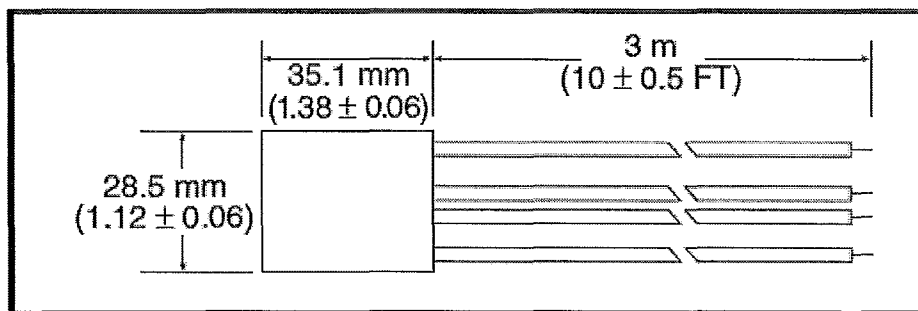


Figure A.9: Dimensions of the HFS-4 heat flux sensors (Omega, 2005).

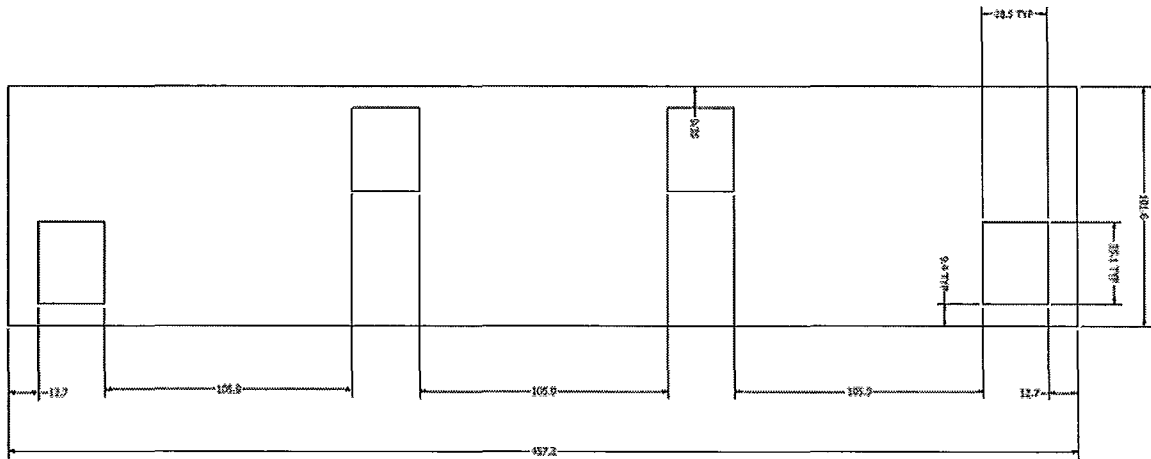


Figure A.10: Position (mm) of the heat flux sensors on the capture/recovery channel surface.

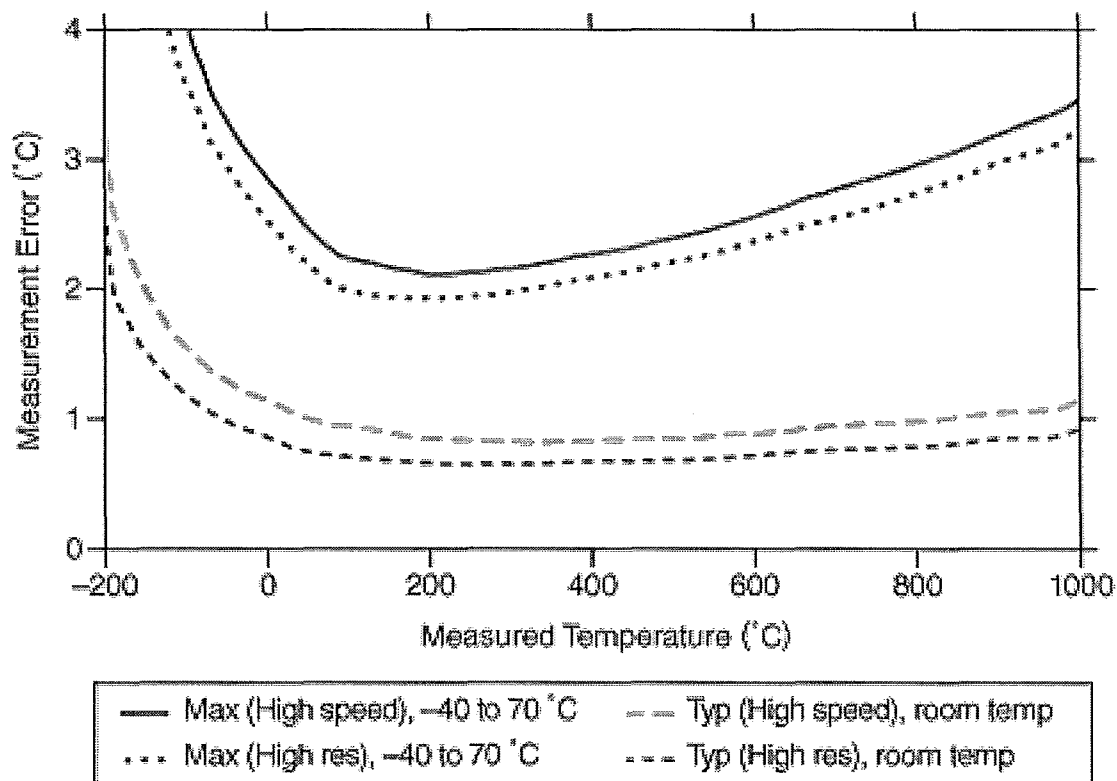
Table A.6: Electrical properties and responses of the HFS-4 heat flux sensors (Omega, 2005).

Property	Unit	Value
Nominal Sensitivity	$\mu\text{V}/(\text{BTU}/\text{ft}^2\text{Hr})$	6.5
	$\mu\text{V}/\text{W}/\text{m}^2$	21
Maximum Heat Flux	$\text{BTU}/\text{ft}^2\text{Hr}$	30,000
	W/m^2	9000
Response	s	0.13
Thermal Capacitance	$\text{BTU}/\text{ft}^2\text{°F}$	0.01
	$\text{W}/\text{m}^2\text{K}$	0.006
Thermal Resistance	$\text{°F}/\text{BTU}/\text{ft}^2\text{Hr}$	0.01
	$\text{K}/\text{W}/\text{m}^2$	0.02
Nominal Thickness	inches	0.007
	mm	0.2

A.8 – DAQ

Data acquisition for the experimentation used the National Instruments cDAQ-9172 unit. This is a modular system with up to 8 data acquisition cards docking in a hub that sends the data to a computer via a USB connection. Three data acquisition cards were used for testing: the NI-9213 (16 channel thermocouple), the NI-9211

(8 channels 80mV or thermocouple) and the NI-9421 (8 channel digital input). The quoted sensitivity for the acquisition of T-type thermocouple data from the NI-9213 card is $<0.02\text{ }^{\circ}\text{C}$ with the cumulative error shown in figure A.8.1 (not including the thermocouple instrument error). The error is further broken down into its component parts in the product literature (National Instruments, 2009).



This figure accounts for gain errors, offset errors, differential and integral nonlinearity, quantization errors, noise errors, $50\ \Omega$ lead wire resistance, and cold-junction compensation errors. The figure does not account for the accuracy of the thermocouple itself.

Figure A.11: Type T thermocouple data acquisition error for the NI-9213 module.

APPENDIX B – Experimental Procedure

B.1 – Cell Assembly

1. Place a bead of 100% Silicone sealant on either side of one of the nitrile gaskets
2. Quickly place the gasket between the polycarbonate flanged chamber and the polycarbonate backing plate before the silicone begins to dry
3. Insert longer bolts into the 14 holes from the backing plate side, with a washer on either side
4. Attach nuts to “finger-tight”
5. Tighten bolt assemblies, starting with opposite corners then proceeding to the middle bolts on each side
6. Tighten remaining bolts in any order
7. Insert thermocouple positioning baffle, ensuring that it is oriented in such a way that none of the holes are in the backing plate slot
8. Insert thermocouples into appropriate holes in the positioning baffle and record the position of each numbered thermocouple
9. Place a bead of 100% Silicone sealant on either side of the remaining nitrile gasket
10. Quickly place the gasket between the capture/recovery flow channel and the polycarbonate backing plate before the silicone begins to dry

11. Insert shorter bolts into the 14 holes from the flow channel side, with a washer on either side
12. Attach nuts to “finger-tight”
13. Tighten bolt assemblies, starting with opposite corners then proceeding to the middle bolts on each side
14. Tighten remaining bolts in any order
15. Allow silicone to cure for 24 hours (this can be done concurrently with the instructions in section D.2)

B.2 – Plumbing and Sensor Connections

1. Ensure all hoses are securely attached between the water bath, pump, flow meter, inlet quick disconnect fitting
2. Insure all hoses are securely attached between outlet quick disconnect fitting and water bath
3. Attach quick connect fittings to capture/recovery flow channel in desired orientation (“INLET” is labelled on the baffled end with “OUTLET” on the non-baffled end)
4. Attach thermocouple leads to data acquisition card and record which thermocouple corresponds to each channel
5. Attach flow meter leads to data acquisition card and plug in power supply
6. Attach heat flux sensor leads (and thermocouple leads, if desired) to data acquisition card and record which heat flux sensor corresponds to each channel

7. Plug in data acquisition card power supply
8. Attach USB connection from data acquisition card to computer

B.3 – Addition of PCM

1. Heat 2 litres of phase change material in glass containers with a pour spout in a furnace set at 70 °C until fully liquid
2. Set test cell upright with fill plugs removed and holes at the top
3. Insert glass funnels into fill holes
4. Weigh phase change material containers and funnels
5. Pour liquid phase change materials into funnels, ensuring both sides are filling evenly
6. Fill to just below the top of the phase change material chamber
7. Return excess liquid phase change material to the furnace
8. Allow phase change material to cool until fully solidified
9. Top up remaining space in phase change material chamber, ensuring no air is trapped
10. Quickly replace plugs into fill holes while the phase change material is still liquid
11. Weigh phase change material containers and funnels
12. Allow phase change material to fully solidify
13. Remove any spilled material and weigh

14. Subtract original mass of phase change material containers and funnels from final mass and spilled material to determine the mass of phase change material in the test apparatus

B.4 – Cell Warm-Up

1. Turn on data acquisition unit and start LabView program PCM01.vi to display and record data
2. Ensure correct calibration coefficients are input in LabView program
3. Fill water bath to just below the upper slit and replace lid to minimize evaporation
4. Turn on water bath and set temperature to 1.5 °C above desired initial cell temperature
5. Ensure throttling valve is fully open
6. Plug in pump
7. Tilt flow channel in order to remove all air
8. Allow rig to warm up until the average temperature of any one thermocouple is changing less than 0.5 degrees per hour
9. Adjust throttling valve to achieve desired test flow rate
10. Unplug pump
11. Stop data acquisition software
12. Set bath temperature to 3 °C above desired average capture temperature

B.4 – Capture Test

1. When bath reaches temperature set point, plug in pump and immediately turn on data acquisition program
2. Allow test to run until all PCM thermocouples are 1.2 °C above the melt temperature (43.5 °C for lauric acid)
3. Turn off data acquisition software and restart
4. Set bath temperature to 5 °C above desired initial temperature for recovery test

B.5 – Stabilization

1. Allow rig to stabilize until the average temperature of any one thermocouple is changing less than 0.5 degrees per hour
2. Adjust throttling valve to achieve desired test flow rate
3. Unplug pump
4. Stop data acquisition software
5. Set bath temperature to 2 °C above desired average capture temperature

B.5 – Recovery Test

1. When bath reaches temperature set point, plug in pump and immediately turn on data acquisition software
2. Allow test to run until all PCM thermocouples are 1.2 °C below the melt temperature (43.5 °C for lauric acid)

3. Turn off data acquisition software, pump, water bath, data acquisition module and computer

APPENDIX C – CALIBRATION AND ERROR ANALYSIS

C.1 – Material Property Data

Melt temperature, freezing temperature, densities, conductivities, heat capacity and latent heat of fusion of materials can vary dependent on the grade of material used. Since literature values of these properties are used in the model, the range of potential literature values for stearic acid has been studied and is listed in table C.1. Based on these ranges, the potential error in material properties has been estimated.

Table C.1: Melt temperature variation for different grades of stearic acid.

Property	Unit	Min.	Ref.	Max.	Ref.
Melting Temperature	[°C]	53	(Hummel Croton, 2009)	72	(Sigma Aldrich, 2009)
Freezing Temperature	[°C]	53	(Hummel Croton, 2009)	72	(Sigma Aldrich, 2009)
Latent Heat of Fusion	[J/kg]	155	(Kenisarin et al., 2007)	208.6	(Sari, 2006)
Thermal Conductivity	[W/mK]	0.172	(Zalba et al., 2003)	0.30	(Karaipekli et al., 2007)
Heat Capacity	[J/kgK]	2.38	(Kenisarin et al., 2007)	2.83	(Kenisarin et al., 2007)
Density	[kg/m ³]	848	(Zalba et al., 2003)	965	(Zalba et al., 2003)

C.2 – Scale (PCM Mass Measurement)

The Starfrit 93033 scale was used to determine the PCM mass by weighing the liquid PCM container before and after pouring the lauric acid into the test apparatus. The

accuracy of the scale is quoted in the product literature as $\pm 1.0\text{g}$ (Starfrit, 2009). This was verified using a set of calibrated masses and found to be true. In addition to the 1.0 g error in the scale, some additional sources of error in the total melted amount of phase change material exist. A small amount of spillage can occur during filling, causing approximately 25 g of additional error. This was determined by allowing the excess material to solidify on the apparatus and then chipping it off and weighing it with an additional factor of 1.25 added for losses during this process. The mass of phase change material present in the test apparatus can therefore vary by $\pm 26\text{g}$ or $\pm 2\%$.

C.3 – PCM Thermocouples

Thermocouple error calculations are found in section 3.8. The calibration coefficients for the PCM thermocouples are found in table C.2.

Table C.2: Flow meter calibration data.

Thermocouple	Slope (m)	Offset (b)
1	0.992549	0.353149
2	0.992494	0.396861
3	0.992308	0.431849
4	0.992591	0.443336
5	0.992758	0.461873
6	0.992755	0.469857
7	0.992590	0.499508
8	0.992163	0.530811
9	0.992334	0.537212
10	0.992346	0.476022
11	0.992319	0.579934
12	0.992119	0.612231
13	0.992088	0.627743
14	0.992236	0.622614
15	0.991665	0.603178
16	0.992081	0.554465

C.4 – Flow Meter

Calibration of the flow meter was accomplished by hooking the instrument up to the data acquisition system as it is in testing. Hoses were attached to the meter with the inlet routed to a supply water faucet with a shut-off valve and the outlet routed to a beaker. The tare weight of the beaker was recorded at the start of each test. The faucet was adjusted to achieve several different flow rates with the shut-off valve opened at time zero. The water was allowed to run for either one or two minutes, depending on the flow rate and then the shut-off valve was closed. The beaker was then weighed to determine the total mass accumulated during the test period. This was compared to the time-average flow reading from the data acquisition system. The results can be seen in table C.3. Comparing these results gives a linear calibration equation with slope of 1.0408 and offset of 0.0372. Error for the flow meter readings is calculated in section 3.8.

Table C.3: Flow meter calibration data.

Time Period [s]	Mass [kg]	Average Flow from Mass [L/min]	Flow Reading [L/min]
120	418	0.209	0.1662
120	747	0.373	0.3252
60	455	0.454	0.3938
60	591	0.590	0.5268
60	734	0.733	0.6677
60	830	0.828	0.7635
61	911	0.909	0.8398
60	945	0.943	0.8755
60	607	0.606	0.5370
60	444	0.443	0.3856
60	276	0.275	0.2339
120	364	0.182	0.1448

C.5 – Heat Loss to Surroundings

At the end of the first melting test the apparatus was allowed to cool naturally to determine the heat loss to the surroundings. The average heat flux per unit area through the aluminum plate for 27 to 31 °C of temperature loss can be seen in figure C.5.1. The heat transfer through the aluminum plate reversed below this temperature difference due to heat loss back through the stagnant flow channel. Since the flow temperature is controlled in the experiments, it will be assumed that the heat loss is negligible below 27 °C of temperature difference from the average cell temperature to the ambient. The heat loss for the adjusted value is therefore calculated using the polynomial fit shown in figure C.5.1 for temperature differences above 27 °C and set to zero for differences below this.

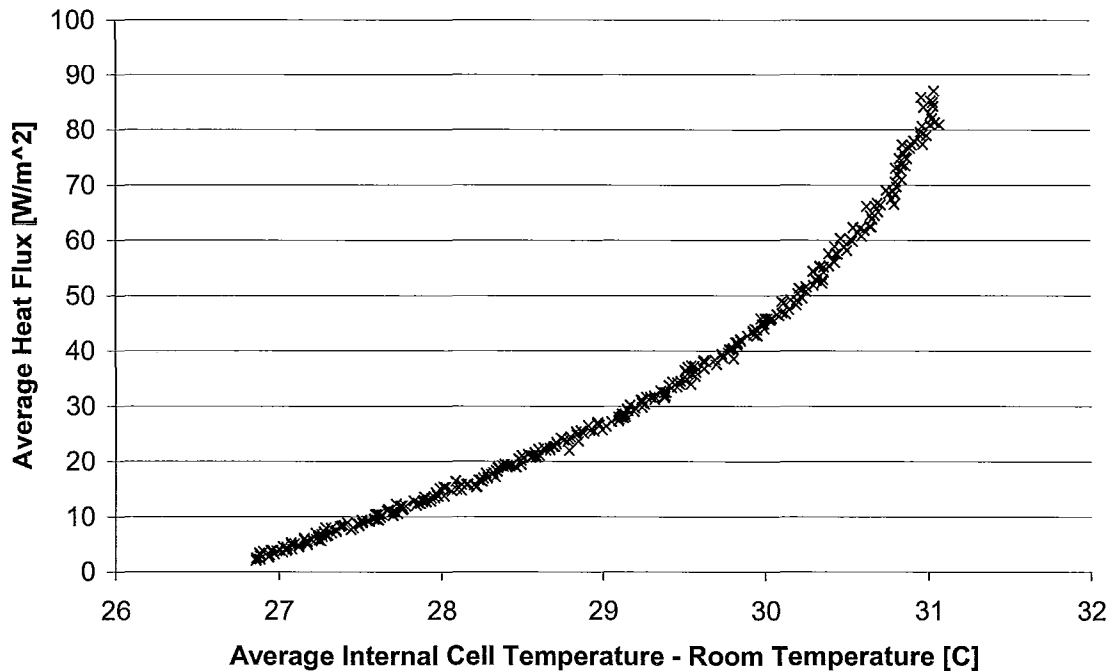


Figure C.1: Heat loss to surroundings under natural convection.

C.6 – Heat Flux Sensors

Calibration of the heat flux sensors was not performed. This was due to the large error involved in calculating the enthalpy change of the capture or recovery fluid due to the cumulative temperature and flow rate error. The temperature measurement in the fluid was even larger than the calculated values for the phase change material temperature measurement due to the temperature gradient within the flow. The position of the thermocouple junction within the flow was unknown and not easily adjusted. The temperature error for the bulk flow would therefore be larger than the 1 °C temperature difference in the flow towards the end of the melt time. This, in addition to the +/-12% error in the flow rate and losses to the surroundings makes calibrating the heat flux

sensors against the flow enthalpy change unfeasible. Since the heat flux sensor readings were not used in further calculations and accurate values of losses through the insulation are not known, error estimates for the heat flux sensors were not used.

C.7 – Flow Temperature

Because the heat transfer to the cell using the flow temperature difference is not being used as a meaningful comparison for the model, the error in the capture/recovery fluid temperature only causes a difference in the model input versus the test data.

APPENDIX D – CFD MODEL SET-UPS

D.1 – Two Dimensional Base Case

Table D.1: Fluent input parameters for the CFD model base case.

Category	Name	Parameter	Units	Value	
Materials	lauric_acid	Density	kg/m ³	869	
		Heat Capacity	J/kgK	2150	
		Thermal Conductivity	W/mK	0.17	
		Viscosity	kg/ms	0.0073 (N/A)	
		Melting Heat	J/kgK	182800	
		Solidus Temperature	K	316.15	
		Liquidus Temperature	K	317.15	
		air	Density	kg/m ³	1.225
			Heat Capacity	J/kgK	1006.43
	Thermal Conductivity		W/mK	0.0242	
	Viscosity		kg/ms	1.7894e-05	
	Melting Heat		J/kgK	0	
	Solidus Temperature		K	0	
	aluminum	Density	kg/m ³	2719	
		Heat Capacity	J/kgK	871	
Thermal Conductivity		W/mK	202.4		
stainless steel		Density	kg/m ³	8000	
		Heat Capacity	J/kgK	500	
		Thermal Conductivity	W/mK	16.4	
Boundary Conditions	al_1	Type		Wall	
		Material Name		aluminum	
		Thermal		Coupled	
	al_1-shadow	Type		Wall	
		Material Name		aluminum	
		Thermal		Coupled	
	al_2	Type		Wall	
		Material Name		aluminum	
		Thermal		Coupled	
	al_2-shadow	Type		Wall	
		Material Name		aluminum	
		Thermal		Coupled	
	al tube	Type		Solid	
		Material Name		aluminum	
		pcm	Type		Fluid
Material Name			lauric acid		
recovery	Type			Fluid	
	Material Name		Air		

Table D.1 continued: Fluent input parameters for the CFD model base case.

	recovery_cl	Type		Wall
		Material Name		Aluminum (N/A)
		Thermal		Heat Flux
		Heat Flux	W/m^2	0
	ss_1	Type		Wall
		Material Name		stainless_steel
		Thermal		Convection
		Heat Transfer Coefficient	W/m^2K	100
		Free Stream Temperature	K	338.15
	ss_2	Type		Wall
		Material Name		stainless_steel
		Thermal		Coupled
	ss_2-shadow	Type		Wall
		Material Name		stainless_steel
		Thermal		Coupled
	ss_tube	Type		Solid
		Material Name		stainless_steel
	walls	Type		Wall
		Material Name		Aluminum (N/A)
		Thermal		Heat Flux
		Heat Flux	W/m^2	0

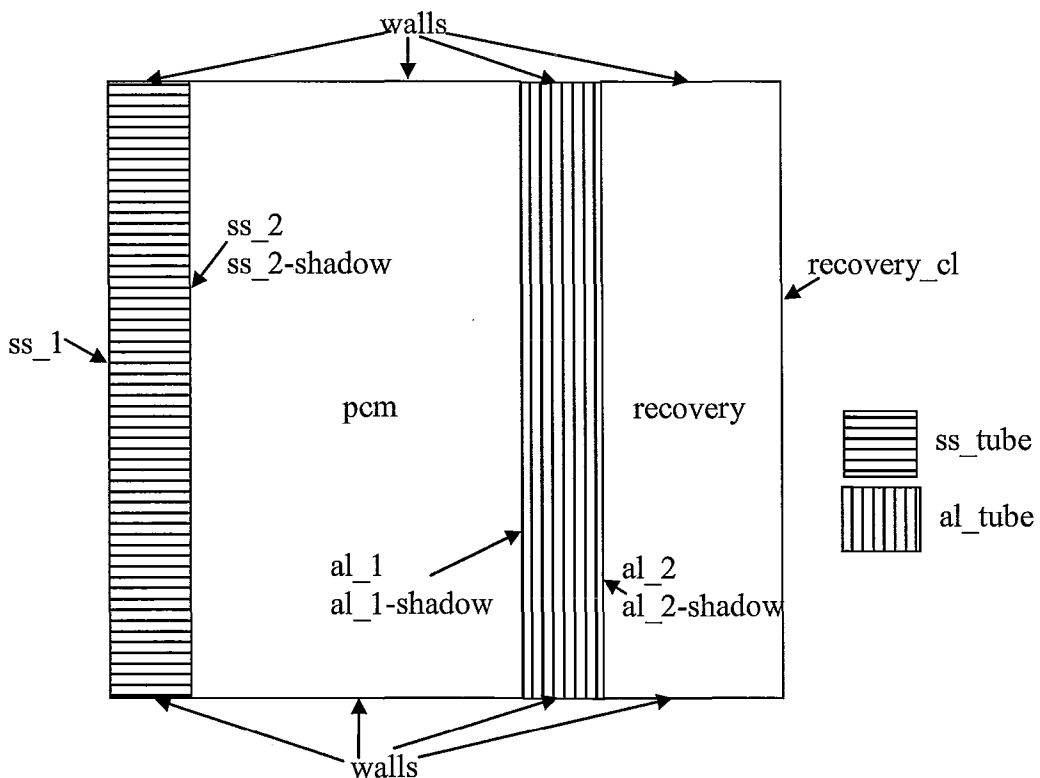


Figure D.1: Model boundaries for the two-dimensional CFD cases.

Table D.2: ANSYS-Fluent 6.3.26 set up parameters for 2D flow solution.

Menu	Category	Parameter	Value	
File	Read	Case	Base_Case.msh	
Define	Models-Solver	Solver	Pressure Based	
		Space	2D	
		Velocity Formulation	Absolute	
		Gradient Option	Green-Gauss Cell Based	
		Porous Formulation	Superficial Velocity	
		Models-Energy	Energy Equation	On
		Models-Viscous	Model	k-epsilon
			k-epsilon Model	Realizable
			Near-Wall Treatment	Enhanced Wall Treatment
			Enhanced Wall Treatment Options	None
	Viscous Heating		Off	
	C2-Epsilon		1.9	
	TKE Prandtl Number		1	
	TDR Prandtl Number		1.2	
	Energy Prandtl Number		0.85	
	Wall Prandtl Number		0.85	
		User Defined Functions	None	
	Models-S/M	Solidification/Melting	On	
		Mushy Zone Constant	100,000	
		Include Pull Velocities	No	
Materials	All	Table 4.9		
Boundary Conditions	All	Table 4.9		
Solve	Controls-Solutions	Equations	Flow & Turbulence	
		Pressure-Velocity Coupling	SIMPLE	
		Under-Relaxation Factors	Pressure – 0.3 Density – 1 Body Forces – 1 Momentum – 0.7 TKE – 0.8 TDR – 0.8 Turbulent Viscosity – 1 Liquid Fraction Update – 0.9 Energy – 1	
		Discretization	Pressure – Standard Momentum – 2 nd Order TKE – 2 nd Order TDR – 2 nd Order Energy – 2 nd Order	

Table D.2 continued: ANSYS-Fluent 6.3.26 set up parameters for 2D flow solution.

	Initialize	Reference Frame	Relative to Cell Zone
		Gauge Pressure	100 Pa
		X Velocity	0 m/s
		Y Velocity	0 m/s
		Z Velocity	0 m/s
		TKE	0.01 m ² /s ²
		TDR	1 m ² /s ³
		Temperature	313.15 K
	Monitors-Residual	Check Convergence	All Off
	Monitors-Surface	Report	Static Pressure
		Surfaces	Inlet
		Report Type	Area-Weighted Average
		X Axis	Iteration
	Monitors-Volume	Field Variable	Velocity Magnitude
		Cell Zones	Water
		Report Type	Max
		X Axis	Iteration

Table D.3: ANSYS-Fluent 6.3.26 set up parameter changes for 2D energy solution.

Menu	Category	Parameter	Value
	Boundary Conditions	inlet-Temperature	
		outlet-Temperature	
Solve	Controls-Solutions	Equations	Energy
	Monitors-Residual	Check Convergence	On
		Energy Residual	1e-08
	Monitors-Surface	1 – When	Time Step
		1 – Report	Total Surface Heat Flux
		1 – Surfaces	al_plate2:005, gaskets:002, pcm_chamber
		1 - Report Type	Area-Weighted Average
		1 - X Axis	Flow Time
		2 – When	Time Step
		2 – Report	Total Temperature
		2 – Surfaces	al_plate2:005
		2 - Report Type	Area-Weighted Average
		2 - X Axis	Flow Time
	Monitors-Volume	When	Time Step
		Field Variable	Liquid Fraction
		Cell Zones	Water
		Report Type	Volume-Average
		X Axis	Flow Time
	Iterate	Time Step Size	10 s
		Time Stepping Method	Fixed
		Max Iterations per Time Step	100
		Reporting Interval	1
		UDF Profile Update Interval	1

D.2 – Two Dimensional Parametric Cases

Table D.4: ANSYS-Fluent 6.3.26 set up changes for the 2D parametric energy solutions.

Zone	Property	Units	Alternate Values
PCM	Heat Capacity	J/kgK	1075
			1720
			2580
	Latent Heat of Fusion	J/kg	91400
			146240
			219360
	Thermal Conductivity	W/mK	0.1
			1
			10
			100
Capture Channel	Heat Capacity	J/kgK	100
			1000
			5000
	Thermal Conductivity	W/mK	1
			10
			100
			1000
Recovery Channel	Heat Capacity	J/kgK	100
			500
			5000
	Thermal Conductivity	W/mK	1
			10
			100
			1000
Capture Fluid	Convective Coefficient	W/m ² K	10
			100
			1000
			10000
	dT Capture – T melt	°C	1
			100
			1000
Recovery Fluid	Heat Capacity	J/kgK	100
			500
			5000
	Thermal Conductivity	W/mK	0.01
			0.1
			1
			10

D.3 – Three Dimensional Lauric Acid Cell

Table D.5: Lauric Acid CFD model boundary conditions and material properties.

Category	Name	Parameter	Units	Value	
Materials	lauric acid	Density	kg/m ³	869	
		Heat Capacity	J/kgK	2150	
		Thermal Conductivity	W/mK	0.17	
		Viscosity	kg/ms	0.0073	
		Melting Heat	J/kgK	182800	
		Solidus Temperature	K	316.15	
			Liquidus Temperature	K	317.15
	water	Density	kg/m ³	998.2	
		Heat Capacity	J/kgK	4182	
		Thermal Conductivity	W/mK	0.6	
		Viscosity	kg/ms	0.000453	
		Melting Heat	J/kgK	0	
		Solidus Temperature	K	0	
			Liquidus Temperature	K	0
		aluminum	Density	kg/m ³	2719
Category	Name	Parameter	Units	Value	
		Heat Capacity	J/kgK	871	
		Thermal Conductivity	W/mK	202.4	
	polycarbonate	Density	kg/m ³	1200	
		Heat Capacity	J/kgK	1500	
		Thermal Conductivity	W/mK	0.195	
	nitrile	Density	kg/m ³	1100	
		Heat Capacity	J/kgK	2010	
		Thermal Conductivity	W/mK	0.13	
	Boundary Conditions	external	Type		Wall
			Thermal		Heat Flux
			Heat Flux	W/m ²	0
		inlet	Type		Mass Flow Inlet
			Mass Flow Rate	kg/s	0.00435
			Supersonic Pressure	Pa	0
Direction Specification				Normal to Boundary	
Reference Frame				Absolute	
Turbulence Specification Method				Intensity and Hydraulic Diameter	
Turbulent Intensity			%	1	
Hydraulic Diameter			m	0.0127	
Total Temperature			K	335.85	
int *		Type		Interior	
nitrile		Type		solid	
		Material		nitrile	
outlet	Type		Pressure Outlet		
	Supersonic Initial Gauge Pressure	Pa	0		
	Backflow Direction		Normal to Boundary		

Table D.5 continued: Lauric Acid CFD model boundary conditions and material properties.

		Backflow Turbulent Intensity	%	1
		Backflow Hydraulic Diameter	m	0.0127
		Backflow Total Temperature	K	335.85
	pc	Type		Solid
		Material		Polycarbonate
	pcm	Type		Fluid
		Material		lauric acid
	water	Type		Fluid
		Material		Water
	All Remaining	Type		Wall
		Thermal		Coupled

Table D.6: ANSYS-Fluent 6.3.26 set up parameters for 3D flow solution.

Menu	Category	Parameter	Value
File	Read	Case	LA_Cell.msh
Define	Models-Solver	Solver	Pressure Based
		Space	3D
		Velocity Formulation	Absolute
		Gradient Option	Green-Gauss Cell Based
		Porous Formulation	Superficial Velocity
	Models-Energy	Energy Equation	On
	Models-Viscous	Model	k-epsilon
		k-epsilon Model	Realizable
		Near-Wall Treatment	Enhanced Wall Treatment
		Enhanced Wall Treatment Options	None
		Viscous Heating	Off
		C2-Epsilon	1.9
		TKE Prandtl Number	1
		TDR Prandtl Number	1.2
		Energy Prandtl Number	0.85
		Wall Prandtl Number	0.85
		User Defined Functions	None
	Models-Solidification and Melting	Solidification/Melting	On
		Mushy Zone Constant	100,000
		Include Pull Velocities	No
	Materials	All	Table 4.9
	Boundary Conditions	All	Table 4.9
Solve	Controls-Solutions	Equations	Flow & Turbulence
		Pressure-Velocity Coupling	SIMPLE

Table D.6 continued: ANSYS-Fluent 6.3.26 set up parameters for 3D flow solution.

		Under-Relaxation Factors	Pressure – 0.3 Density – 1 Body Forces – 1 Momentum – 0.7 TKE – 0.8 TDR – 0.8 Turbulent Viscosity – 1 Liquid Fraction Update – 0.9 Energy - 1
		Discretization	Pressure – Standard Momentum – 2 nd Order TKE – 2 nd Order TDR – 2 nd Order Energy – 2 nd Order
	Initialize	Reference Frame	Relative to Cell Zone
		Gauge Pressure	100 Pa
		X Velocity	0 m/s
		Y Velocity	0 m/s
		Z Velocity	0 m/s
		TKE	0.01 m ² /s ²
		TDR	1 m ² /s ³
		Temperature	313.15 K
	Monitors-Residual	Check Convergence	All Off
	Monitors-Surface	Report	Static Pressure
		Surfaces	inlet
		Report Type	Area-Weighted Average
		X Axis	Iteration
	Monitors-Volume	Field Variable	Velocity Magnitude
		Cell Zones	water
		Report Type	Max
		X Axis	Iteration

Table D.7: ANSYS-Fluent 6.3.26 set up parameter changes for 3D energy solution.

Menu	Category	Parameter	Value
	Boundary Conditions	inlet-Temperature	
		outlet-Temperature	
Solve	Controls-Solutions	Equations	Energy
	Monitors-Residual	Check Convergence	On
		Energy Residual	1e-08
	Monitors-Surface	1 – When	Time Step
		1 – Report	Total Surface Heat Flux
		1 - Surfaces	al_plate2:005, gaskets:002, pcm_chamber
		1 - Report Type	Area-Weighted Average
		1 - X Axis	Flow Time
		2 – When	Time Step
		2 – Report	Total Temperature
		2 - Surfaces	al_plate2:005
		2 - Report Type	Area-Weighted Average
		2 - X Axis	Flow Time
	Monitors-Volume	When	Time Step
		Field Variable	Liquid Fraction
		Cell Zones	Water
		Report Type	Volume-Average
	Iterate	X Axis	Flow Time
		Time Step Size	10 s
		Time Stepping Method	Fixed
		Max Iterations per Time Step	100
		Reporting Interval	1
		UDF Profile Update Interval	1